Development and Validation of Models for Prediction and Control of Machining Distortion in Aluminum Samples

By

JULIANNE EMILY JONSSON
THESIS

Submitted in partial satisfaction of the requirements for the degree of

MASTER OF SCIENCE

in

Mechanical and Aerospace Engineering

in the

OFFICE OF GRADUATE STUDIES

of the

UNIVERSITY OF CALIFORNIA

DAVIS

Approved:

Barbara S. Linke, Co-Chair

Michael R. Hill, Co-Chair

Bahram Ravani

Committee in Charge

2021

Abstract

Residual stresses induced from manufacturing processes produce distortion in aluminum workpieces. It is desirable to control distortion from manufacturing process to prevent part rejection or rework. Both the near surface residual stress from milling processes and the bulk residual stress from manufacturing processes contribute to the distortion. Predicting the distortions using finite element models can help improve the quality of manufactured components and reduce non-conformity costs. The finite element model uses elastic stress analysis which is a mechanics boundary value problem to form the basis of the prediction. The machining is included by introducing an initial stress state near the machined surface. The distortion model is created based off predetermined workpiece geometry, known as the "feature sample", and uses residual stress measurements on a line milled stress relieved plate AA7050 T7451 as the input to the finite element model. The near surface residual stress measurements are completed using hole-drilling, and the bulk residual stress measurements are completed using slitting. To increase complexity, a model with a spiral path milling pattern and a model with high bulk residual stress from quenched material are created. Models are validated using three methods, by comparing the bottom face of the observed and predicted samples, by comparing the residual stress profiles that are used as inputs to the model to measured residual stress profiles taken in areas of aggressive machining on the sample, and by comparing the bottom surface form of a removed and isolated section of the workpiece.

The validation experiments for the stress relieved and line milled samples show agreement between predicted and observed results. For the bottom face comparison, both the surface form and line plots taken along the bottom face are compared. The observed surface forms and the line plots agree with the shape of the predicted surface forms and line plots. The 3 mm low stress sample has better agreement within the uncertainty for the line plots than the 7 mm sample. The residual stress measurements that were taken on the sample are nearly identical with the grand average stress profiles applied to the model. The isolated pocket floors also agree well between the predicted and observed data, with line plots showing good agreement in both the 3 mm and 7 mm samples. Assuming that there is negligible near surface stress in the remaining surfaces of the sample is supported by measurements taken along the walls and bottom of the sample, which demonstrate near zero stress.

The validation experiments for the spiral milled and high bulk stress samples add complexity to the distortion prediction method. The spiral milled observed and predicted bottom face line plots and surface form agree, with better agreement in the 3 mm sample than the 7 mm sample. The residual stress measurements completed in the pocket of the spiral stress feature sample have slightly more compressive stress along σ_{xx} and σ_{yy}, but the profiles do agree with the shape and magnitude of the grand average stress profiles. The isolated pocket floor surface form and line plots for the spiral sample also agree, with better agreement for the 3 mm pocket floor. The high bulk residual stress observed and predicted surface form and line plots agree, with better agreement in the 7 mm sample than the 3 mm sample. Residual stress measurements taken in the 7 mm sample agree with data taken from representative material. Residual stress measurements taken in the 3 mm sample shallower near surface data than the 7 mm measurements. Finite element models still provide a reasonable estimate of distortion in these samples for different milling and material conditions.

Future work could analyze other types of machining and other geometries. It might also be useful to create a 3-dimensional model of the distortion for comparison to the observed results. This 3-dimensional model is out of scope for this work but could be useful in other studies. The interaction between the bulk residual stress and machining induced residual stress in samples with thin walls should also be explored. Additional refinement to this method in future work could help improve the method for application to industry.

Acknowledgements

Thank you to Barbara S. Linke, Michael R. Hill, and Bahram Ravani for their roles and advice in being committee members and professors. I enjoyed taking classes with all 3 of my committee members and I appreciated their continued support throughout my graduate program. Thank you to Barbara S. Linke and Michael R. Hill for their mentorship and guidance while I completed research for this thesis. Additionally, thank you to Christopher R. Chighizola, Christopher R. D'Elia, and Nicholas A. Bachus, who were my laboratory partners and who aided my progress throughout the graduate program. Thank you to Hill Engineering, LLC for the loan, and frequent advice given on their residual stress measurement machine.

This research was funded by the National Science Foundation (NSF) under the Award No. 1663341 (Division of Civil, Mechanical and Manufacturing Innovation (CMMI)). This research was also a collaboration between the University of California Davis and the Technische Universität Kaiserslautern (TUK). The UC Davis team included Barbara S. Linke, Michael R. Hill, Christopher R. D'Elia, and Christopher R. Chighizola. The TUK team included Jan Aurich, Benjamin Kirsch, and Daniel Weber, and was funded by the Deutsche Forschungsgemeinschaft (DFG) within project AU 185/64 1. Any opinions, findings, and conclusions or recommendations expressed in this material are those of the authors and do not necessarily reflect the views of the NSF or DFG.

Table of Contents

List of Figures

List of Tables

Chapter 1 – Introduction

Thin-walled aluminum components are often used in aircraft because of their high strength to weight ratio. Due to thin sections, complex geometries and high tolerances, aircraft component production can have challenges due to residual stresses [1]. Residual stresses in aluminum arise from the manufacturing processes, particularly the heat treatment and milling which introduce bulk and near surface residual stress that drive geometric distortion [2][3]. The geometric distortion can cause part rejection or rework, resulting in economic losses [1]. In order to minimize these economic losses, distortion should be modeled and predicted.

Residual stress is an internal stress that is introduced during manufacturing processes and can only be measured post-process using destructive experimental techniques. Typically, the residual stress is estimated from measurements of strain in the material, where a destructive process releases the strain and plastic deformation. The residual stress can then be used in models to determine the influence residual stress has on distortion in that material. Comparisons between model and observed results can determine the usefulness of these models. The following chapters will analyze the usefulness of models based off residual stress measurements in representative material for prediction and control of workpieces with complex geometries. The model will explore workpieces with different thicknesses, different material conditions, and different machining patterns.

Chapter 2 will develop the distortion prediction finite element model which is the basis for the finite element model analysis. Residual stress measurements are completed using two different methods, with fine increment hole-drilling to assess the near surface residual stress, and with slitting to assess the bulk residual stress in the material. A finite element model is developed to predict distortion in a predetermined workpiece geometry. The workpiece was designed to

simulate a thin-walled, lightweight aerospace component and will be referred to as the feature sample. The workpiece is then machined, and validation experiments are performed on the machined sample to determine the usefulness of the prediction. Three distinct validation experiments are developed to compare the observed and predicted results. Two of the validation experiments compare observed and predicted distortion measured using a TalyScan 250 laser scanning profilometer. The first comparison scans one surface of the feature sample for comparison to the finite element model. The other comparison removes a section of the bottom plate on the feature sample where aggressive machining occurs and compares the isolated surface to a finite element model with the same geometry. The third validation experiment measures the residual stress in the feature sample and compares the measured residual stress with the applied residual stress.

An expansion on the distortion prediction method is explored in Chapter 3. Complexity is added by analyzing different machining tool paths and by changing the underlying bulk residual stress in the material. The previous model focused on simple machining paths and low bulk residual stress. To achieve this, a straight-line path was machined in certain locations on the sample, and the material was from a material condition known to have low levels of bulk residual stress [4]. The more complex model will analyze a spiral path machined sample. An additional model will analyze samples with high bulk residual stress. The spiral path machining was introduced as a method to reduce the distortion in the workpieces [5]. The high bulk residual stress model will analyze the interaction of bulk residual stress and near surface milling induced residual stress and how that effects the distortion prediction method. Validation experiments that were introduced in Chapter 2 will be utilized in Chapter 3 to determine the usefulness of the model compared to the observed results. The observed distortion along the bottom face of the

feature samples will be compared to the predicted distortion as well as the distortion of the removed section where removing the sections led to isolating the influence of the aggressive machining. In addition to the distortion comparisons, residual stress measurements were completed in the feature sample and compared to the applied residual stress profiles. The discussion on the validation experiments analyzes the usefulness of this method and determines the outlook for future work.

Chapter 2 – Description and Development of Feature Sample Model to Predict Distortion in Stress Relieved and Milled AA7050

2.1 Introduction

The distortion from residual stresses can be modeled using different methods. Some methods use modeling of the machining to determine the residual stresses in the parts. One method by Schindler et al. [6] was able to model deformations using finite element (FE) simulations based on temperature distributions, cutting conditions, and the location of the cutting tool relative to the workpiece. Schindler et al. found that the method allowed calculation of the distortion of the workpiece, but additional work of including the thermal expansion and deflection of the tool and tool holder was needed to enhance the prediction. Another method of modeling the machining distortion was developed by Ma et al. [7]. They found that the material removal and the loads induced from cutting must be properly accounted for in the FE model to accurately predict distortion. In addition to machining modeling, another method by Aurrekoetxea et al. [8] used equivalent bending stiffness calculations for ribbed components. They found that the equivalent bending stiffness presented a good approximation of the bulk residual stress, but the distortion prediction needed additional inputs for greater accuracy, such as measured residual stress profiles.

Other methods use residual stress fields established from measurements as input to FE models to predict distortion. One example of this method by Huang et al. [9] used measured residual stresses from crack-compliance as an input to a FE model to model the deformation of a monolithic beam. The authors found that there was good prediction accuracy of the FE model when compared to the observed results of two same machined monolithic components when

using this method of distortion prediction. For these authors, the geometry in the FE model is reflected by a set of elements that comprise the geometry of the physical workpiece, which results in the prediction of the distortion. Another method specifically isolated the milling induced residual stresses (MIRS) as inputs to the FE model. This method was investigated by Madariaga et al. [5] and Zhang et al. [10], where both models were able to accurately predict distortion in experimental samples. However, these studies focused on relatively simple geometries.

This study will focus on distortion prediction in relatively complex parts since previous research has focused on distortion prediction on parts with relatively simple geometries. This study uses measured residual stresses to predict distortion by applying these stresses to a FE model, whose geometry is representative of complex workpieces. The FE model which uses measured residual stress data will predict distortion in a complex geometry workpiece. The predicted distortion will then be validated by performing three types of validation experiments.

2.2 Methods

A linearly elastic finite element (FE) model is developed to predict distortion in a workpiece due to machining induced residual stress, where elastic stress analysis forms the basis of the prediction. The stress analysis is a mechanics boundary value problem, where the domain is the geometry of the workpiece. The material behavior is assumed to be elastic with properties reflecting those of the workpiece. The boundary conditions are traction free surfaces and minimal displacement conditions that eliminate rigid body motion. The effect of machining is included by introducing an initial stress state near the machined surfaces representative of the effect of the machining operation. The effect of the material preparation is included by

introducing an initial bulk residual stress state in the material. A solution for equilibrium given those initial stresses produces an output displacement, which comprises the distortion prediction.

First, a plate sample of representative material will be machined with the same machining conditions and material properties as the workpiece. Residual stress measurements will be completed on this sample to determine the initial stresses. The initial stresses will then be applied to an FE model that has been developed of the workpiece geometry. The workpiece geometry will be somewhat complex, with thin walls, curves, and straight edges. A physically machined workpiece of the complex geometry will be used as a basis for the validation of the distortion prediction method.

2.2.1 Initial stress state

The initial stress state at and adjacent to the machined surface is the key input to the FE distortion model. The initial stress state could be determined by nonlinear process modeling that simulates the thermo-elasto-plastic deformation due to milling (e.g., the work in [6][11]). The present work develops the initial stress state experimentally from measurements of near surface residual stress in milled plates, where the plates are of representative material and milled with the same cutting parameters as used to fabricate the workpiece. The work also uses previous research to develop the values of bulk residual stress in the material [12]. Here, the plates are large enough to perform measurements in steady state milling and thick enough that the near surface residual stress is not lost to distortion when the part is unclamped and tries to obtain equilibrium.

2.2.2 Feature sample

To validate the distortion model, we designed a workpiece with some geometric complexity. This workpiece will be called the “feature sample”. The feature sample was designed to simulate a thin-walled, lightweight aerospace component, an example of the sample is shown in Figure 1. The sample has either 3 mm or 7 mm thick walls, and is made from AA 7050-T7451, a typical aircraft alloy. The specific dimensions for the feature sample are shown in Figure 2. The feature sample includes five bolt holes that are used to clamp the sample during milling. Labels are to describe different areas of the feature sample (Figure 1). The bottom face is the xy-plane where z = 20 mm. The side opposite the bottom face is the top, which is at z = 0. The location of the pocket floors, bolt holes, sidewalls, endwalls, top face, and bottom face of the feature sample is shown in Figure 1.

The feature samples were milled from a supply of consistently prepared plate samples that had been cut from a single 7050-T7451 plate, originally 1250 mm by 1250 mm by 102 mm. The 51 suffix reflects stress relieved rolled plate with plastic stretch stress relief, a material condition known to have low levels of bulk residual stress [4]. The plate samples were removed using a saw, each plate 206 mm long (along LT (length transverse)) by 102 mm wide (along ST (straight transverse)) by 28 mm thick (along L (length)). A coordinate system was established for the plates so that the x-direction is along the 206 mm length, the y-direction is along the 102 mm width, and the z-direction is along the 28 mm thickness (as shown in Figure 1).

The manufacturing of the feature sample was accomplished in 5 steps. The first step involved side milling the outer sidewalls of the sample using a 12 mm diameter Kennametal F3AA1200AWL endmill with 3 flutes. The cutting speed was 450 m/min and the feed per tooth was 0.055 mm. This step had a relatively low width of cut (2.5 mm), which indicated it would

produce shallow MIRS in the outside sidewalls [13]. The second and third step involve milling the bottom and top faces of the feature sample using a 50 mm diameter Sandvik R590-050HA6-11M indexable tool with 2 inserts. A relatively low cutting depth was chosen (1.5 mm) to induce low MIRS [13]. The fourth step involved drilling the 5 bolt holes into the sample. The fifth and final step was the milling of the pockets of the feature sample using the 12 mm diameter Kennametal F3AA1200AWL endmill with 3 flutes. All the steps are performed without cutting fluids. The pockets are milled with line milling into what will be designated as the face of the sample. This milling was chosen to have comparatively aggressive machining conditions, (with a cutting speed of 200 m/s, a feed per tooth of 0.2 mm, an axial engagement of 3 mm and a radial engagement of 4 mm). The milling of inner sidewalls was then accomplished to remove stepover features from the milling of the pocket, with a width of cut of 0.2 mm. More detail about the manufacturing process is discussed by Weber et al. [14]. An example of a machined sample is shown in Figure 3. The pocket floor has considerable texture from the aggressive milling, as noted in our earlier work [15].

The feature sample model addresses the pocket floor residual stresses and the bulk residual stresses. The model will apply near surface residual stress profiles that are representative of the aggressive milling to the pockets of the sample. The pockets of the floor are assumed to be milled with line milling, where line milling refers to steady state milling along the x-axis, without any changes in milling direction. Surfaces were purposefully machined to only have stresses significant on one surface to determine the influence that surface had on the overall distortion of the workpiece. The bottom, inside and outside sidewalls and endwalls, and the face of the sample are considered to have negligible near surface residual stresses because they were machined with finishing milling parameters.

2.2.3 Residual stress measurements

This study uses hole-drilling measurements as the method to quantify near surface residual stress due to milling. The residual stresses from milling can be measured using a range of techniques, as shown in our earlier work [15], with hole-drilling providing consistent and useful results. Other work [16] applied hole-drilling to a wide range of milled plates and found good repeatability of MIRS data measurements when there was stable machining. The near surface residual stress measurement depth schedule from this work is shown in Table 1. These earlier results were the basis for using hole-drilling in this study. Figure 4 shows the hole-drilling experimental set-up. This study also uses slitting as the method to quantify bulk residual stress in an unmachined stress relieved rolled plate with plastic stretch stress relief (T7451). The bulk residual stress that is applied to the model is taken from previous work [12]. The near surface residual stress and the bulk residual stress is added to comprise the initial stress state.

The hole-drilling measurements followed ASTM E837 [17] but were modified to use fine cut depth increments to improve near surface resolution [18]. This modification has been shown in prior work with the same material to be very repeatable [15]. Hole-drilling provides depth profiles for the three in-plane components of stress (σ_{xx}, σ_{yy}, and σ_{xy}). A measurement comprises bonding a three-element strain gage rosette on the surface and milling a 2 mm diameter hole into the surface of the part in small increments of depth. Stress versus depth is then computed from measured strain versus depth data [17]. For consistent results, depth correction is utilized so the measured final depth of the hole is consistent with the final intended hole depth, which improves measurement accuracy (see [15]).

The initial stress input for the distortion model is found by measuring residual stress at the surface of multiple thick plate samples milled on one 206 x 102 mm surface. The other

surfaces of the plate remain unmachined. Multiple measurements across multiple samples were used to develop a representative machining induced residual stress field that accounts for variations from the stock material, the milling process, and the stress measurements. Measurements were completed on 4 plate samples. Three of the plate samples had 3 hole-drilling measurements, and one sample had 6 hole-drilling measurements. A summary of the plate sample ID and the number of hole drilling measurements completed on each surface is shown in Table 2. The average of the stress profiles on each sample was computed, and a grand average across all samples was computed along with the standard deviation among the four sample averages. The grand average is used as the initial stress input for the distortion prediction model.

2.2.4 Feature sample model specifics

To create a finite element model with robust distortion prediction, certain modeling parameters were chosen. The model material has a Young's Modulus of 72000 MPa and Poisson's ratio of 0.33. An in-plane mesh of 2 mm is used in the sample, with a 0.01 mm to 1 mm bias mesh being applied in starting at the pocket floor to the bottom of the model. The bias starts at the pocket floor because this is the surface where aggressive milling occurs. The bias mesh allows the entire residual stress profile from hole drilling to be represented in the model elements. Element size follows the MIRS gradients, as suggested in [7], with 0.01 mm element size at the milled surface and increasing in size away from the milled surface. Tetrahedral elements are used in areas where the geometry is too complex for hexahedral elements. Hexahedral elements are used in areas where MIRS is applied, with the initial stress state interpolated to element centroids. Interpolated values define the initial condition for the FE analysis. The centroid coordinates are then computed from the nodal coordinates using the following equations,

$$X = \frac{sum(X_{nodal})}{N} \quad (1)$$

$$Y = \frac{sum(Y_{nodal})}{N} \quad (2)$$

$$Z = \frac{sum(Z_{nodal})}{N} \quad (3)$$

After interpolating the initial stress state to centroids, a subsequent solution for equilibrium provides a distorted geometry in terms of nodal displacements. To provide a solution for the boundary value problem, a boundary condition is established in the center bolt hole of the part.

To compare the surface form, an uncertainty determination from the model results is used. The residual stress measurements have uncertainty bars which represent the standard deviation of stress at each depth. The standard deviation of stress is applied as an input to the distortion prediction model. The surface form that is a result of the standard deviation is then used as uncertainty bands for the surface form produced by the model results.

2.2.5 Validation of the distortion prediction model

In order to validate the distortion prediction model, we developed three methods: (1) compare observed and predicted form of the bottom surface; (2) compare observed and predicted residual stress at selected locations on the pocket floor; (3) compare observed and predicted form of the bottom face after the floor is cut free of the feature sample.

A first validation is to compare the observed and predicted form of the nominally flat bottom face of the feature samples. The comparison is made qualitatively by using color maps to convey the overall surface form and then quantitatively by using line plots along a series of lines across the surface. The locations of the lines are along the bottom face at values of constant x (25, 100, and 175 mm) and y (15, 50, and 85 mm) as well as diagonally (positive and negative

diagonals from corner to corner of the surface form). The location of the line plots are shown in Figure 5. In the model prediction, uncertainty from the model is shown based off the uncertainty bars from the residual stress measurements. Measurements are made to assess the form bottom face of 3 mm and 7 mm feature samples using a TalyScan 250 laser scanning profilometer from Talyor Hobson. The profilometer measures surface height (z) at a grid of points with 0.2 mm spacing along both the x and y directions. The surface form data are trimmed to remove data points not belonging to the scanned surface. Observed and predicted surface form data are compared in a consistent frame by fitting each to a plane and subtracting the plane from the data. A datum zero is established computing the average of the surface form within a 15 mm radius at the center bolt hole and then subtracting that from all the data.

A second validation is to compare residual stress profiles measured experimentally by hole-drilling in the floor of the feature sample to the model inputs established using the thick plates. Figure 6 shows the locations of residual stress measurements, where one measurement is completed at the middle (M) of the pocket and 3 others toward three of the pocket corners (right (UR), lower left (LL), and upper left (UL)). The locations were chosen to get a comparison of the near surface of milling induced residual stress (MIRS) across the pocket surface. Measurements were performed on one 7 mm feature sample.

A third validation uses a sectioning step to isolate distortion of the pocket floor alone, which is helpful for isolating the effects of MIRS from those of bulk residual stress. The pocket floor is isolated and removed because this is the only surface where aggressive machining was performed. For the 3 mm and 7 mm samples, one pocket floor is sectioned and removed using wire electric discharge machining (EDM). The laser scanning profilometer is used to obtain the observed form of the bottom face of the removed pocket floor. The distortion model is used to

predict the form of the floor removed pocket floor by using an FE model where the domain (geometry) includes only the pocket floor. The observed and predicted distortions are compared by taking diagonal lines (positive and negative diagonals) of z-height from corner to corner of the sectioned pocket floor surface form, shown in Figure 7.

A flowchart was created to show connections among the various aspects of this work (Figure 8). The flowchart begins with the machined plate samples and ends with validation that comprises comparisons between observed and predicted quantities. The colors indicate different aspects of the work, with blues indicating physical measurements or material properties, green indicating modeling or computer simulation, and red indicating model validation (i.e., comparison between model estimates and physical observations).

2.3 Results

2.3.1 Initial stress state for near surface residual stress and bulk residual stress

Figure 9 shows the average of the residual stress versus depth profiles found on four milled plate samples. The average at each depth is computed from multiple measurements on each sample. The profiles for each plate demonstrate some consistency, with a hook shape for the direct stress components. The hook shape is consistent with expected MIRS in milled aluminum [2]. They also show some dispersions; notably a lower level of MIRS in sample A20. The MIRS data consistently trend toward 0 MPa after 0.20 mm depth. In the longitudinal direction, the depth of maximum stress occurs at 0.05 mm with peaks consistently near -150 MPa, except for plate A20, where the depth of maximum stress occurs at 0.06 mm with and peaks at -100 MPa. In the transverse direction, the depth of maximum stress occurs at 0.04 mm for plate B4 and A6. The maximum stress peaks for both plates are at -165MPa and -190 MPa

respectively. In the shear, the depth of maximum stress occurs at 0.04 mm for plates A20 and A18, and at 0.02 mm for plates B4 and A6. The stress values peaks at 85 MPa for plate A6, 55 MPa for plate B4, and 45 MPa for plates A20 and A18. The error bars for each milled plate sample reflect the standard deviation among the individual measurements taken on that plate.

The grand average stress versus depth profile, shown in Figure 10, is computed as the average of the average profile in each plate and is used as the initial stress state in the distortion model. The highest magnitude stress in the grand average is approximately -140 MPa in the milling direction occurring at 0.05 mm, -145 MPa in the transverse direction occurring at 0.05mm, and -55 MPa in shear occurring at 0.03 mm. The grand average stresses trend to zero in all directions at a depth of 0.2 mm. The error bars shown on the grand average reflect the standard deviation among the 4 milled plate samples from the averages of each plate. The standard deviation results in an estimate for the uncertainty in predicted distortion, as explained earlier.

Figure 11 shows the bulk residual stress in the σ_{xx} direction which is measured from slitting. The bulk residual stress peaks at a value of 15 MPa and is the lowest at -12 MPa. The bulk residual stress is applied only in the σ_{xx} direction, all other directions are assumed to have negligible bulk residual stress.

2.3.2 Validation – form of the bottom face

Figure 12 shows the observed and predicted distortion, which is the difference from the ideal flat surface, for the 7 mm and 3 mm feature samples. Figure 12a shows observed distortion along the bottom of the 7 mm feature sample, showing a saddle shape, which agrees with the model overall. The observed form has -0.010 mm z-height at the upper left and bottom right

corners and 0.030 mm at the upper right and bottom left corners. Figure 12c shows the predicted distortion of the bottom of the 7 mm feature sample. The predicted distortion is a saddle shape, distorting -0.025 mm at the upper left and bottom right corners and 0.025 mm at the upper right and bottom left corners, with center bolt hole being the reference datum (zero). Figure 12b shows the observed distortion along the bottom of the 3 mm feature sample, showing a saddle shape that agrees with the model overall. The upper left and bottom right corners show distortion of -0.08 mm, and the upper right and bottom left corners show distortion of 0.05 mm. Figure 12d shows the predicted distortion of the bottom of the 3 mm feature sample. The predicted distortion is a saddle shape, distorting -0.09 mm at the upper left and bottom right corners and 0.085 mm at the upper right and bottom left corners. The color scale used for the 3 mm sample is 3x the color scale used for the 7 mm feature sample. The predicted and observed distortion for the 3 mm and 7 mm sample are generally consistent, showing a saddle shape. There are differences in the magnitude of distortion, about 3x larger for the 3 mm sample compared to the 7 mm sample, which is consistent with the lower stiffness of thinner sections. There are also differences in magnitude of the observed form compared to the predicted, with the predicted generally overpredicting the observations.

To compare the model and observed form for the 7 mm and 3 mm sample, data are taken along various lines across the bottom face. The line plots for the 7 mm sample are shown in Figure 13. It is useful to compare the uncertainty bands in Figure 13 with the forms from Figure 12. The comparison shows that the uncertainty peaks along the edges of the surface, with greater uncertainty farther from the center bolt hole (the datum). The lines taken at x = 100 mm and y = 50 mm go through the center bolt hole of the part, and the heights are relatively small, with lower height for the observed than the model and the uncertainty for these line plots are not as large.

On lines closer to the edges of the part, the differences between the predicted and observed heights become more apparent, with the biggest difference seen in the lines taken at x = 25 mm and x = 175 mm. At x = 25 mm the observed data falls outside the uncertainty band after a distance of 35 mm and a very similar trend is seen at x = 175 mm, but at opposite ends of the y-direction. The line taken at y = 15 mm shows the observed data falls outside the uncertainty band after a distance of 100 mm, and a very similar trend is seen at y = 85 mm, but at the opposite ends of the x-direction. The positive diagonal line plot (g) has very good agreement between the observed and predicted form, with the observed data falling within the uncertainty for the predicted data except near zero, where the observed data falls outside the uncertainty bands. The negative diagonal (h) does not have good agreement, with the observed data falling outside the uncertainty bands for the predicted data. While the color maps of surface height (Figure 12) show the general agreement of observed and predicted form for the 7 mm feature sample, the line plots of Figure 13 show some discrepancy.

Figure 14 shows the line plots for the 3 mm sample. The lines taken at x = 100 mm and y = 50 mm also have relatively small heights, with lower height for the observed distortion. Similar to the 7 mm sample, it is useful to compare the uncertainty bands in Figure 14 with the forms from Figure 12. The comparison shows that the uncertainty peaks along the edges of the surface, with greater uncertainty farther from the center bolt hole (the datum). The edges of this sample also have larger differences between the predicted and observed heights, with the biggest difference seen in the lines taken at x = 25 mm and x = 175 mm. At x = 50 mm the observed data falls outside the uncertainty band for most points but there is general shape agreement, which also true for the line taken at x = 175 mm but in the opposite end of the y-direction. The line taken at y = 15 mm and y = 85 mm also shows the observed data falls outside the uncertainty

band, but there is good shape agreement, with the observed data following a similar to trend to the predicted data. The positive diagonal line plot (g) has good agreement between the observed and predicted form, but the observed data falls outside or on the uncertainty for the predicted data for most points. There is good shape agreement for the negative diagonal (h), but the observed data falls further outside the uncertainty bands than the positive diagonal. The line plots show better correlation between observed and predicted results for the 3 mm sample when compared to the 7 mm feature sample line plots.

Overall, there are distinct differences between the observed and predicted form along the bottom face of the 7 mm and 3 mm sample. In general, the magnitude and shape of distortion is similar, although the predicted generally overpredicts the observation. There is greater uncertainty along the edges of the sample, with the least amount of uncertainty around the center bolt hole (the datum).

2.3.3 Validation – residual stress measurements

Figure 15 compares the measured residual stress in the pocket area of the 7 mm feature sample to the grand average stress profiles used for model inputs (that were determined on the plate samples). In the length direction (σ_{xx}), at most locations σ_{xx} peaks around -140 MPa at a depth of 0.05 mm, except LL, which peaks at -125 MPa. The pocket peak stresses are within the standard deviation of the grand average peak stress. The stresses trend toward zero around 0.2 mm, except UR and LL which trend to 10 MPa, which is the level of residual stress found in low stress material [12]. In the transverse direction, at all locations σ_{yy} peaks around -150 MPa at a depth of 0.05 mm. The stresses trend toward zero at a depth of 0.2 mm, except UL, which stays around -40 MPa until a depth of 0.4 mm, where it trends toward zero. The shear stresses peak around -70 MPa at a depth of 0.04 mm for the LL and UL measurement, the other 2

measurements (UR and UL) peak at the first measured depth at a value -90 MPa. All values then trend toward zero at a depth of 0.15 mm. The data measured in the pocket floor are as expected given what was seen in the plate samples. This suggests that the model is useful, and that using the measured residual stresses in application to the FE model is a valid assumption.

2.3.4 Validation – isolated pocket floor form

Figure 16 shows the observed and predicted form of the isolated bottom face after pocket floor removal for the 7 mm and 3 mm samples. Note that the color scale for the 3 mm data is 5x that for the 7 mm sample. The observed and predicted shapes are similar for the 7 mm sample and 3 mm sample, however there is a rotation difference in the distortion, where the rotation of the distortion is referred to as the angle of maximum curvature. The angle of maximum curvature is measured from the x-axis, and the observed results rotate more than the predicted results in both the 7 mm and 3 mm thickness. There is also a machining line visible in the observed data for the 7 mm sample at y = 30 mm, which distorts the rotation. The predicted forms have nearly identical angles of maximum curvature. The magnitude of distortion is similar for the 3 mm and 7 mm samples, but the predicted forms have consistently more distortion than the observed forms.

Figure 17 shows diagonal line plots of the observed and predicted form for the 7 mm and 3 mm isolated pocket floor form. There is general shape agreement with the diagonal line plots, with the positive diagonal line plots (a,b) showing more height than the negative diagonal line plots (c,d) for both surface forms. The 7 mm surface form has an observed maximum height of 0.055 mm and a predicted maximum height of 0.038 mm. The agreement between the observed and predicted line plots for the positive diagonal is better than for the negative diagonal for the 7 mm sample. The 3 mm surface form has an observed maximum height of 0.27 mm and a

predicted maximum height of 0.22 mm. There is very good agreement between the observed and predicted forms along the negative and positive diagonals of the 3 mm sample.

The machining stresses put on the pocket floor creates an observed distortion that's consistent with what was predicted. The bottom face after the pocket floor removal demonstrates that isolating the pocket floor improves the distortion prediction. The observed distortion is consistently less than the predicted distortion, and the angle of maximum curvature is greater in the observed distortion. However, there is better agreement between observed and predicted distortion for the pocket floor than for the entire bottom face of the sample.

2.4 Discussion

2.4.1 Residual stress profiles and measurement techniques

One purpose of this study is to acquire the residual stress measurement data to be used as input to the distortion model. By taking multiple measurements across different plate samples, the grand average stress profiles provided a robust estimate of the near-surface machining stresses. Because the grand average stress profiles are a combination of data from 15 individual measurements, there was a reasonable assumption that they provide a useful model input. However, hole-drilling data from the multiple feature samples show similar, but slightly different residual stress profiles for different areas of the pocket. The differences in the results could be due to material variation, wearing of the tool, changes in the milling conditions beyond the scope of tool control, or an effect from the finite thickness of the pocket floor.

2.4.2 Bending moment method for model input to produce model distortion

Residual stress profiles were used as an input to a finite element model to determine the distortion prediction for these samples. The current method requires a high mesh refinement to

capture the values of the near surface machining stresses. Another method uses the measured residual stress profiles to calculate a through thickness bending stress field. This method is useful because it can be imposed in a relatively coarse mesh, which saves on computation time. The bending stress is then applied as stress linearly through the thickness to the model in the areas where aggressive machining occurs. The model shown previously will be called as the initial stress model, this new model will be known as the bending stress model. To establish the bending moment model, values of the principal forces, the location of the effective stress, and the principal angle are found for the grand average residual stress profile. These values are based on previous work in this material [12].

The previous work introduces a concept of layer average principal stresses and average depth. These values are based off the grand average stress profile, which uses the shape of the measured residual stress profile to determine values of force and centroidal distances. More information on this derivation can be found in the previous work [12]. Bending moments along each principal direction can then be computed (M_1 and M_2).

$$\bar{M}_2 = \bar{F}_1\left(\frac{t_w}{2} - h\right) \tag{4}$$

$$\bar{M}_1 = \bar{F}_2\left(\frac{t_w}{2} - h\right) \tag{5}$$

The thickness of the part is t_w (which is 3 mm or 7 mm from the machined pocket surface to the bottom depending on the sample). F_1 and F_2 are the forces along the principal directions and h is centroidal distance found from the effective stress area from the stress profile curve. The area moment of inertia is then found

$$I = \frac{1}{12} B t_w^3, \tag{6}$$

where B = 1 mm. The area moment of inertia and the bending moments can then be used to find the bending moment principal stresses that are applied to the centroids of the elements.

$$\sigma_1 = \frac{\bar{M}_1 y}{I} \tag{7}$$

$$\sigma_2 = \frac{\bar{M}_2 y}{I} \tag{8}$$

where y is the distance from the centerline to the centroid of the elements where the stresses are applied. The principal stresses are then used to find the normal stresses. The normal stresses are then added to the bulk residual stress. Since the bending moment model does not need to capture the near surface residual stress profile like the initial stress model, fewer elements are needed for mesh convergence. Less elements also allows the bending moment model to save on computation time. A more detailed explanation on the bending moment model will be explored in the next chapter.

The distortion from the bending moment model compared to the initial stress model for the 3 mm and 7 mm sample are shown in Figure 18. The general shape are nearly identical in both the initial stress and bending moment models, but bending stress model estimates significantly lower distortion. Line plots are taken along the positive and negative diagonals of the models to better compare the results (shown in Figure 19). The line plots are also shown with the uncertainty bands from the modeling results. In general, the bending moment falls within or just outside the uncertainty for the initial stress model. There is nearly identical shape agreement between the line plots, with the bending moment model consistently having less height than the initial stress model for both the 3 mm and 7 mm samples. Because the bending moment model saves on computation time, it will be used in the following chapter for predicted and observed comparisons.

2.4.3 Discussion on the validation techniques

The three validation techniques are chosen to assess the distortion in distinct ways. The first method to validate the model was to compare the bottom face distortion of the model and the machined samples. This validation technique is used because it is a direct comparison between the predicted model and observed results of the sample. The bottom face was chosen due to its large flat surface area and to maximize the area for comparison, but the distortion comprises the entire 3-D geometry of the sample. The largest flat surface was also chosen because it makes it desirable for distortion measurements [19]. Future research could assess this for multiple surfaces on this sample. In general, the surface forms of the bottom face are similar between the observed and predicted results, but there are distinct differences. The predicted results generally overpredict the observed results, and the line plots show shape differences. There are general trends, with the observed and predicted data being more comparable toward the middle of the surface form. The uncertainty increases towards the edges of the surface, where more distortion occurs, and that is also where the observed and predicted data differ the most. The 7 mm sample has less distortion, and therefore less agreement than the 3 mm sample.

The second validation technique was chosen because it is a direct assessment of the residual stresses in the sample. The residual stress profiles from representative plate samples compare well to the residual stress profiles in the pocket floor of the feature sample. The data from the pocket floor compare reasonably well to the grand average stress profiles being consistent with σ_{xx} peaking around -140 MPa and σ_{yy} peaking around -150 MPa (Figure 15). The consistency supports the approach of using residual stress measured on a simple geometry (the plate sample) to predict the distortion of parts with more complex geometries.

The third method to validate the model involved removing the pocket floor and comparing the measured and modeled isolated floor distortion. The value of this comparison is isolating the areas of the sample where aggressive machining occurs. By removing the pocket floor the influence of the bulk residual stress in the walls is removed and the model becomes more simplified. The simplified model helps analyze the distortion prediction method when aggressive machining has more influence over the overall distortion. The comparison between model and measurement for the 7 mm and 3 mm isolated pocket floor have consistent amounts of distortion, with the 3 mm samples having approximately 5x the distortion of the 7 mm samples. There is general agreement in the amount of corner-to-corner distortion, and the angles of maximum curvature. The measured surface height maximum is consistently less than the predicted height range, a trend consistent with the form of the feature samples as a whole. Removing the pocket floor from the feature sample isolates the roughing machining stress, since aggressive machining is mainly completed in the pocket floor. The distortion prediction method is validated by this model because the predicted distortion and observed distortion agree well. There is also improved agreement in the pocket floor compared to the agreement along the bottom face of the feature sample. There could be additional factors which are influencing the distortion along the bottom face of the feature sample which result in less agreement between predicted and observed. Future work could explore these factors.

2.4.4 Sidewalls and bottom of the sample and their influence on the distortion

The feature sample distortion prediction assumes that the distortion is caused only by MIRS on the pocket floor and the bulk residual stress in the material. To further assess the adequacy of this assumption, hole-drilling measurements were completed in the inner and outer endwall of the 7 mm feature sample. Endwall measurements were completed by removing the

shorter end of the sample using a EDM. The hole-drilling measurement locations for the endwall are shown in Figure 20.

Figure 21 shows the residual stress profiles for the outer endwall measurements. Stresses along the length of the outer endwall exhibit near surface tension, ranging from 100 MPa to 150 MPa, and then quickly trending to 0 MPa at depth of 0.04 mm. Stress along the feature sample thickness in the endwall exhibits near surface tension, ranging from 100 MPa to 150 MPa that quickly trends to 0 MPa at 0.035 mm depth. Shear stress is consistently near zero.

Figure 22 compares the inner and outer endwall residual stress profiles to the grand average stress profiles. The endwall data comprise the average of data from the three individual measurements on the inner and outer endwall. Both surfaces show shallow near surface equibiaxial tension, which is very small and much different than the stresses produced by roughing and given by the grand average.

Four hole-drilling measurements were also completed on a plate sample that had been milled with the same indexable tool and machining conditions used to mill the bottom face of the feature sample. Figure 23 shows the average of the residual stress profiles obtained and a comparison with the grand average stress profiles. The stresses caused by the indexable tool are very small compared to the grand average stress profiles.

While the residual stress data from the endwall and bottom surface support the assumption that MIRS at these surfaces can be ignored, we can use the data to provide an updated distortion estimate. The updated model accounts for inner and outer endwall stresses. These stresses are applied to the endwalls and to the sidewalls in areas where the sidewalls are

straight and not in areas where the sidewalls curves around the bolt holes because of the complexity of those sections.

Figure 24 compares results of the updated model to results of the original mode. The differences are slight, which supports the assumption of the original model that the sidewalls and bottom face had negligible MIRS and can be left out.

2.5 Conclusion

This study assessed a distortion prediction method using FE modeling for complex geometries. The material used in this study was AA7050-T7451, an aerospace grade aluminum alloy milled with aggressive machining parameters. Measured residual stress profiles from plate samples were used as an initial stress condition to the FE model. Validation techniques were proposed to assess the distortion prediction method.

There are distinct differences between the observed and predicted bottom face of the feature sample. Line plots taken along the surface form show disagreement outside the uncertainty for both the 3 mm and 7 mm sample. However, the FE model does predict the general magnitude and shape of the observed sample, with the 3 mm observed and predicted results distorting about 3x as much as the 7 mm observed and predicted results. The measured residual stress profiles taken in the pocket of the feature sample generally agree with the applied grand average stress profile. The agreement of the profiles supports the application of stress from representative material to the model. Isolating and removing the pocket floors show better shape agreement between observed and predicted results compared to the agreement for the bottom face of the entire sample. Isolating the area on the sample where machining stresses occur simplifies the distortion prediction method.

Assuming that the residual stresses in the sidewalls and bottom face of the sample were negligible for the initial model was valid. The residual stress measurements in the sidewalls and bottom face of the sample showed very little residual stress, except for slight near surface tension in both the longitudinal and transverse directions. Since the near surface tension is relatively small compared to the total thickness of the sidewalls, it has little effect on the overall distortion of the model.

2.6 Tables

Table 1 – Depth schedule of the fine-depth increment hole-drilling used to assess near surface residual stresses [12]

Increment mm	Depth mm
0	0
0.0127	0.0127
0.0127	0.0254
0.0127	0.0381
0.0127	0.0508
0.0127	0.0635
0.0127	0.0762
0.0127	0.0889
0.0127	0.1016
0.0127	0.1143
0.0127	0.127
0.0254	0.1524
0.0254	0.1778
0.0254	0.2032
0.0254	0.2286
0.0254	0.254
0.0254	0.2794
0.0508	0.3302
0.0508	0.381
0.0508	0.4318
0.0508	0.4826
0.0508	0.5334
0.0508	0.5842

Table 2 - Summary of plate samples and the number of hole drilling measurements completed on each plate sample

Plate Sample ID	Hole Drilling Measurements
B4	6
A20	3
A18	3
A6	3

2.7 Figures

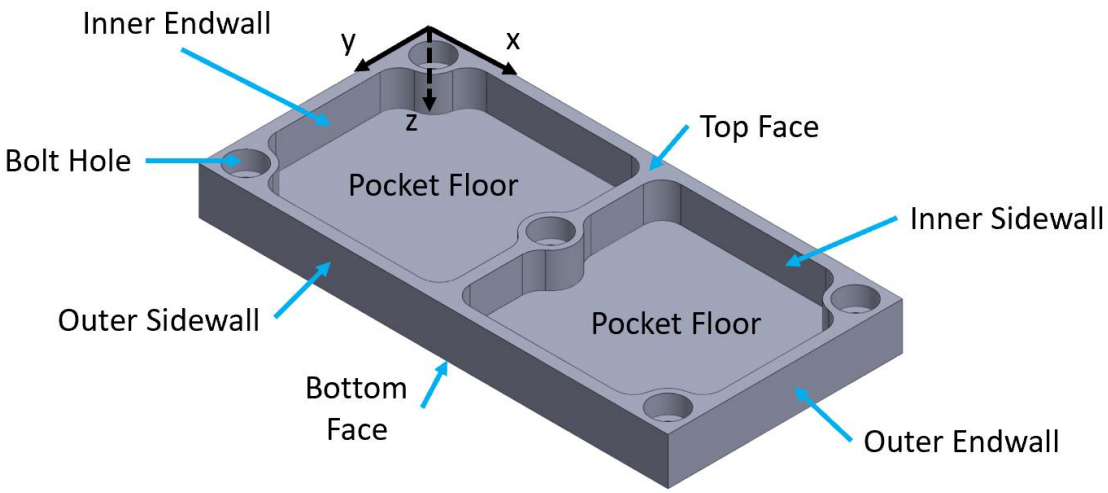

Figure 1 – Feature sample overview with labeling of regions and coordinate system

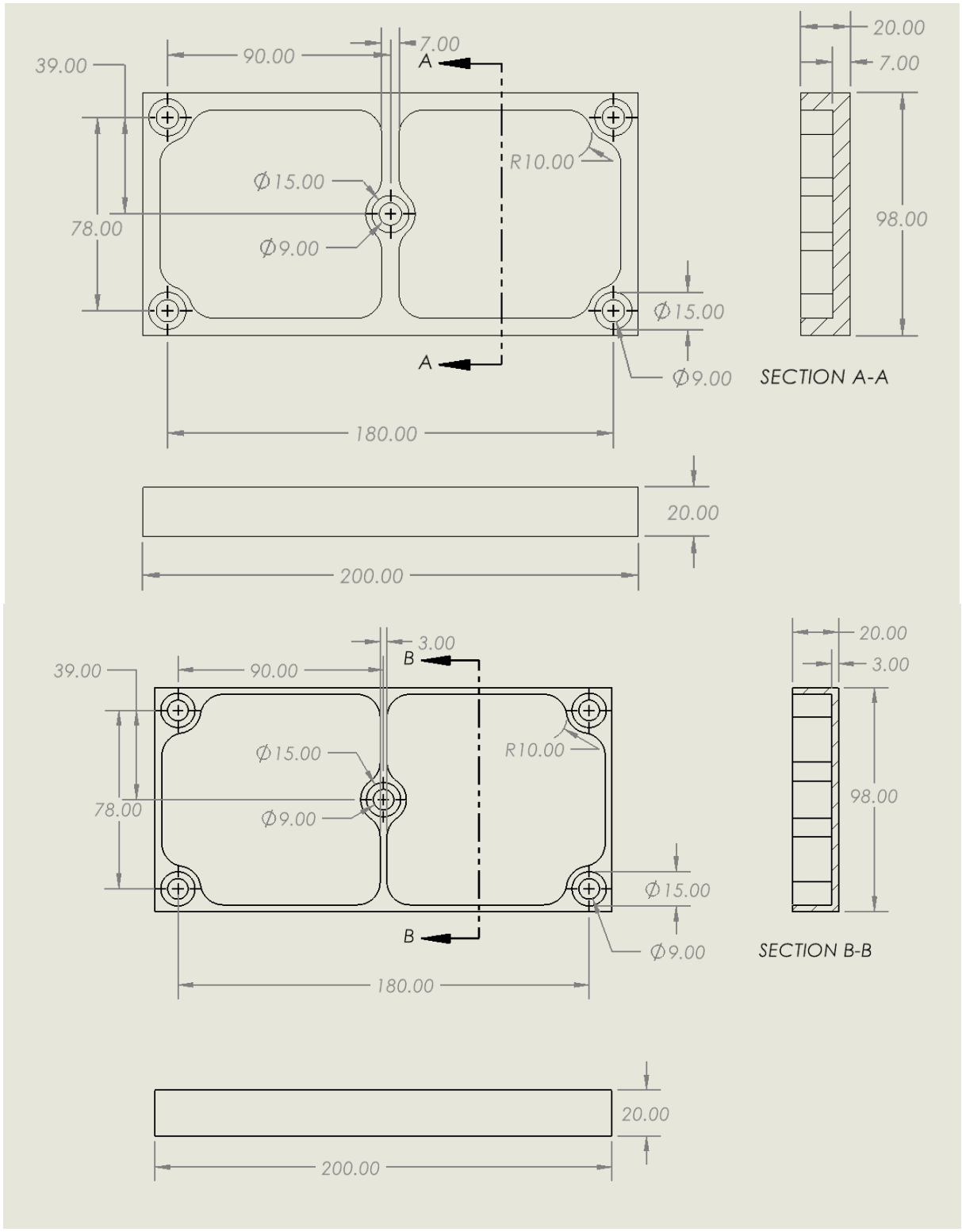

Figure 2 – Feature sample with 7 mm (top) and 3 mm (bottom) walls (dimensions in mm)

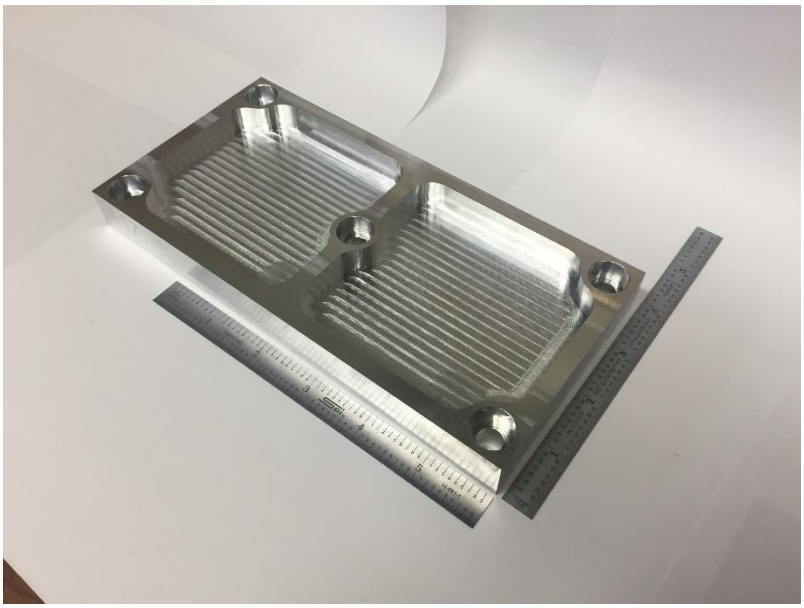

Figure 3 - Feature sample A17 with 7 mm walls; the lay on the pocket floor is a result of the aggressive milling

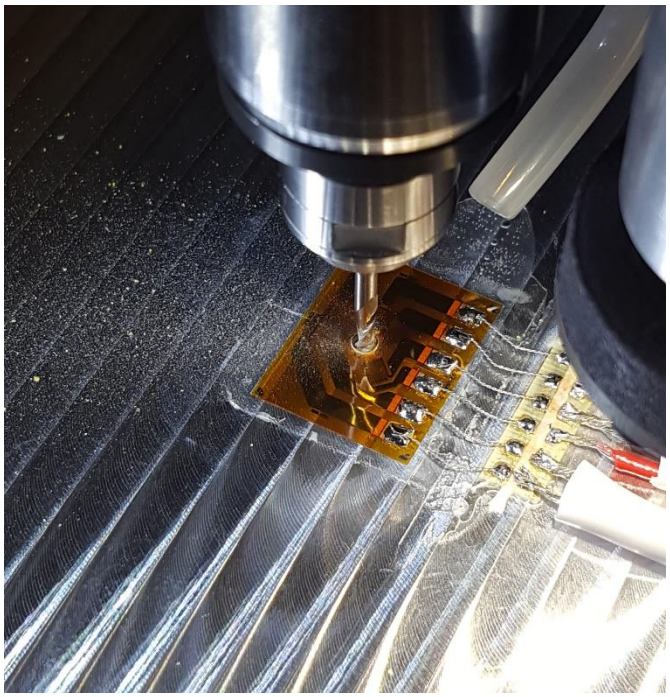

Figure 4 - Hole drilling experimental set-up

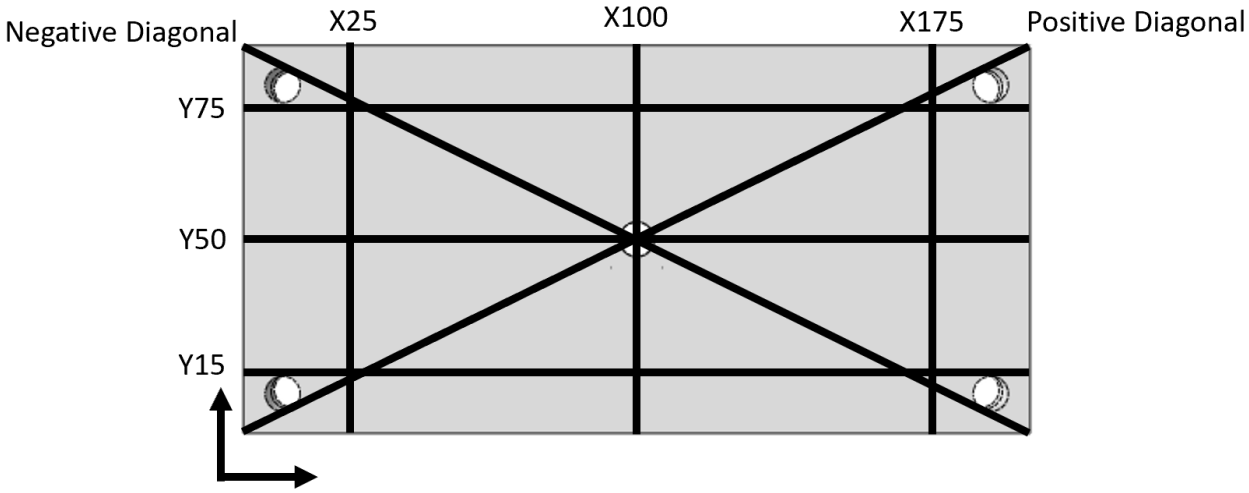

Figure 5 - Location of line plots along the bottom surface of the feature sample

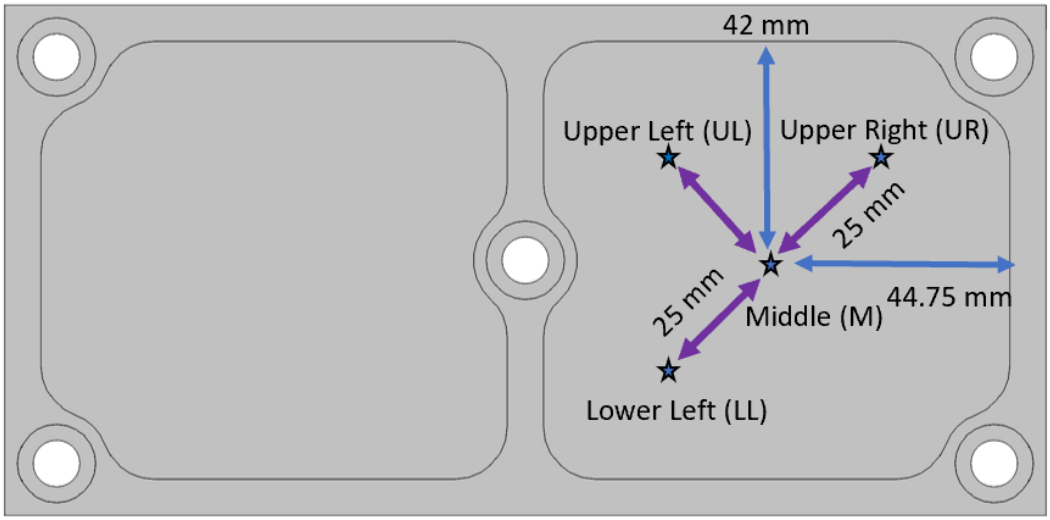

Figure 6 - Location of hole-drilling measurements on the pocket floor of the 7 mm feature sample

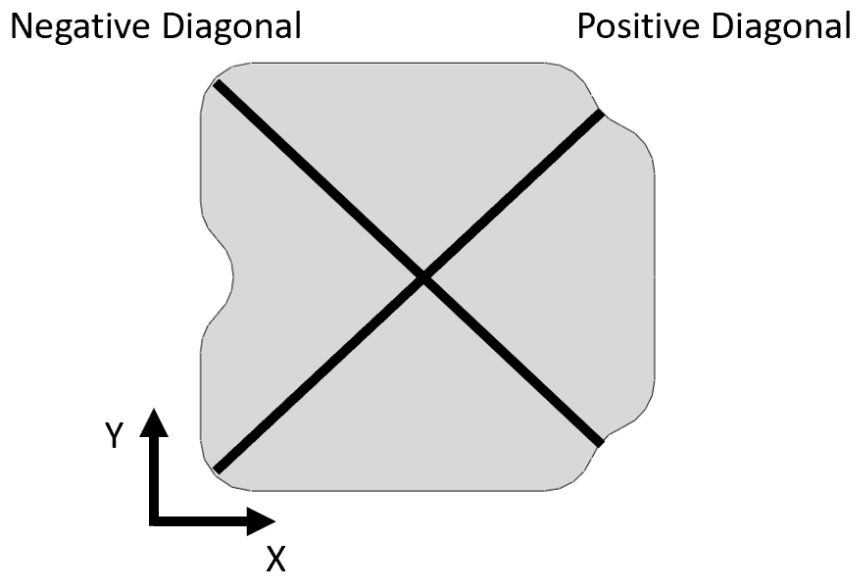

Figure 7 - Location of the line plots along the bottom surface of the pocket floor removal

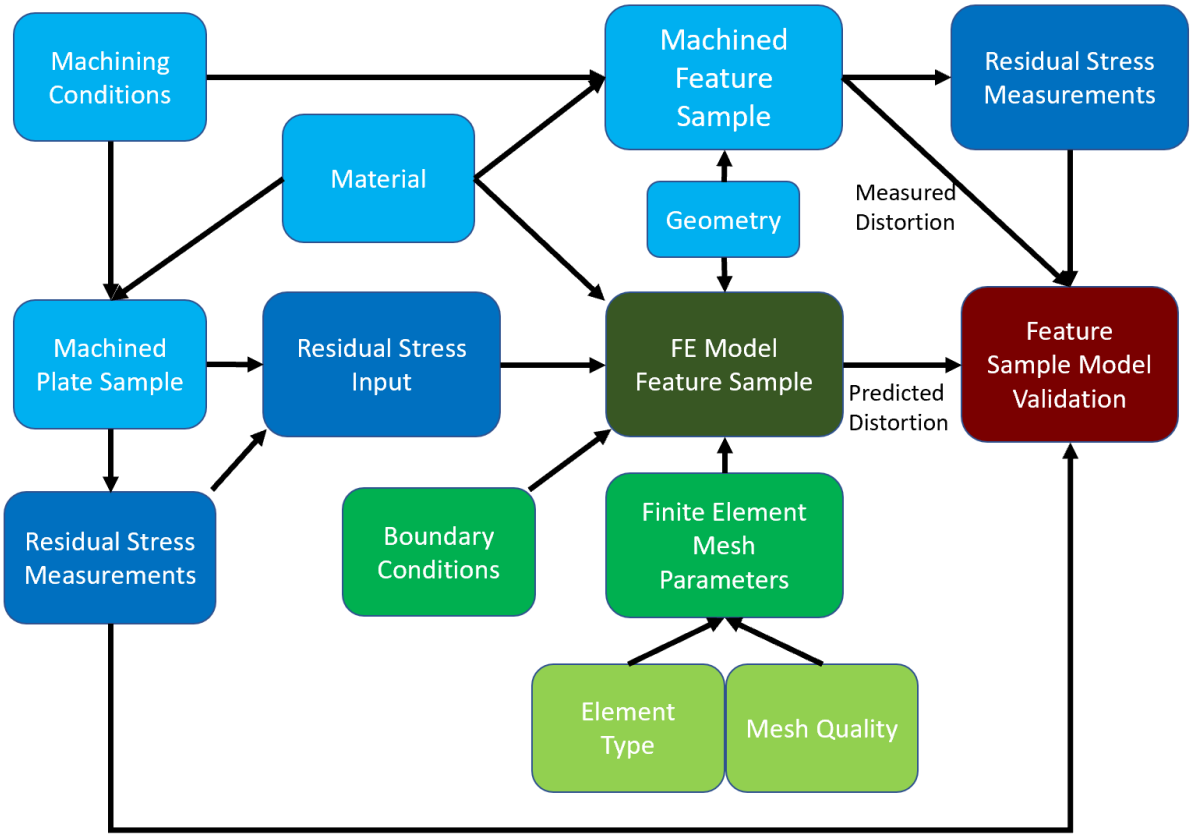

Figure 8 - Flowchart of process to determine and validate prediction of distortion using a FE model. Light blue indicates physical measurements or machining, dark blue indicates residual stress usage and measurement, light green indicates model parameters, green indicates model inputs, dark green indicates the model, and the model is compared to dark red which is the validation steps

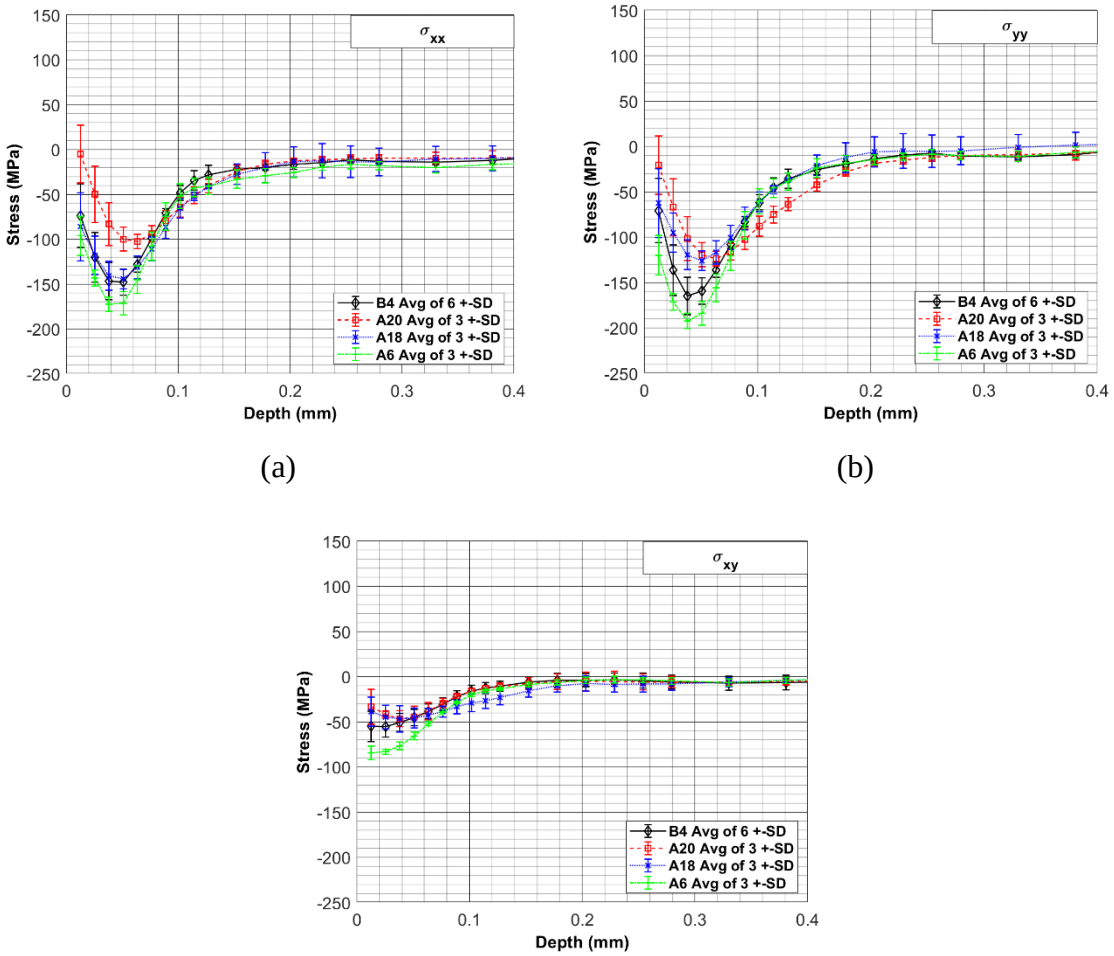

Figure 9 – Summary of residual stress measurement data for plate samples B4, A20, A18, and A6 showing average (avg) depth profiles with error bars showing standard deviation (SD) among measurements with error bars showing: (a) σ_{xx} (b) σ_{yy} (c) σ_{xy}

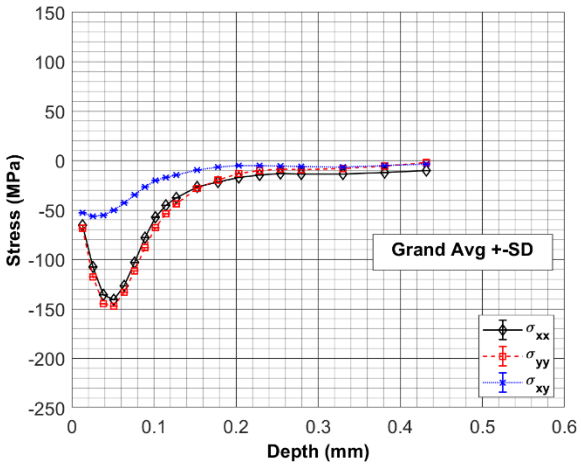

Figure 10 – Grand average residual stress depth profiles with error bars showing standard deviation (SD) among average of samples

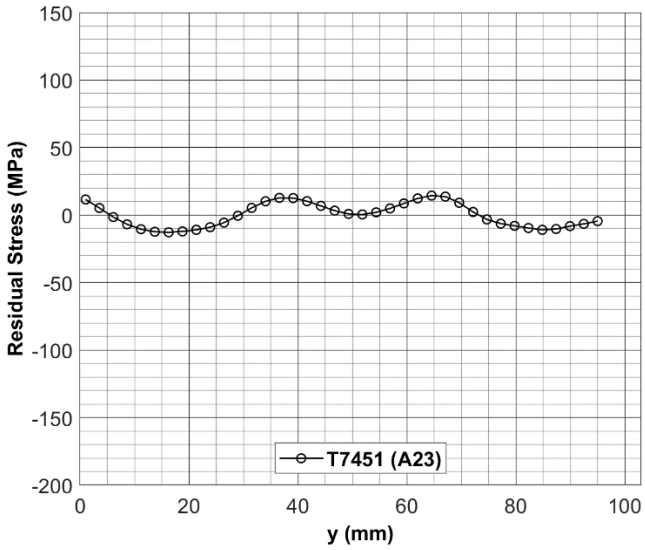

Figure 11 – Bulk residual stress for T7451 material measured from slitting [12]

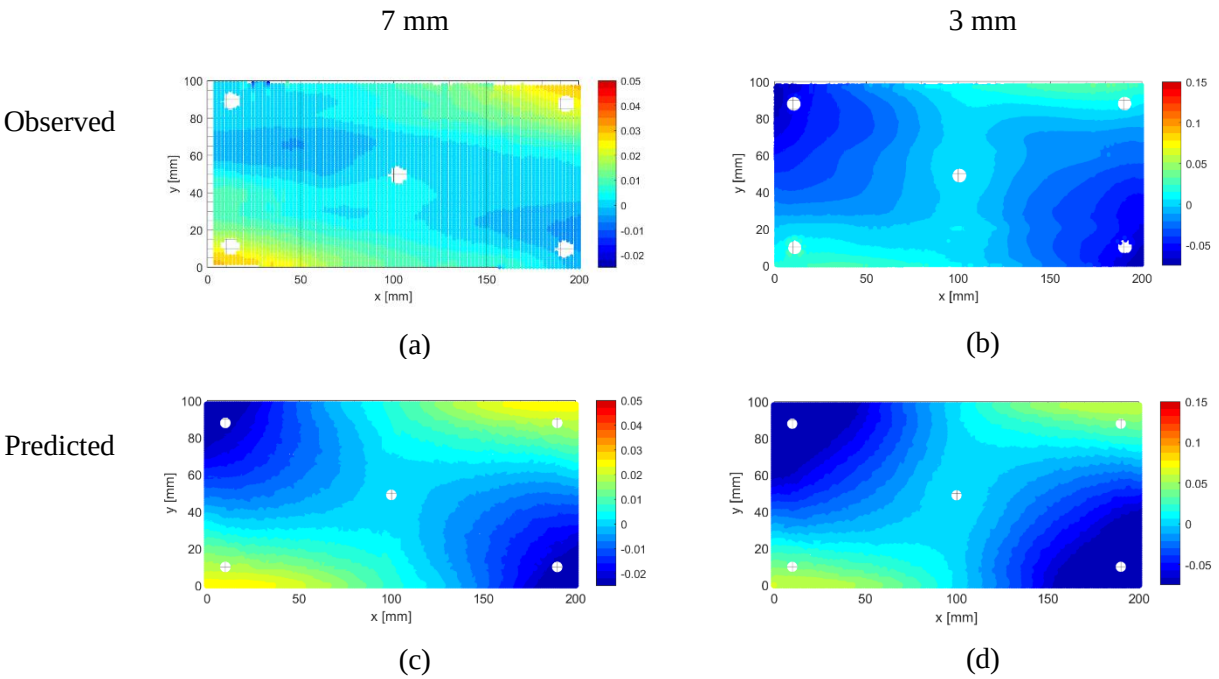

Figure 12 – Observed (upper) and predicted (lower) form of the bottom face of the 7 mm (left) and 3 mm (right) feature samples

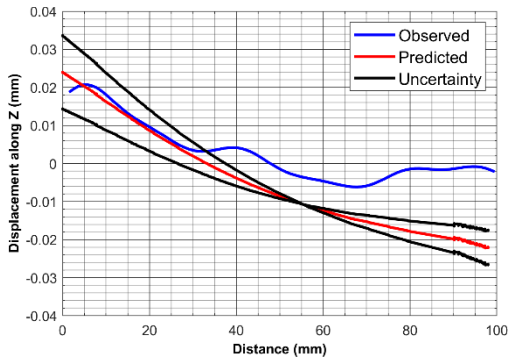

(a) x = 25 mm

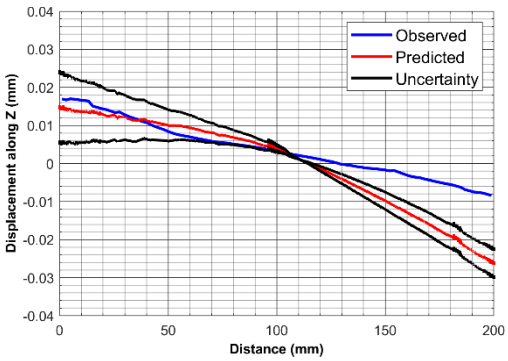

(b) y = 15 mm

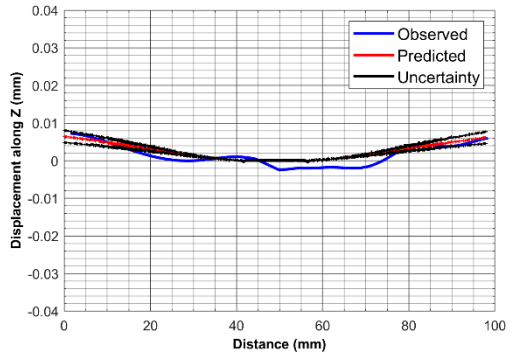

(c) x = 100 mm

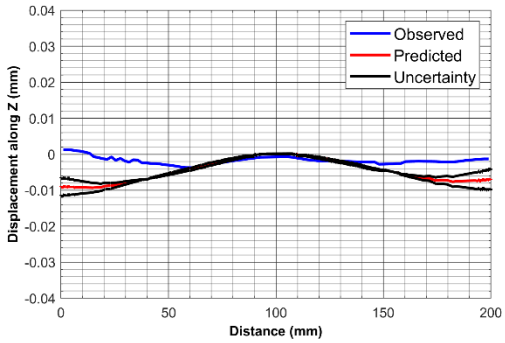

(d) y = 50 mm

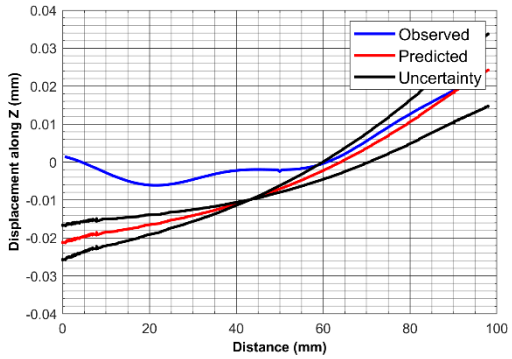

(e) x = 175 mm

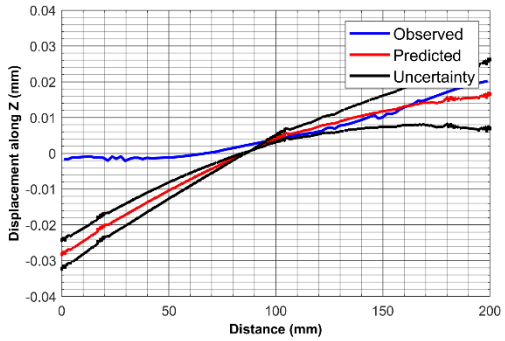

(f) y = 85 mm

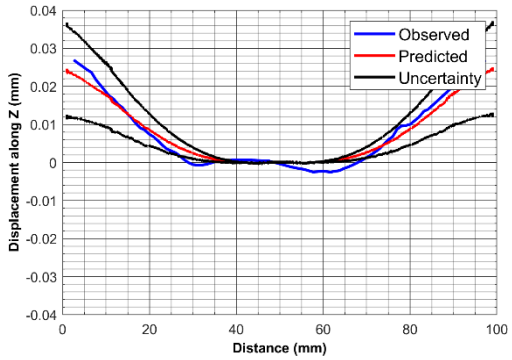

(g) Positive diagonal

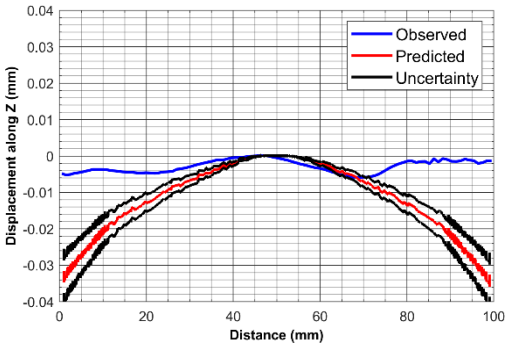

(h) Negative diagonal

Figure 13 – 7 mm, line path milling: line plots of bottom surface form along various paths including model uncertainty (±1 sigma)

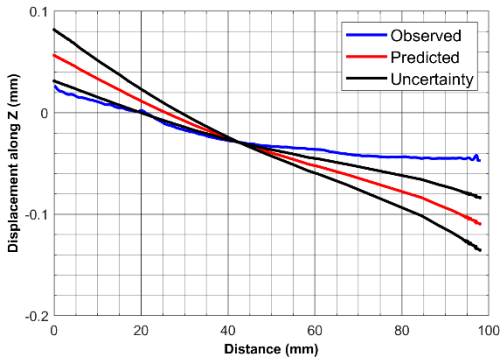

(a) x = 25 mm

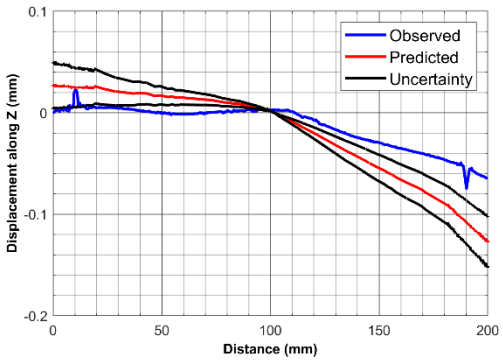

(b) y = 15 mm

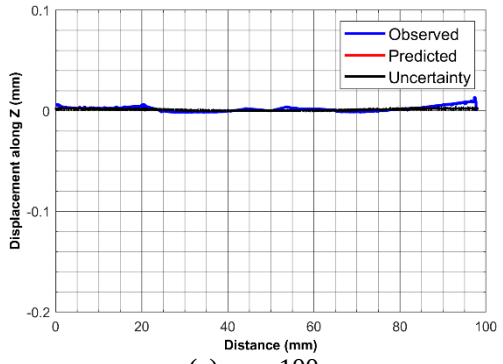

(c) x = 100 mm

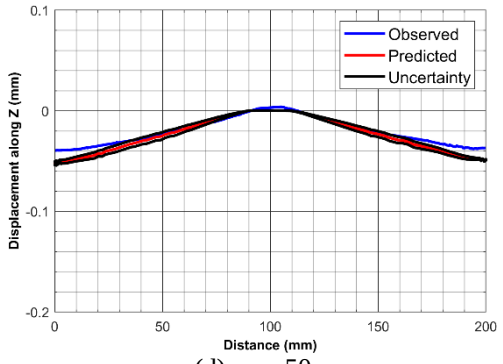

(d) y = 50 mm

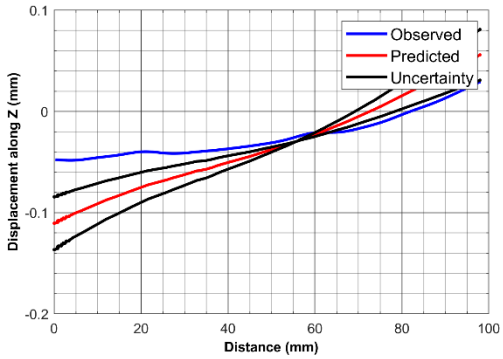

(e) x = 175 mm

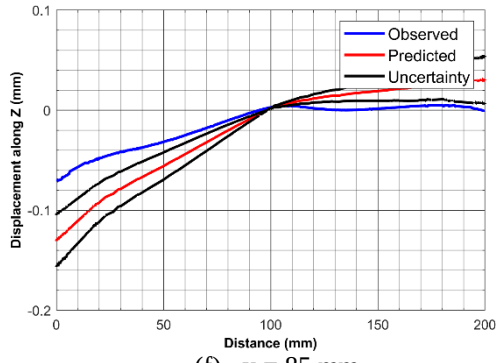

(f) y = 85 mm

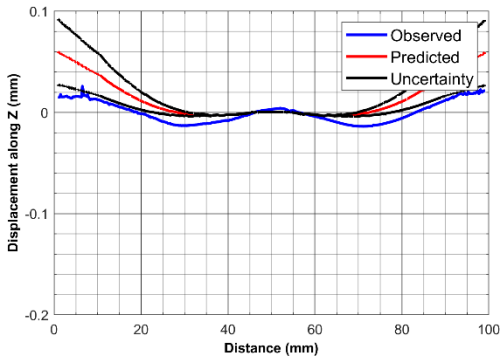

(g) Positive diagonal

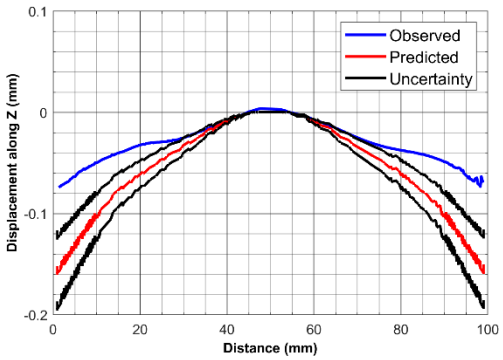

(h) Negative diagonal

Figure 14 – 3 mm, line path milling: line plots of bottom surface form along various paths including model uncertainty (±1 sigma)

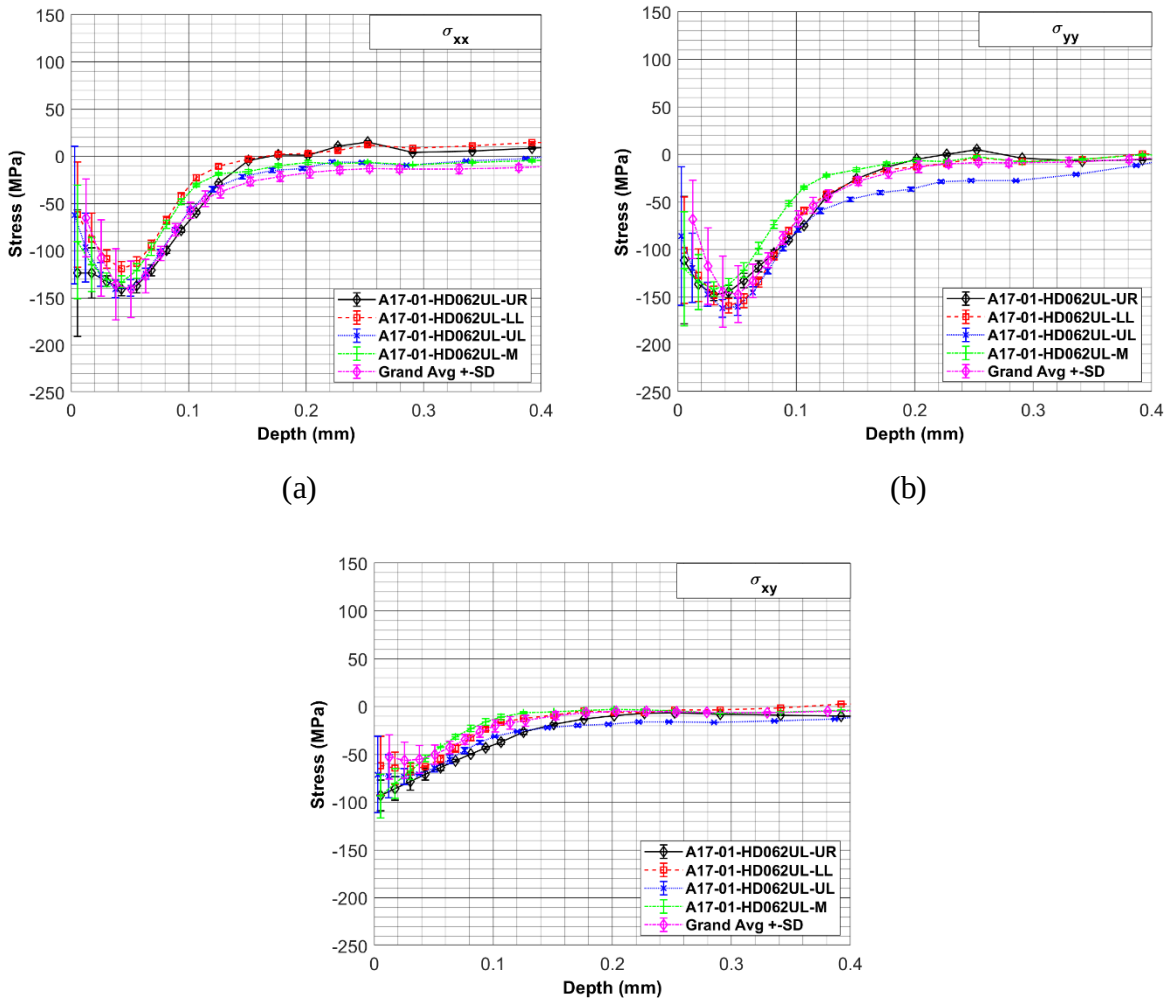

Figure 15 - Residual stress measured in the pocket on the surface of the 7 mm feature sample compared to the grand average stress profile: (a) σ_{xx} (b) σ_{yy} (c) σ_{xy}

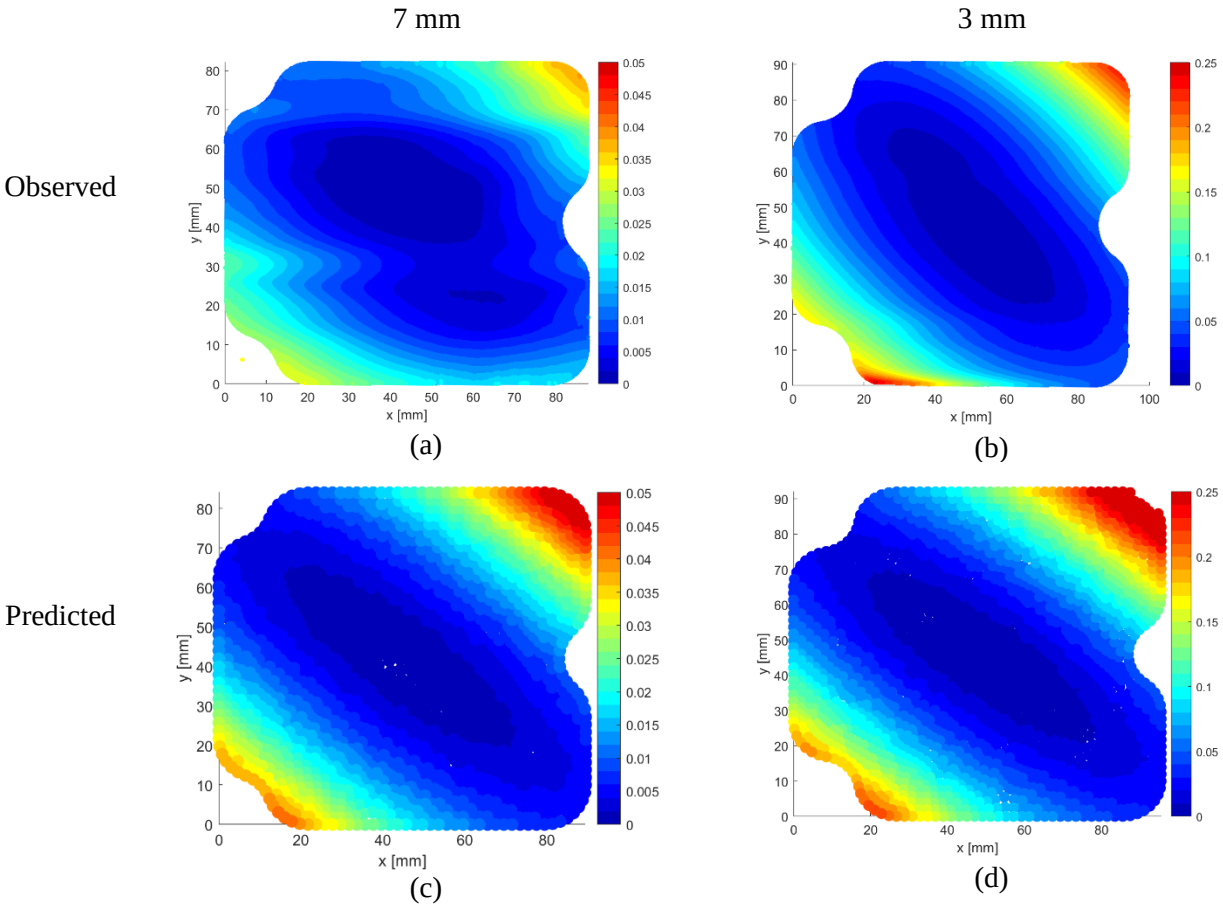

Figure 16 – Form of the bottom face after the pocket floor is cut from the 7 mm (left) and 3 mm (right) feature sample. Observed results (top) and predicted model results (bottom). Note that the color scale for the 3 mm data is 5x that for the 7 mm sample.

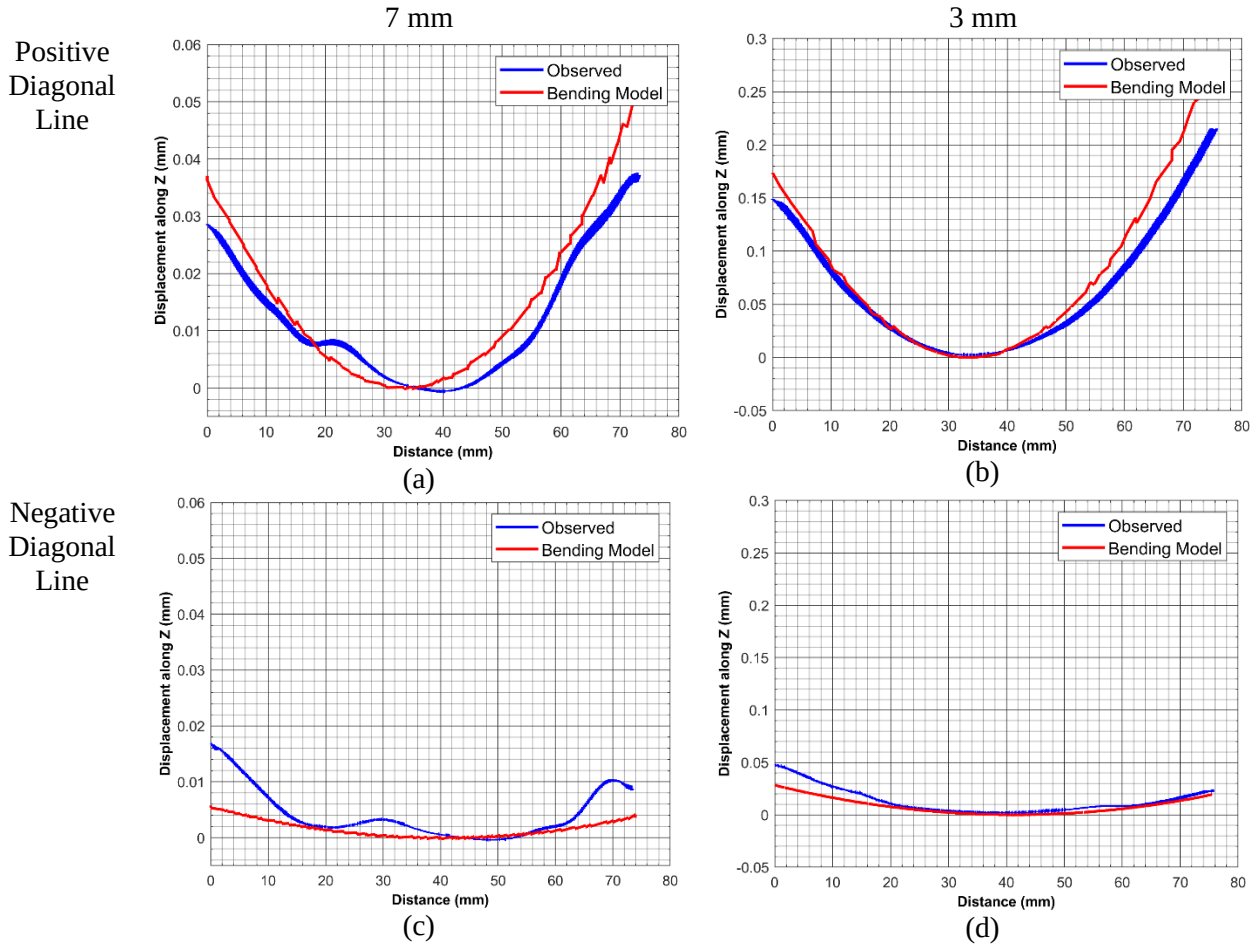

Figure 17 – Diagonal line plots of observed and predicted bottom surface form after the pocket floor removal for the 3 mm and 7 mm samples

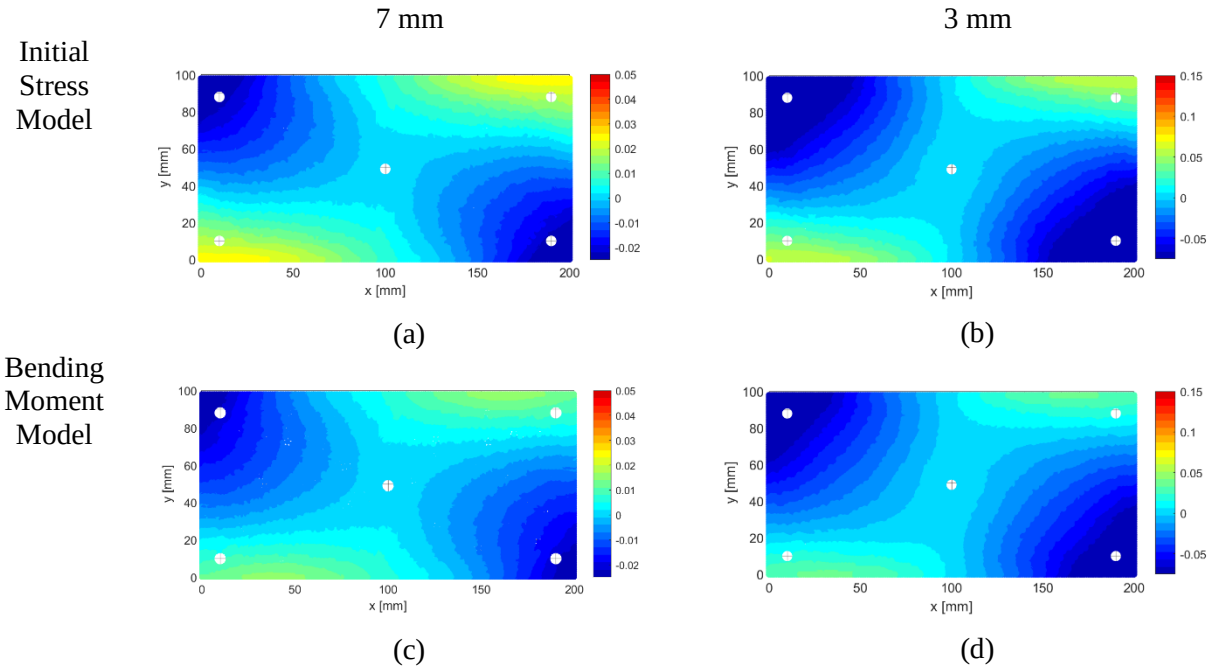

Figure 18 – Initial stress model (upper) and bending moment model (lower) form of the bottom face of the 7 mm (left) and 3 mm (right) feature samples

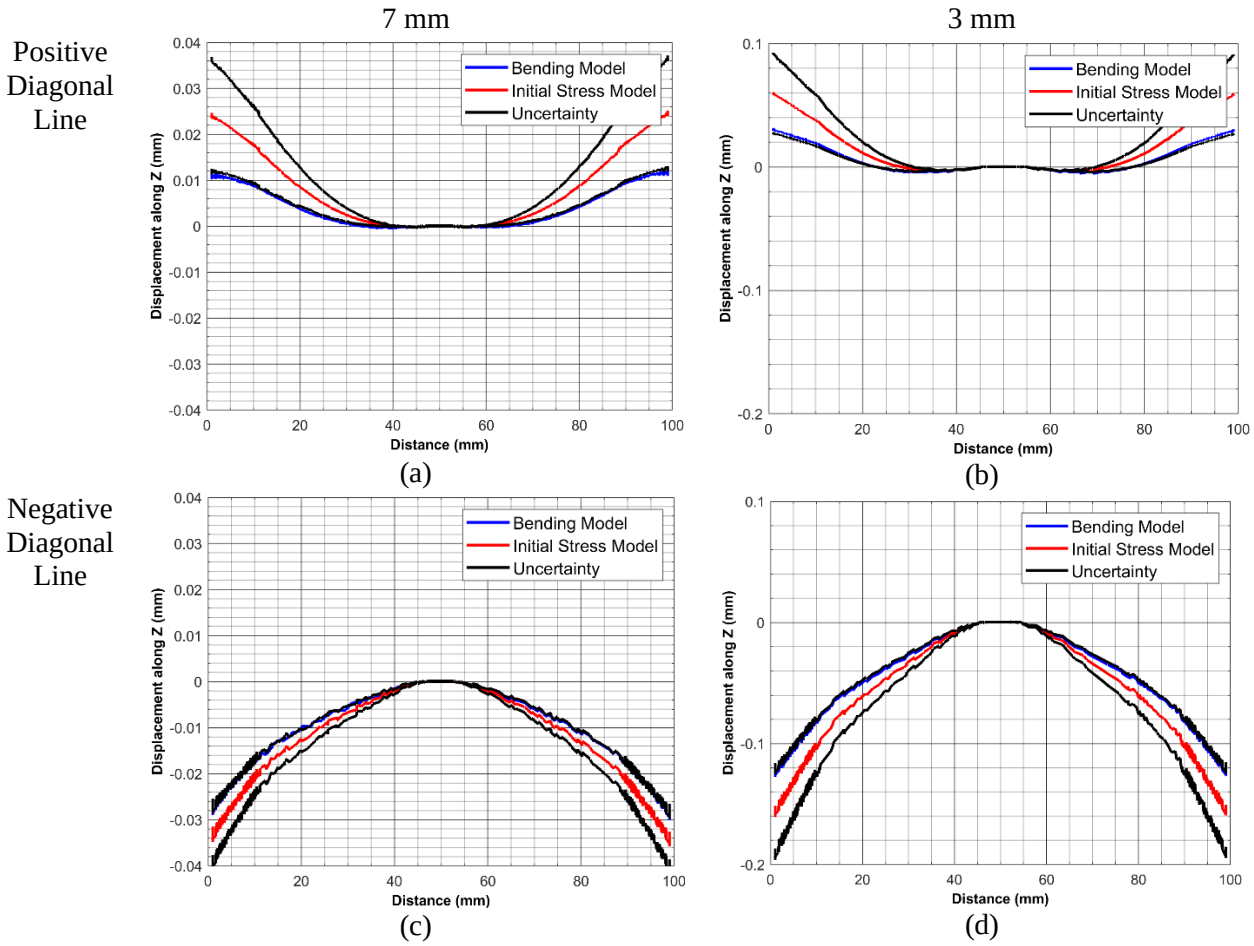

Figure 19 – Diagonal line plots of the bottom surface form of the 7 mm and 3 mm feature samples comparing the bending model to the initial stress model including model uncertainty (±1 sigma)

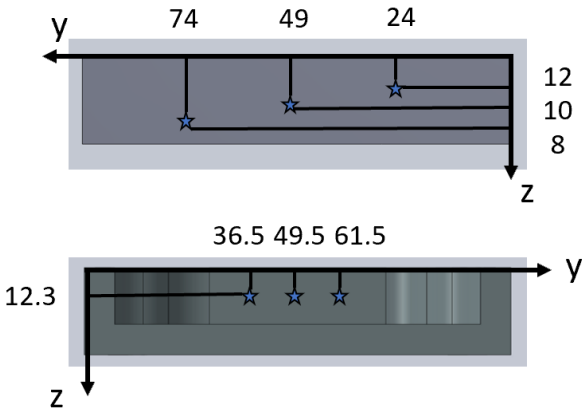

Figure 20 – Location (in mm) of hole-drilling measurements on the endwall outer (above) and inner (below) surface

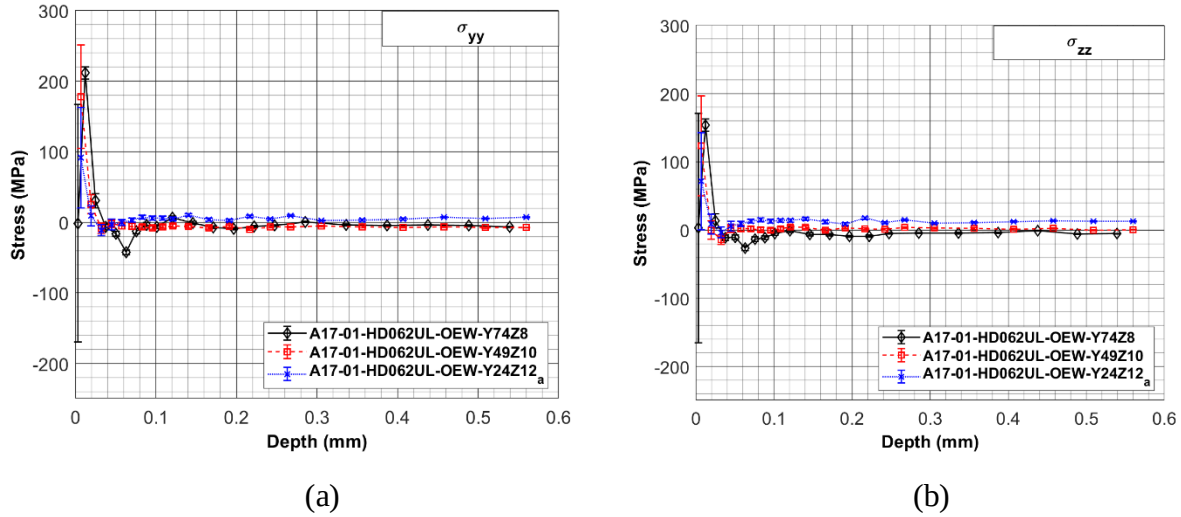

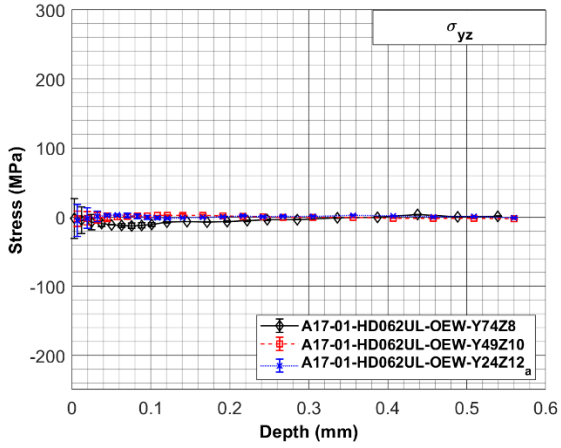

Figure 21 - Residual stress profiles for the outer endwall: (a) σ_{xx} (b) σ_{yy} (c) σ_{xy}

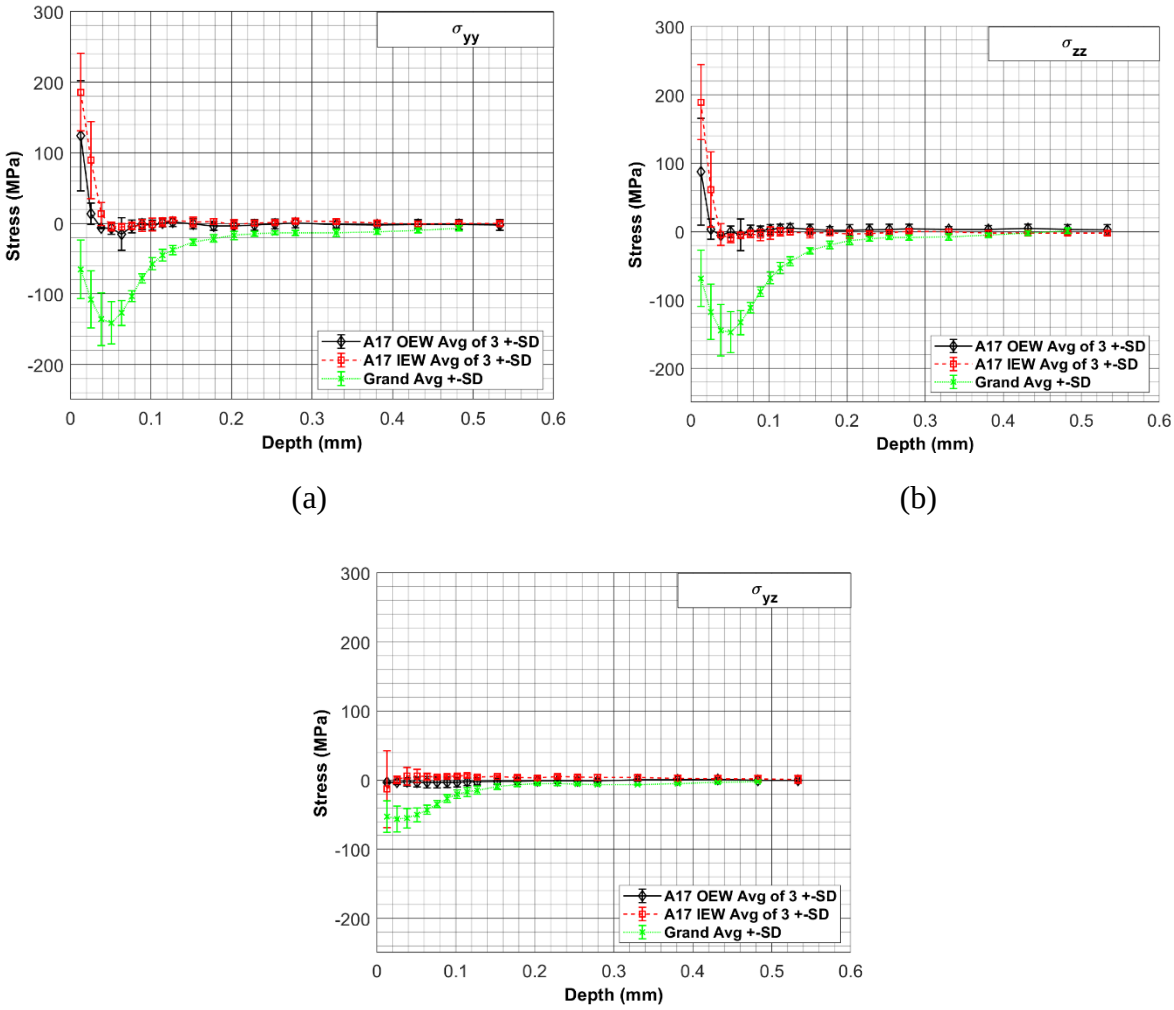

Figure 22 - Residual stress profiles for the average of the inner and outer endwall measurements compared to the grand average stress profile (error bars show standard deviation (SD) among the three measurements): (a) σ_{xx} (b) σ_{yy} (c) σ_{xy}

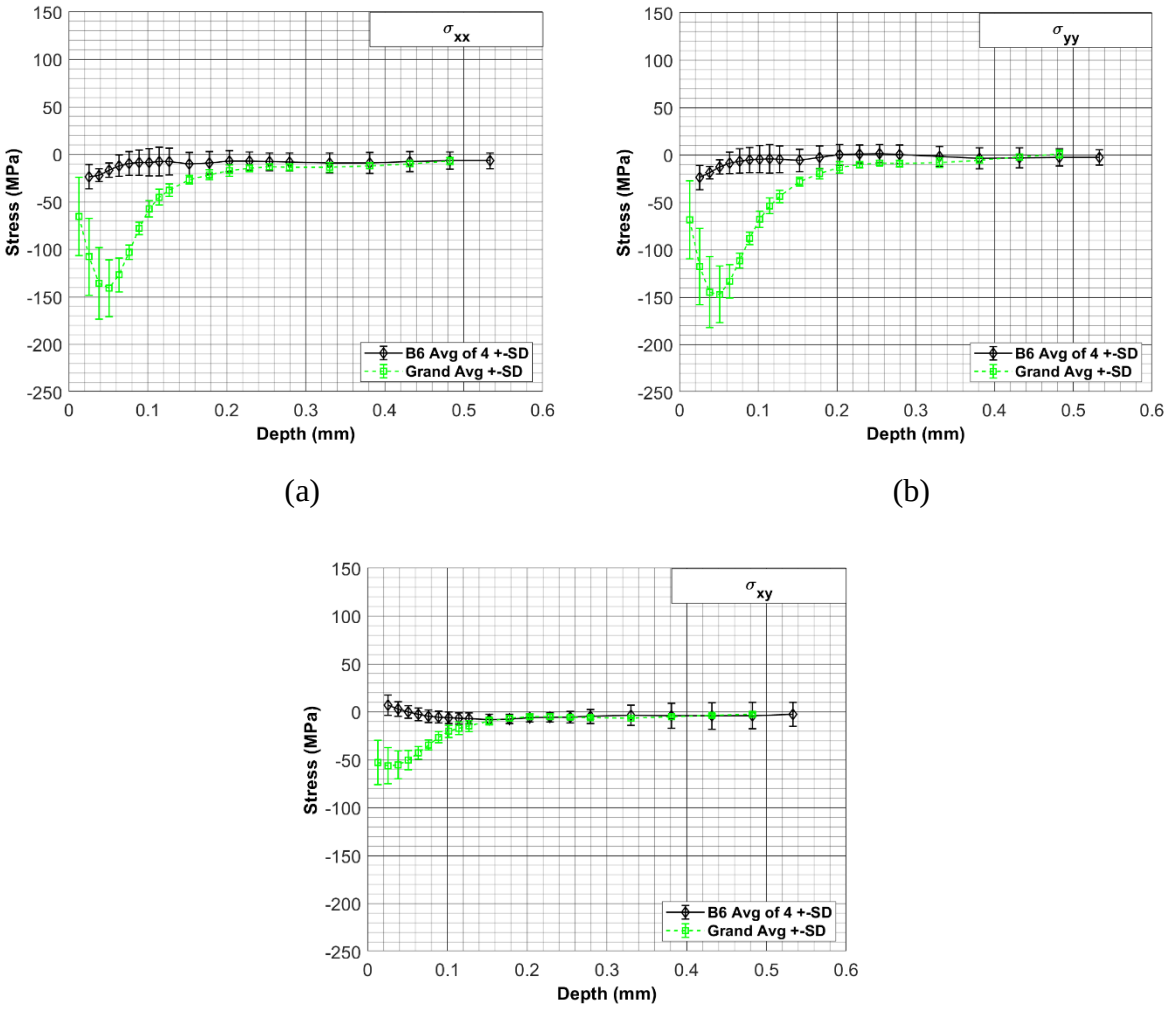

Figure 23 - Residual stress profiles from a plate sample (B6) machined with an indexable tool (as also used on the bottom of the feature sample) compared to the grand average stress profiles: (a) σ_{xx} (b) σ_{yy} (c) σ_{xy}

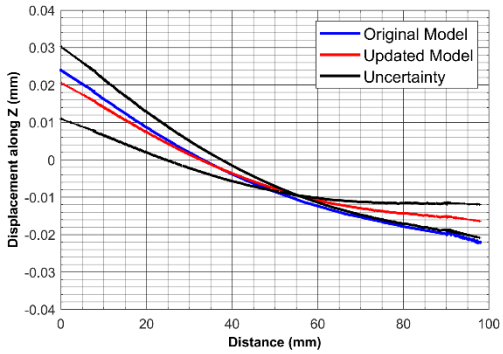

(a) x = 25 mm

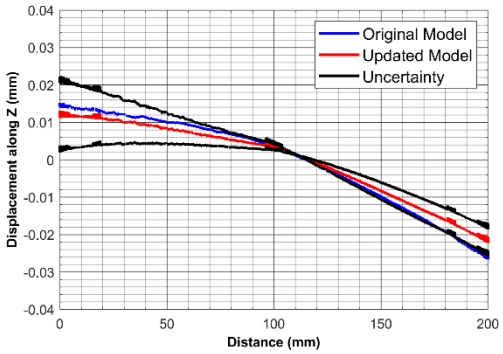

(b) y = 15 mm

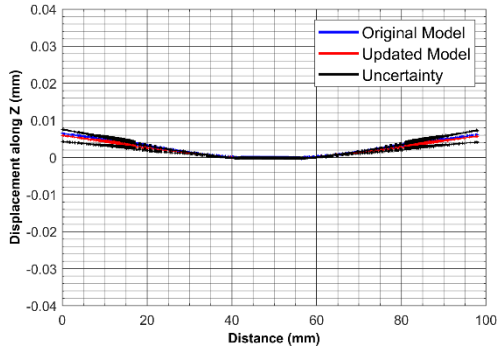

(c) x = 100 mm

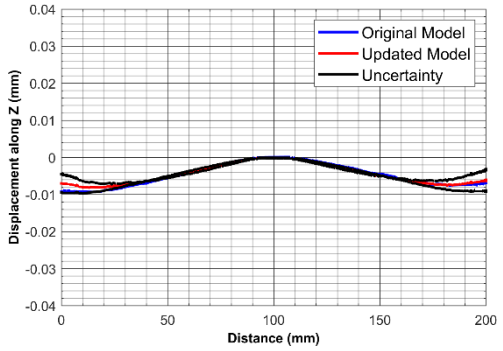

(d) y = 50 mm

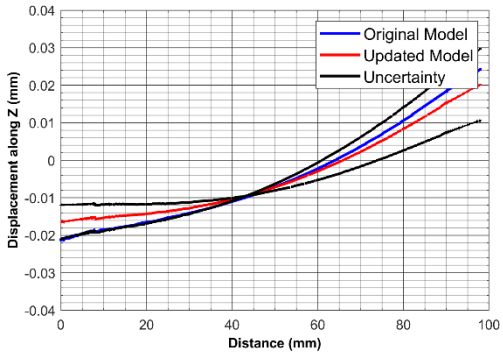

(e) x = 175 mm

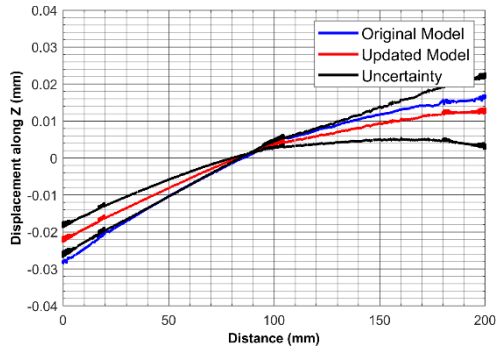

(f) y = 85 mm

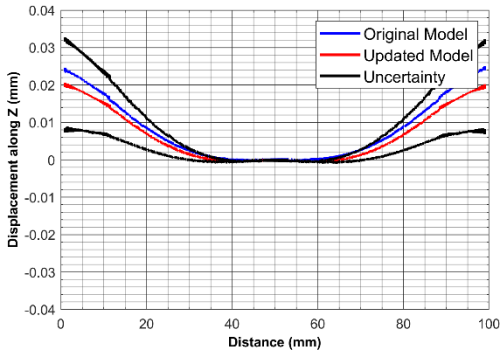

(g) Positive diagonal

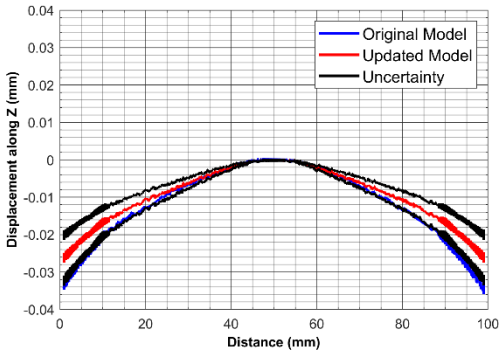

(h) Negative diagonal

Figure 24 – 7 mm, line path milling: line plots of the predicted form of the bottom face along various paths ignoring or including MIRS in the sidewalls and bottom surface

Chapter 3 – Validation of the Feature Sample Distortion Prediction Method for Complex Cases

3.1 Introduction

This chapter will add complexity to the distortion prediction method by analyzing the same workpiece with more complex machining and a different material condition. The prior chapter introduced that distortion from residual stresses can be modeled using different methods. Some of these methods include modeling of the machining process [6], equivalent bending stiffness calculations [8], or residual stress fields established from measurements. This chapter will again explore models based on residual stress fields established by measurements.

Machining tool paths are an important aspect of the manufacturing process. Different tool paths can minimize part distortion, as explored by Madariaga et al. [5]. Li et al. investigated the effect that path strategy had on the residual stress and distortion and used finite element models to predict the distortion of a thin-walled part [20]. They developed a thermomechanical model to analyze the distortion in parts with different features and path strategies and concluded that the smallest distortion resulted when the stress distribution was more symmetrical.

In addition to the machining tool paths, the material condition has a significant effect on the overall distortion. It is established in the literature that the near surface machining induced residual stresses have significant effect on the distortion and service life of a part [21]. It is also established that the bulk residual stress (preceding machining) has a significant effect on distortion [8]. The interaction between the bulk residual stress and near surface machining induced residual stress has been explored to some extent in previous work [12]. Bilkhu et al. worked on simulating the coupling effect of bulk and induced residual stresses on machining

distortion [22]. They found that there was initial agreement for modeling based on coupling the bulk and initial residual stresses into a finite element model. However, there is a lack of research investigating the interaction of bulk residual stress and machining induced residual stress in complex geometry.

3.2 Methods

3.2.1 Expanding on the distortion prediction problem

A linearly elastic finite element (FE) model is developed to predict distortion in workpieces with machining induced residual stresses and bulk residual stresses. The model is an expansion on the previous chapter, where elastic stress analysis forms the basis of the prediction. The model will have the same material behavior (assumed to be elastic) and properties as the workpiece. The boundary conditions and workpiece geometry are the same as the previous chapter as well. To determine the robustness of the distortion prediction method proposed in the previous chapter, more complex material preparation and machining is considered in this chapter. The effect of machining is included by applying a through thickness linear bending moment found from residual stress profiles. The effect of different material preparation is included by a bulk residual stress state. The interaction between the bulk residual stress and machining induced residual stress is also included in the model. The through thickness bending moment and the initial bulk residual stress state are then used to provide a solution for equilibrium, which produces an output displacement. The output displacement will be the distortion prediction for the workpieces.

The objective of this chapter is to determine the validity of the distortion prediction method for two cases. The first case is a stress relieved workpiece with complex machining

patterns. The second case is a workpiece with high bulk stress that interacts with the machining stress. First, plate samples of representative material are machined with machining parameters typical of roughing. Residual stress measurements, which include near surface residual stress and bulk residual stress measurements, are performed to determine the initial stress state. As in the prior chapter, samples are machined to assess observed distortion, having thin walls, curves, and straight edges, and are made in two wall thicknesses, 3 mm and 7 mm. The experimental observations are then compared to model outputs to explore validation.

3.2.2 Introducing the model cases

The first case extends the distortion prediction model to feature samples machined with a spiral tool path. The spiral machining pattern is typical in industry to help minimize machining (it is also found to reduce distortion compared to line machining). To assess the spiral path machining, samples were milled from consistently prepared plate samples of AA7050-T7451. This material condition is known to have low levels of bulk residual stress [4] and was chosen so the distortion of the sample would be due to milling induced residual stress (MIRS) rather than the bulk residual stress (BRS). The manufacturing of the sample occurred in the same 5 steps as described in Chapter 2, but the pocket floor finished with a spiral pattern (rather than the line milling). The spiral pattern is machined with the same parameters as the prior chapter (with a cutting speed of 200 m/s, a feed per tooth of 0.2 mm, an axial engagement of 3 mm and a radial engagement of 4 mm). The spiral pattern follows the shape of the pocket walls, starts from the middle of the pocket, and ends along the walls. An example of a finished spiral path sample is shown in Figure 25. The samples for this model will be referred to as low bulk stress (LBS) samples with spiral milling.

The second case examines the distortion prediction for samples with more significant BRS. To introduce high bulk residual stress, blocks were taken from the parent stock (AA7050) and solution heat treated and aged to T74 condition. This heat treatment was completed to industry specifications [23] where the plate is solution heat treated, quenched to room temperature, and then artificially aged in two stages. The blocks were then cut into plate samples of the same dimensions as those used in Chapter 2. Feature samples are then machined into the high bulk stress (HBS) plates with either 7 mm or 3 mm thick walls. The line milling pattern is used to mill the pocket floor and has the same tool parameters as the spiral pattern. These samples will be referred to as HBS samples with line milling.

3.2.3 Residual stress measurements and initial stresses

The distortion prediction method uses residual stress measurements to determine the initial stress state. The initial stress at or adjacent to the machined surface is the near surface MIRS. The near surface MIRS is measured using hole-drilling with depth increments as described in Chapter 2. In addition to hole-drilling, slitting was used in prior work [24] to measure bulk residual stress in both the LBS and HBS plate samples.

An initial stress due to machining is applied to the model using a linear through thickness bending stress. The linear through thickness stress corresponds to a measured MIRS in the previous chapter, and is defined from values of principal force,

$$\bar{M}_2 = \bar{F}_1\left(\frac{t_w}{2} - h\right) \tag{9}$$

$$\bar{M}_1 = \bar{F}_2\left(\frac{t_w}{2} - h\right) \tag{10}$$

where the bending moments along each direction are M_1 and M_2, the thickness of the part is t_w (which is 3 mm or 7 mm), and the force is given by values found from previous work [12]. The distance from the machined surface to the location of the centroid of the effective stress is defined from previous work and is represented by h [12]. How the location of effective stress is determined is shown in Figure 26. The bending moments along with the area moment of inertia and the distance from the centerline, y, are used to find principal bending stresses.

$$\sigma_1 = \frac{\bar{M}_1 y}{I} \tag{11}$$

$$\sigma_2 = \frac{\bar{M}_2 y}{I} \tag{12}$$

These equations were introduced in the previous chapter. The principal stresses are then used to calculate component stresses using Mohr's circle equations where σ_x is the milling direction, σ_y is the transverse direction, and σ_{xy} is the shear.

$$\sigma_x = \frac{\sigma_1 + \sigma_2}{2} + \frac{\sigma_1 - \sigma_2}{2}\cos(2\theta) \tag{13}$$

$$\sigma_y = \frac{\sigma_1 + \sigma_2}{2} + \frac{\sigma_1 - \sigma_2}{2}\cos\left(2(\theta + 90)\right) \tag{14}$$

$$\sigma_{xy} = -\frac{\sigma_1 - \sigma_2}{2}\sin\left(2\theta\right) \tag{15}$$

Where θ is the principal angle relative to the milling direction, a value found from MIRS data and described in previous work [12]. The bending stress model is based on plate bending theory and gives an equivalent linear stress profile through the thickness of the part (as shown in Figure 26). The bending stress model is advantageous because it allows for a simpler mesh, which improves model computation time. The bending stress model is also able to capture the interaction between the BRS and MIRS. The BRS in the material affects the results from the near

surface MIRS. The value of MIRS trends to the value of BRS, which changes the residual stress profile. Examples of this interaction between BRS and MIRS is discussed in previous work [12].

3.2.4 Model specifics – spiral stress and high bulk residual stress application

The finite element model used to predict distortion is similar to the model in the previous chapter. The model material has a Young's Modulus of 72000 MPa and Poisson's ratio of 0.33. An in-plane mesh size of 2 mm is used in the sample, except starting at the pocket floor to the bottom of the model, where a 0.1 mm mesh size is used along the z-direction. The refined mesh is only in the pocket floor area, where the spiral and line milling occurs and was chosen to capture the stresses calculated from the linear through thickness bending stress. The bending stress is applied in the areas where aggressive machining occurs (i.e. the pocket floor). The walls the top face, and the bottom face of the sample are assumed to be free of MIRS, which was shown to be a valid assumption in the previous chapter. Tetrahedral elements are used in areas with more complex geometry, and hexahedral elements in the pocket floor as used in the prior chapter. The boundary conditions are fixed at the center bolt hole of the part, which makes that location a datum for assessment of distortion.

Initial stresses are imposed at the centroids of the elements. BRS is added to the bending stress to account for both bulk and machining residual stress. Because the spiral sample is milled with the same parameters as the line milled sample, the bending stresses are rotated to follow the path of the tool. The tool path is shown in Figure 27 and is used to calculate those angles. Since the machining tool and parameters are the same as the line sample from the previous chapter. The grand average stress for the milling is shown in Figure 28a and is used for both spiral and line milling. The grand average stress from milling is used to formulate the bending stress, and

the bending stress is added to the LBS found from slitting, shown in Figure 28b. The LBS is only considered for the σ_{xx} direction, and all other BRS components are assumed to be zero.

The HBS model must account for MIRS, BRS and the interaction between the two. Machining on HBS plate samples with the same BRS and machining residual stress hole-drilling measurements, and data analysis provided the table of plate bending stress parameters used to determine the bending moment throughout the feature sample model. The data were developed previously [12] and the parameters are given in Table 3. The principal forces (F_1 and F_2), principal angle (θ), and depth of effective stress (h) are plotted versus underlaying BRS in Figure 29. The forces and principal angle show linear trends with BRS. The depth of effective stress is taken as constant with BRS. To determine the underlying BRS in the model, the data from slitting HBS samples in two directions (σ_{xx} and σ_{yy}) is applied biaxially to a FE model of the feature sample. The model is constrained with boundary conditions at the 5 bolt hole locations in the feature sample. The model is allowed to relax, and the resulting residual stresses along σ_{xx} are the underlying bulk residual stresses used to determine the bending moment parameters. The underlying bulk residual stress when all 5 bolt holes are constrained is an estimate of BRS when the sample is clamped to the worktable and the milling is nearly complete. In the pocket floor volume (the areas where aggressive machining occurs) the clamped BRS at each element is used to determine the bending stress parameter values the linear trends in Figure 29. The resulting bending stresses are then added to the BRS from slitting, which is then applied to all elements in the model. The model is then allowed to come to equilibrium, the clamping is released at all locations except the center bolt hole, which provides the estimated distortion.

3.2.5 Model validation

The validation of the distortion prediction method is accomplished with three types of experimental methods: (1) comparison of the observed and predicted form of the bottom face; (2) comparison of the observed and predicted residual stress at particular locations on the pocket floor; (3) comparison of the observed and predicted form of the bottom face after the pocket floor is removed from the sample.

The first validation compares the observed and predicted form of the bottom face of the feature samples. This comparison was first introduced in the methods discussed in the previous chapter and is done qualitatively by color maps of the overall surface form, and quantitatively by line plots along a series of lines across the surface. The surface form is measured on the physically machined samples using a TalyScan 250 laser scanning profilometer (Talyor Hobson). The profilometer measures surface height (z) at a grid of points with 0.2 mm spacing along both the x and y directions and extraneous data points are trimmed. The line plots are taken along the bottom face at values of constant x (25, 100, and 175 mm) and y (15, 50, and 85 mm) as well as diagonally (positive and negative diagonals from corner to corner of the surface form). In the model prediction, an uncertainty determination from the model results is used. The uncertainty is derived from the residual stress measurement uncertainty bars, which represent the standard deviation of stress at each depth. This standard deviation of stress is applied as an input to the model and the resulting surface form is used for the uncertainty bands for the surface form produced by the model results. The observed and predicted data are fitted to a plane and the plane is subtracted from that data to present a consistent frame of comparison. The datum is established in the same way as discussed in the previous chapter.

The second method involves comparing residual stress profiles measured experimentally from hole-drilling. To measure residual stress profiles in the spiral stress sample, gages are rotated and placed to align with the tool path. The rotation of the gages allows a comparison of the spiral stresses to the grand average stress which is applied (after rotation) to the spiral stress feature sample model. Figure 30 shows the location of the hole drilling measurements for the spiral stress feature sample. Measurements are made in the 7 mm spiral milled feature sample. The locations are noted with the location and the angle at which the gage is rotated (i.e. Right-90: the gage is located to the right and rotated 90 degrees). To measure residual stress profiles in the HBS sample, gages are placed in locations of various BRS. Measuring MIRS in areas of compressive and tensile BRS allows comparison to stress profiles found previously in HBS plate samples [12]. To determine the bulk residual stress in the sample, a simulation is run with the underlying bulk residual stress, and the resulting clamped bulk residual stress is analyzed. Figure 31 shows BRS in the 7 mm feature sample as introduced (based on slitting measurements), as in the clamped condition, and as in the released condition. These data were used to determine the locations of the hole drilling measurements, which are shown in Figure 32.

The third method of validation isolates the pocket floor from the feature samples by cutting. This isolates the surface where line and spiral path milling occurred in feature samples. The pocket floors are cut free using wire electric discharge machining (EDM) and the observed form of the bottom face is measured using the laser scanning profilometer. The observed form is then compared to the distortion predicted by a model of the isolated pocket floor. The observed and predicted distortion are compared using color maps and also using line plots of the surface form along positive and negative diagonals.

3.3 Results

3.3.1 Validation – form of the bottom surface, spiral path feature sample

Figure 33 shows the observed and predicted distortion for the 7 mm and 3 mm spiral milled feature samples. Figure 33a shows observed form of the bottom face of the 7 mm feature sample, showing a saddle shape, which agrees with the predicted form (Figure 33c) overall, but the predicted magnitude is lower than that observed. Also, the predicted distortion is less rotated than the observed form. The observed form has a maximum height of 0.02 mm and a minimum height of -0.015 mm, while the predicted form has a maximum height of 0.01 mm and a minimum height of -0.01 mm. Figure 33b and Figure 33d show the observed and predicted distortion for the 3 mm feature sample with spiral milling. The observed and predicted form are roughly symmetrical and are similar in form and amount of distortion. The observed form has a maximum height of 0 mm and a minimum height of -0.06 mm, while the predicted form has a maximum height of 0 mm and a minimum height of -0.05 mm. The color scale used for the 3 mm sample extends 3.75x the minimum direction the color scale used for the 7 mm sample.

Line plots of the bottom face form for the 7 mm spiral sample are shown in Figure 34. The observed data is not as smooth as the predicted data, especially along the positive and negative diagonal. The lines taken at x = 100 mm and y = 50 mm go through the center bolt hole of the part (the datum). In general, the distortion for the 7 mm spiral sample is small, within -0.01 mm and 0.02 mm. There is agreement between the shapes of distortion for the line plots, especially at the lines taken at y = 15 mm, y = 50 mm, and y = 85 mm. However, all of the line plots show areas where the observed form falls outside the model uncertainty (i.e. the lines taken along the positive and negative diagonals).

Figure 35 shows line plots of the surface form for the 3 mm spiral milled feature sample. The line taken at x = 100 mm has relatively small height, with lower height for the predicted than the observed. There is good shape agreement between the observed and predicted data on the lines taken at y = 15 mm, y = 85 mm, and the positive and negative diagonal. The observed height consistently falls within or just outside prediction bounds along these lines. The lines taken at x = 25 mm, x = 175 mm, and y = 50 mm demonstrate general shape agreement between the observed and predicted form, but there are variances in the observed data that do not appear in the predicted data.

3.3.2 Validation – form of the bottom face, HBS feature sample

Figure 36 shows the observed and predicted forms for the 7 mm and 3 mm high bulk residual stress feature samples with line milling. Figure 36a and Figure 36c show the observed and predicted distortion along the bottom of the 7 mm sample. The predicted form shows a bowl shape with a slight rotation from the centerline of the sample. The observed form shows a similar form but is more linear than circular. The observed form rotates away from the centerline of the sample, but the rotation is less than that in the predicted form. The observed and predicted forms have a maximum height of 0.5 mm and a minimum height of 0 mm. The Figure 36b and Figure 36d show the observed and predicted forms along the bottom of the 3 mm sample. The distortion is similar in shape and magnitude (maximum of 0.5 mm and minimum of 0 mm) to the 7 mm sample, but there is more rotation in both the observed and predicted form. The predicted form also has more of a bowl shape and has a greater rotation from the centerline than the observed distortion for the 3 mm samples. The distortion in the high stress samples is significantly less flat than the form in the spiral low bulk stress samples, with the color scale 25x (7 mm spiral sample) and 10x (3 mm spiral sample) that of the spiral sample color scales.

Figure 37 shows the line plots for the 7 mm high bulk residual stress feature sample. The lines taken along x = 25 mm, x = 100 mm, and x = 175 mm show very little height variaton, with the line taken at x = 100 mm showing the least agreement between the observed and predicted results, and the observed height 0.01 mm lower than the predicted height at the ends of the line plot. The best agreement is seen along the positive and negative diagonals and the lines taken at y = 50 mm with the observed results trending well with the predicted results.

Figure 38 shows the line plots for the 3 mm high bulk residual stress feature sample. Similar to the 7 mm sample, the lines taken along x = 25 mm, x = 100 mm, and x = 175 mm are relatively flat. The observed height is approximately 0.1 mm larger than the predicted height for the lines taken along x = 25 mm and x = 175 mm. The line taken along x = 100 mm has the best magnitude agreement between the observed and predicted height, but it also the line taken where there is very little height in the sample. There is general shape agreement between the observed and predicted height for the lines taken along y = 15 mm, y = 50 mm, and y = 85 mm, along with the positive and negative diagonal lines, but the observed height is consistently larger than the predicted height.

3.3.3 Validation – residual stress measurements

Figure 39 shows the residual stress profile results from the pocket of the 7 mm spiral milled feature sample. The results are compared to the grand average stress profile. In general, the results agree well with each other and with the grand average stress profile. In the milling direction, the stress profiles measured on the feature sample peak higher (-170 MPa to -215 MPa) than the grand average stress profile (-145 MPa), but the peak stress occurs at the same depth (0.05 mm) for all measurements. The stresses trend toward zero at a depth of 0.2 mm, except T-0 and R-90, which trend toward zero at a depth of 0.15 mm. In the transverse

direction, at all locations stress peaks at a depth of 0.05 mm and a magnitude of -150 MPa for the grand average, approximately -185 MPa for T-0, R-90, and B-180, and -125 MPa for L-270. The transverse stresses trend to zero at a depth of 0.2 mm. The shear stress peaks at a value of -120 MPa for L-270, -75 MPa for T-0 and R-90, and -60 MPa for B-180.

Figure 40 compares the MIRS measured in the 7 mm pocket of the high bulk stress feature sample (D11) to the MIRS in a high bulk stress plate sample (D3) in an area where the bulk residual stress is tensile. In the milling direction, stress peaks at a depth of 0.05 mm, where D3-X4Y2 and D11-middle peak at -135 MPa, and D3-X3Y2 and D11-left peak at -100 MPa. The stresses trend toward a tensile bulk residual stress value at a depth of 0.24 mm. The bulk stress values are approximately -80 MPa for D11-middle, and 100 MPa for the other 3 measurements. In the transverse direction, at all locations stress peaks around -120 MPa at a depth of 0.05 mm for the plate sample measurements, and -170 MPa and -140 MPa at a depth of 0.04 mm and 0.05 mm for D11-middle and D11-left respectively. All values trend toward 0 after 0.24 mm of depth. The shear stress peaks at a depth of 0.05 mm for the feature sample and 0.03 mm for the plate sample at a value of -80 MPa and -60 MPa respectively. The plate sample results and the feature sample results trend toward zero after a depth of 0.15 mm. There are distinct differences in MIRS in the HBS feature sample when compared to the grand average stress profiles from LBS samples. Since the BRS is largest in the milling direction, the best depiction of the interaction stresses is shown in Figure 40a. These results show where the stresses transition from the MIRS to the BRS (from about 0.15 to 0.23 mm of depth).

Figure 41 shows MIRS in the pocket of the HBS 7 mm feature sample (Top Left in Figure 32) compared to the MIRS in a plate sample in an area of compressive bulk residual stress each. Both results have similar MIRS peak stresses in the transverse and milling directions, but

the BRS at these locations of the plate and feature samples differ somewhat (data at 0.3 to 0.5 mm). The feature sample stress profiles are also noisier than the plate samples with very little agreement between results in the shear direction.

3.3.4 Validation – isolated pocket floor form

Figure 42 shows the observed and predicted form of the bottom face after the pocket floor removal for the 7 mm and 3 mm LBS spiral milled samples. Note that the color scale for the 3 mm data is 5x that for the 7 mm data. The observed and predicted shapes are similar for the 7 mm data, with differences due to a machining line that is visible in the observed results at y = 35 mm. The observed and predicted shapes are nearly identical for the 3 mm data; with similar magnitude and shape. The 3 mm observed data also has a machining line at y = 35 mm, which could account for the difference when compared to the predicted results.

Figure 43 shows diagonal line plots of the observed and predicted form of the 7 mm and 3 mm spiral milled bottom face of the isolated pocket floor. There is very good shape agreement for both the 7 mm and 3 mm line plots. The 7 mm line plots have a bump from the machining line which alters the shape. The magnitude of both the observed and predicted line plots are nearly identical, and the curvature of the lines are very consistent with each other.

Figure 44 shows the observed and predicted form of the bottom face of the isolate pocket floor for the 7 mm and 3 mm HBS samples. Note that the color scale for the 3 mm data is 5x that for the 7 mm sample. The observed and predicted shapes are not very similar for the 7 mm data. The observed and predicted shapes are generally similar for the 3 mm sample. The magnitude of distortion is greater but similar for the predicted form than the observed form, and the rotation from the centerline greater for the predicted form when compared to the observed form.

Figure 45 shows the diagonal line plots of the observed and predicted form for the 7 mm and 3 mm bottom face after the pocket floor removal for the high bulk stress samples. There is very little agreement for the 7 mm line plots. There is general shape agreement for the 3 mm line plots. The 3 mm negative line plot shows near zero height, with a flat parallel curvature. The 3 mm positive line plot shows parabolic trend, with the prediction (maximum height of 0.24 mm) having more distortion than the observation (maximum height of 0.14 mm).

3.4 Discussion

3.4.1 Model and machined feature sample comparison – spiral path feature sample

The previous chapter explored the three validation techniques and their ability to assess the distortion prediction method compared to the observed results. This chapter adds complexity to the distortion prediction by altering the machining tool path and changing the material condition of the sample. The spiral machining pattern was chosen because it is desirable in industry to minimize distortion. For the spiral path machined feature sample, the distortion decreases to approximately a third to what was seen in the low stress line milled samples in the previous chapter (3 mm and 7 mm, Figure 12). Since the distortion is so small, any unintended variations in machining parameters could cause larger differences between the observed and predicted data. This could also contribute to the better agreement between the observed and predicted data for the bottom face of the 3 mm sample, which has about twice the form of the bottom face of the 7 mm sample.

The residual stress measurements in the pocket of the spiral feature sample agree well with the grand average stress profile that is applied in the model and is obtained from line milling. The consistency supports the approach of using residual stress measured on the simple

plate sample to predict the distortion of parts with more complex geometries and more complex milling.

The pocket floor removal of the spiral machining path samples isolates the spiral stress application and analyzes the distortion prediction. The removed pocket floor distorts more than the surface form of the bottom of the feature samples for the spiral path machining. Since the distortion is driven by the machining, and since the isolated pocket floor models show good agreement, the discrepancy from the spiral machining path feature sample is most likely from another source.

3.4.2 Model and machined feature sample comparison – HBS feature sample

There is good agreement between the observed and predicted surface form for the 7 mm and 3 mm high bulk stress feature samples. The bending moment model accounts for the interaction of bulk residual stress and machining induced residual stress. The model can account for the interaction by utilizing data from previous work and calculating the bending stress parameters from measured residual stress profiles [12]. The agreement between observed and predicted results supports this method for the 7 mm sample. The general agreement between the observed and predicted results also supports this method for the 3 mm sample, but with more discrepancy. Since the bending stress model depends on MIRS measured in HBS plate samples, hole drilling measurements were completed in the 7 mm HBS sample. The measured stress in the 7 mm feature sample compared well to that of the plate samples, further supporting the method.

Hole drilling measurements were also completed in the 3 mm high stress feature sample. Measurements were completed in areas of tensile bulk residual stress and the locations are shown in Figure 46. Figure 47 compares the residual stress profiles in an area of tensile bulk residual

stress for the 7 mm feature sample (D11) and for the 3 mm feature sample (G13). The data from the 3 mm sample peak at a lower value than the 7 mm sample. In the length direction, σ_{xx} peaks at a value of -65 MPa for the 3 mm sample, and -100 MPa or -130 MPa for the 7 mm sample, but at a consistent depth of 0.05 mm for all measurements. In the transverse direction, σ_{yy} peaks at a value of -70 MPa for the 3 mm sample, which is approximately half of the peak from the 7 mm sample measurements. The stress for the 3 mm sample is also around half (-45 MPa) of the peak of the 7 mm sample in the shear direction. These results suggest that the bending moment model may not be as accurate for the 3 mm sample. Future research is needed to determine the cause of this discrepancy. The hole-drilling results also support that the model may not be as accurate for the 3 mm sample, which was seen in the surface forms of the bottom face of the feature sample and the isolated pocket floor where the observed and predicted forms did not agree as closely as for the low stress samples.

3.5 Conclusion

This study assessed the distortion prediction method on two complex cases. One case assessed the model for a spiral milling path. The other case assessed the model for a high bulk residual stress material. Validation of the cases was performed with three methods, one which analyzed the observed and predicted form of the bottom face of the feature sample, another which compared the measured residual stress profiles in the feature sample to those assumed in the model, and finally the pocket floor was isolated and removed and the observed and predicted form of the bottom face was compared.

For the spiral milled samples, the bottom face distortion shows that the thickness of the feature sample influences the accuracy of the distortion prediction method, with the 3 mm

feature sample prediction agreeing better with the observed results. Overall, there is general agreement between the predicted and observed results. The bottom face distortion also demonstrates that the spiral milling significantly decreases the overall distortion compared to a workpiece milled with line milling. The residual stress measurements completed in the floor of the spiral sample are very similar to the residual stress profiles used in the distortion model. Where the stress directions follow the milling path. This agreement supports the residual stress profiles being applied for the distortion prediction method. There is agreement in both the magnitude and form of the 7 mm and 3 mm pocket floors isolated from LBS spiral milled feature samples. Since there is good agreement in both magnitude and form for the isolated pocket floor models, the discrepancy from the feature sample must be from another source. Further research is required to determine this discrepancy.

For the high bulk stress samples, the bottom face distortion shows that the high bulk residual stress significantly influences the distortion of the sample. The distortion increases compared to the LBS samples in both the 3 mm and 7 mm samples, with the 3 mm sample showing more rotation in the angle of maximum curvature. There is less agreement in the 3 mm predicted and observed results than the 7 mm predicted and observed results. The residual stress profiles show that the 3 mm feature sample has less near surface residual stress than the 7 mm sample, which could account for this. The 7 mm near surface residual stress measurements agree well with the measurements that were completed on the high stress plate samples, supporting the distortion prediction in this thickness. The isolated pocket floor forms do not agree well in either the 7 mm of 3 mm thickness, although the observed form for the 3 mm thickness does have the general shape of the predicted form. The 3 mm isolated pocket floor form is most likely affected by the difference in near surface residual stress profiles, where the 3 mm measured residual

stress profiles in the pocket of the feature sample seem to have shallower MIRS compared to the 7 mm residual stress profiles. Additional pocket floor removals for the 7 mm thickness would be beneficial to determine the cause of this difference since the residual stress profiles and surface form results supported the distortion prediction method in this thickness.

3.6 Tables

Table 3 – Summary of strength of material data taken from previous work that are used to calculate the through thickness bending moment values [12]

Sample ID	σ_b (MPa)	F_{ij} (N)	h_{ij} (mm)	θ (degrees)
A20 Low Bulk Stress	σ_{xx} = -9.5 σ_{yy} = -9.7 σ_{xy} = -4.9	F_{xx} = -8.2 F_{yy} = -11.9 F_{xy} = -3.2	h_{xx} = 0.081 h_{yy} = 0.089 h_{xy} = 0.064	60
B4 Low Bulk Stress	σ_{xx} = -11.8 σ_{yy} = -7.9 σ_{xy} = -5.0	F_{xx} = -10.3 F_{yy} = -12.4 F_{xy} = -3.4	h_{xx} = 0.061 h_{yy} = 0.066 h_{xy} = 0.047	54
A18 Low Bulk Stress	σ_{xx} = -10.8 σ_{yy} = -1.9 σ_{xy} = -6.0	F_{xx} = -11.7 F_{yy} = -11.4 F_{xy} = -4.4	h_{xx} = 0.068 h_{yy} = 0.073 h_{xy} = 0.077	44
D3 – 1 High Bulk Stress	σ_{xx} = -6.9 σ_{yy} = 1.6 σ_{xy} = -2.1	F_{xx} = -12.7 F_{yy} = -18.1 F_{xy} = -4.0	h_{xx} = 0.079 h_{yy} = 0.075 h_{xy} = 0.069	62
D3 – 2 High Bulk Stress	σ_{xx} = -112.6 σ_{yy} = -18.8 σ_{xy} = 4.5	F_{xx} = 4.2 F_{yy} = -27.2 F_{xy} = -2.2	h_{xx} = 0.081 h_{yy} = 0.080 h_{xy} = 0.036	85
D3 – 3 High Bulk Stress	σ_{xx} = 92.9 σ_{yy} = 0.4 σ_{xy} = -4.1	F_{xx} = -23.6 F_{yy} = -13.8 F_{xy} = -6.0	h_{xx} = 0.070 h_{yy} = 0.077 h_{xy} = 0.060	25

3.7 Figures

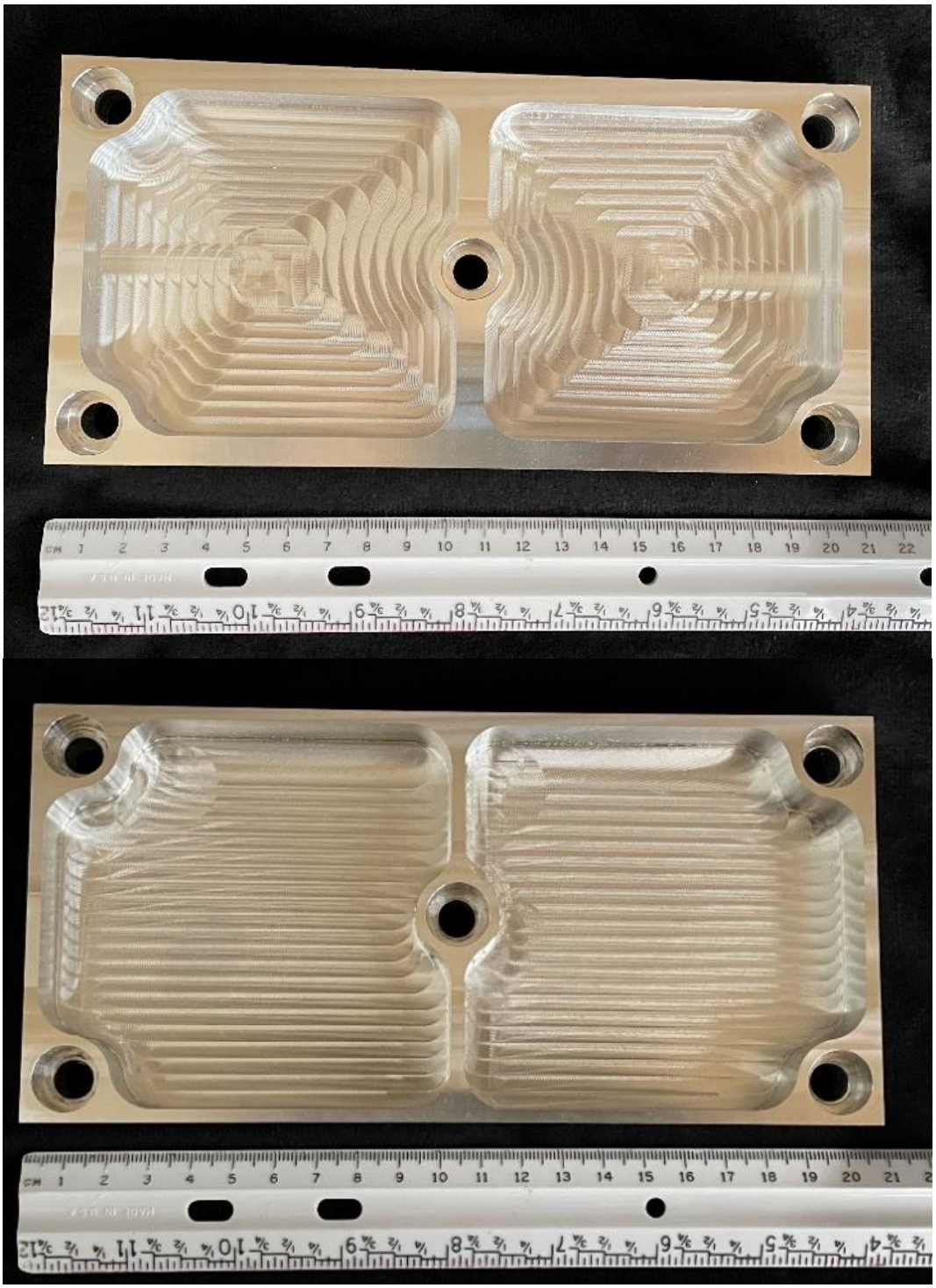

Figure 25 – Spiral milling in a 7 mm stress relieved feature sample (top) and line milling in a high bulk stress 3 mm feature sample (bottom)

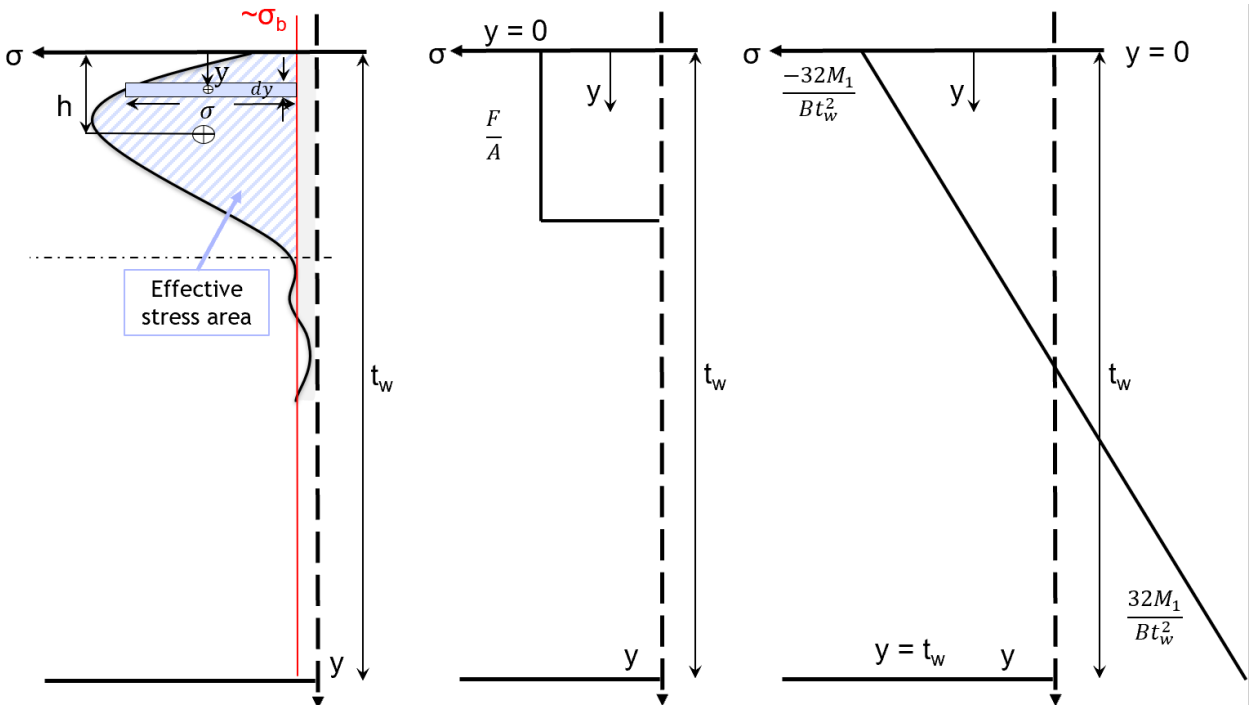

Figure 26 – Diagrams depicting the strength of materials elastic stress analysis (left), the average axial stress (middle) and the bending moment stress (right)

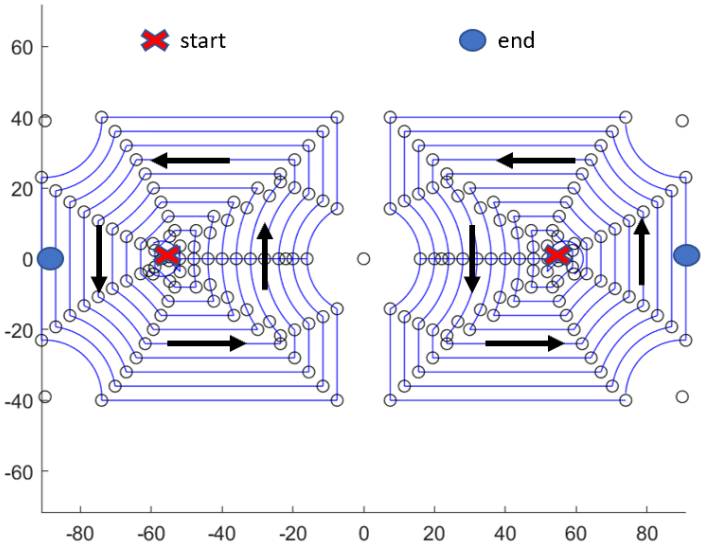

Figure 27 - Spiral path milling from the machining g-code to determine rotation of stresses in application to the spiral path milling model

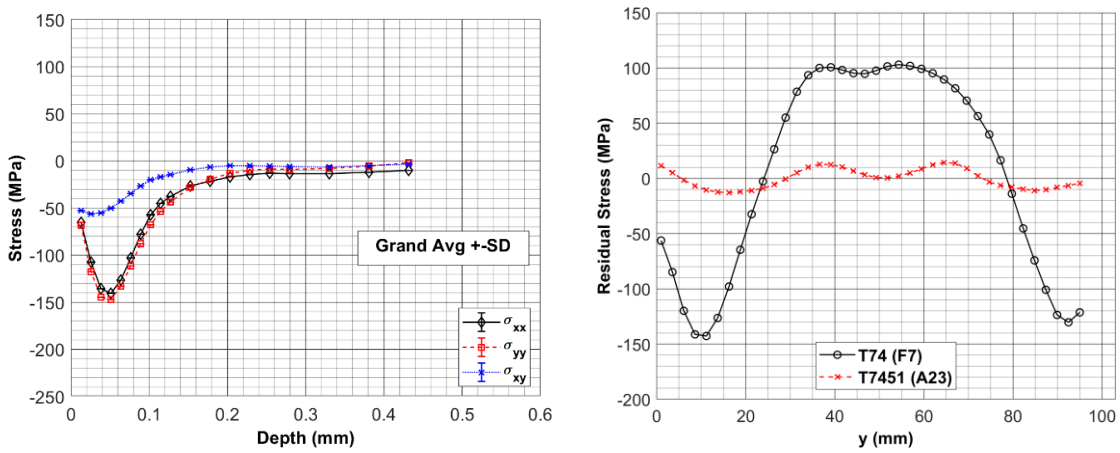

(a) (b)

Figure 28 - Grand average residual stress profiles applied to the spiral path milling model (a). Bulk residual stress measured from slitting for HBS (T74) and LBS (T7451) plate samples at the mid length (x = 100 mm) (b)

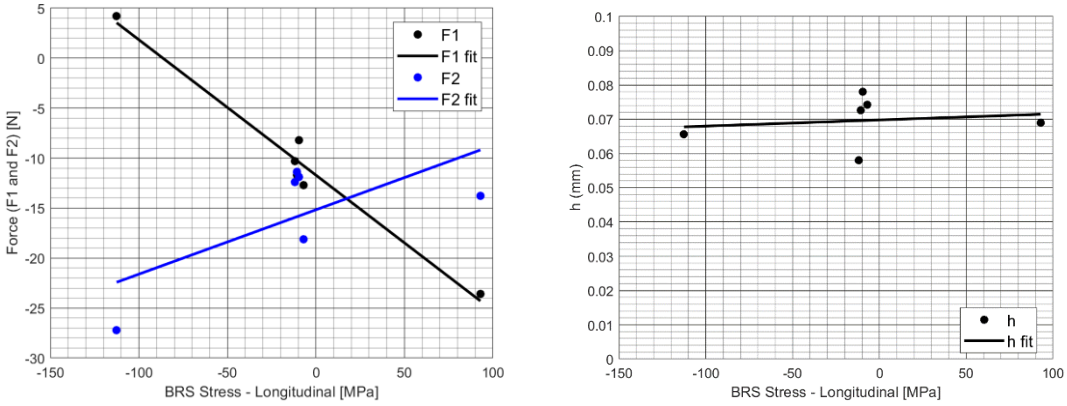

(a) (b)

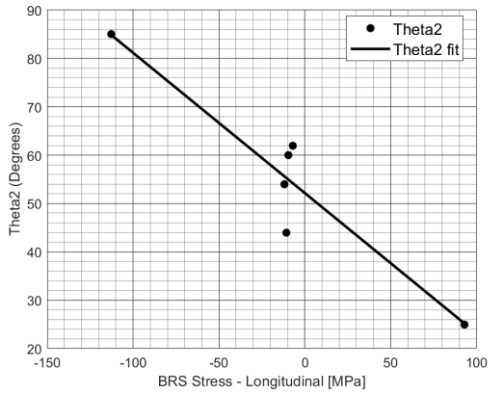

(c)

Figure 29 – (a) principal Forces (F1 and F2), (b) effective stress depth (h), and (c) principal angle (theta 2) model parameters as functions of bulk residual stress. Fitted lines are taken through the data to interpolate the parameters as functions of bulk residual stress

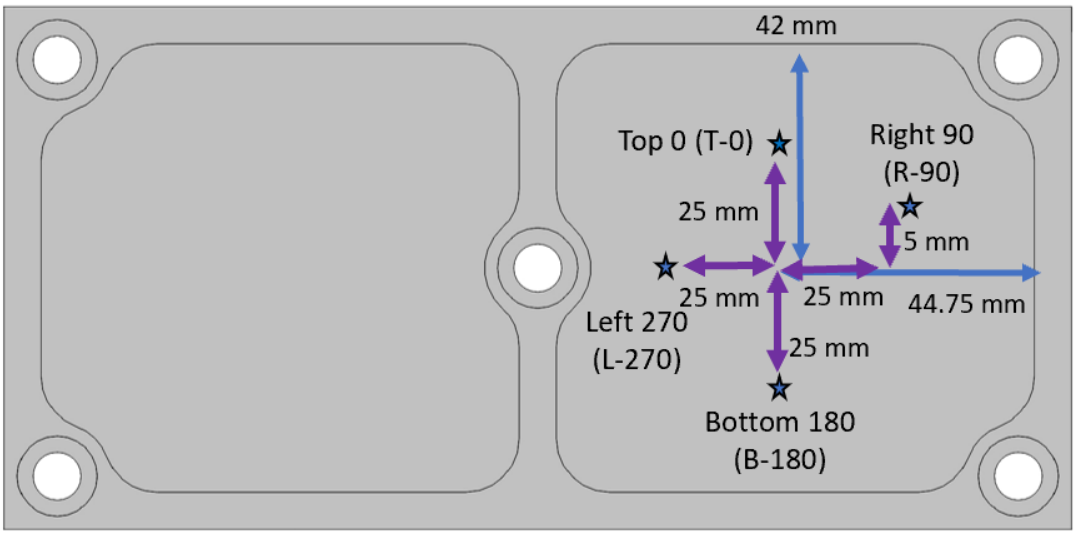

Figure 30 - Location of hole drilling measurements on the pocket floor of the 7 mm spiral path feature sample

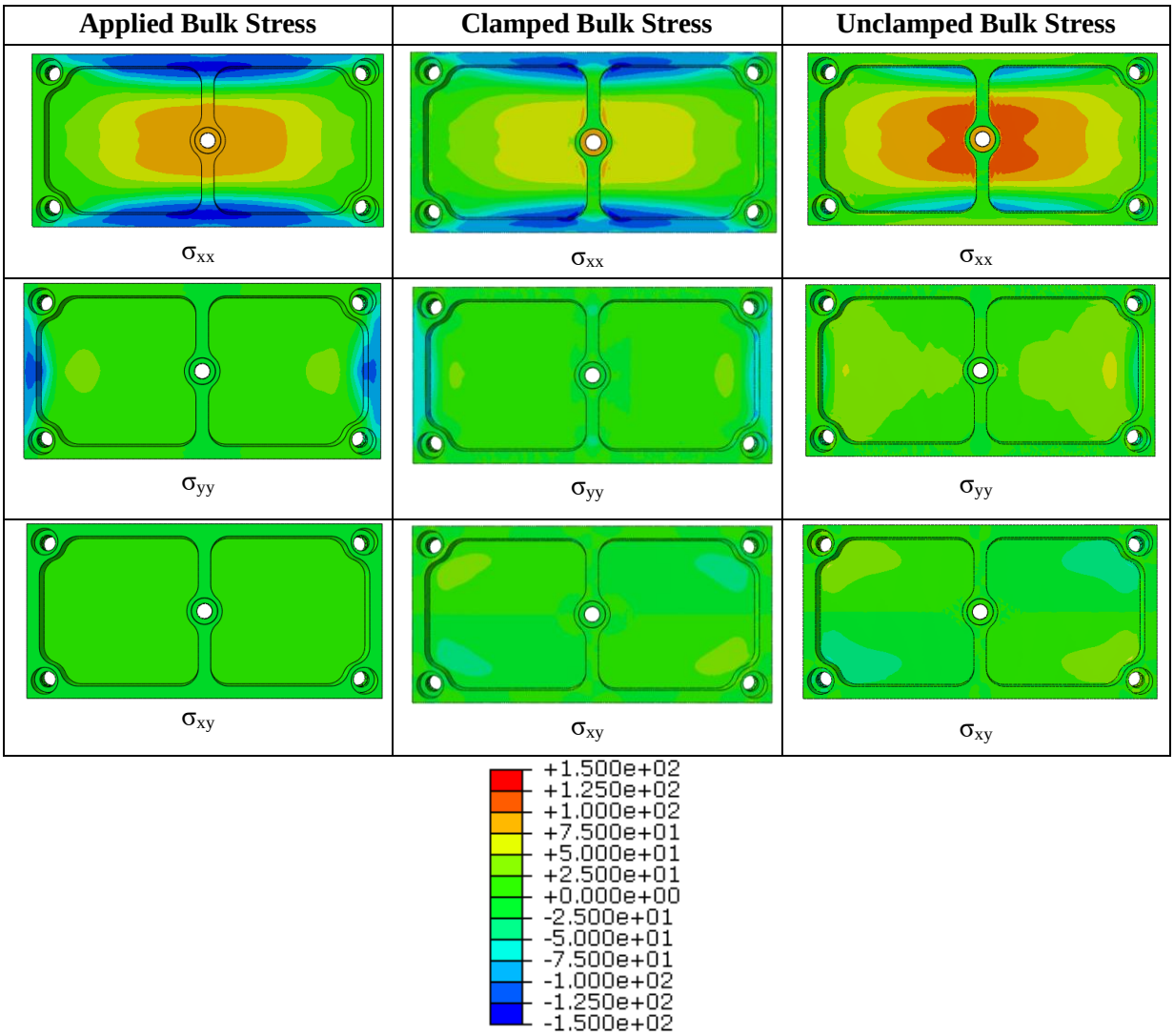

Figure 31 - Feature sample high bulk stress stress maps. Top: stress along σ_{xx}, middle: stress along σ_{yy}, bottom: shear stress. Left: bulk stress found from CMOD slitting; Middle: bulk stress when all bolt holes are clamped; bulk stress when all bolt holes are released. All color maps have the same scale

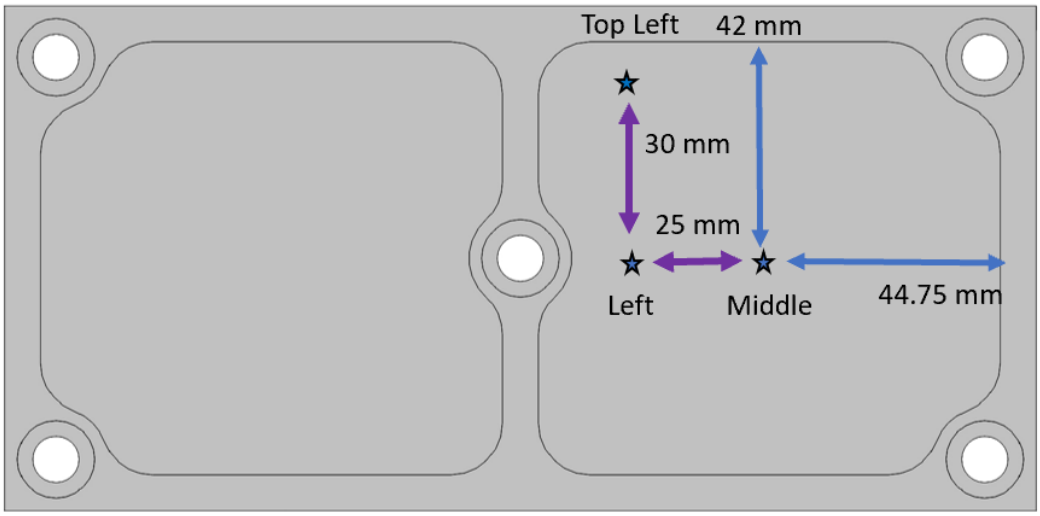

Figure 32 - Location of hole drilling measurements on the pocket floor of the 7 mm high bulk stress feature sample

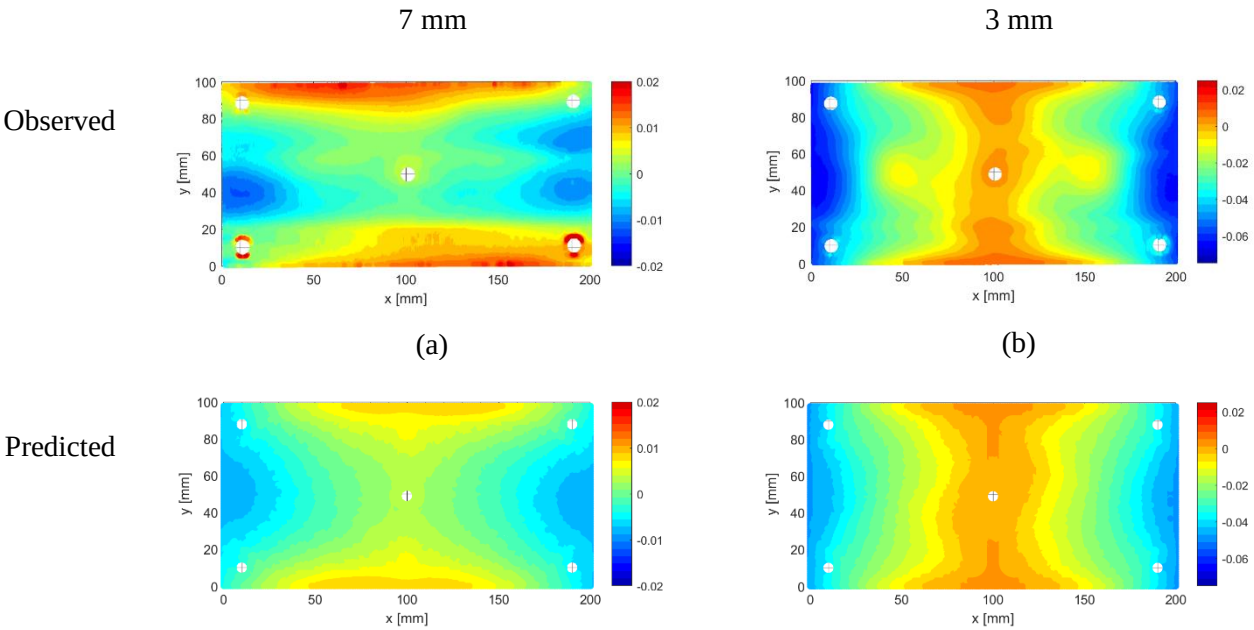

Figure 33 – Observed (upper) and predicted (lower) form of the bottom face of the 7 mm (left) and 3 mm (right) feature samples milled with spiral path milling

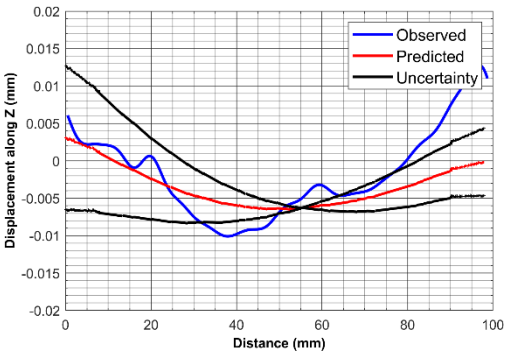

(a) x = 25 mm

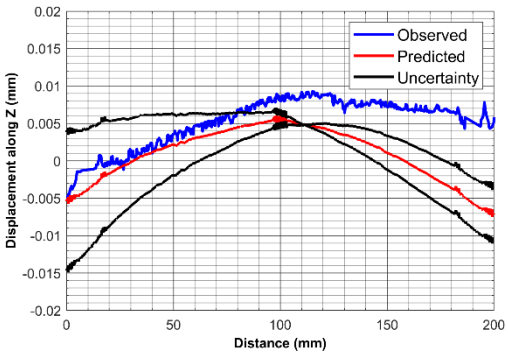

(b) y = 15 mm

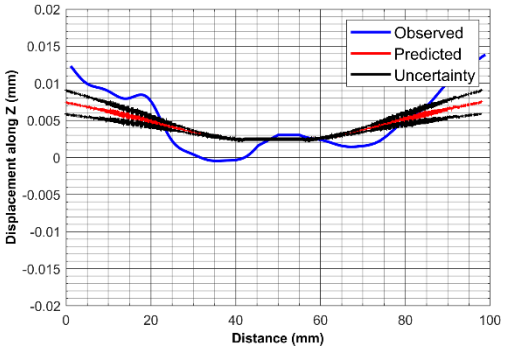

(c) x = 100 mm

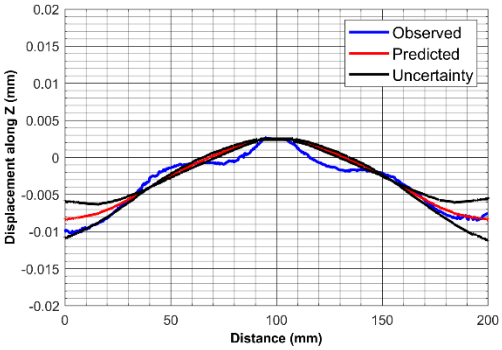

(d) y = 50 mm

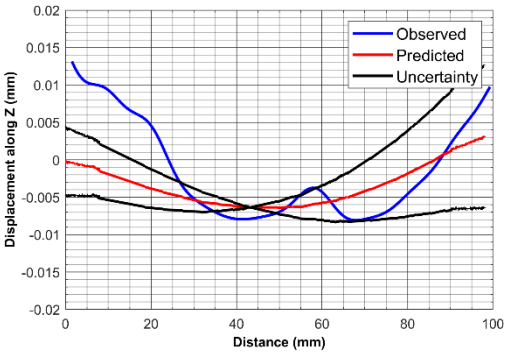

(e) x = 175 mm

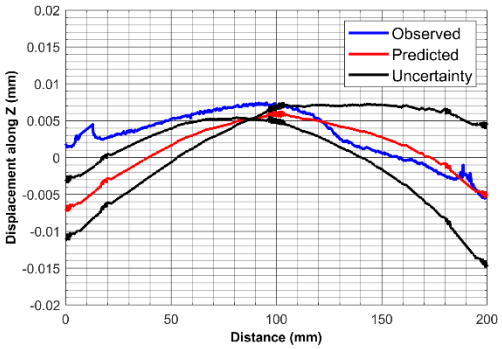

(f) y = 85 mm

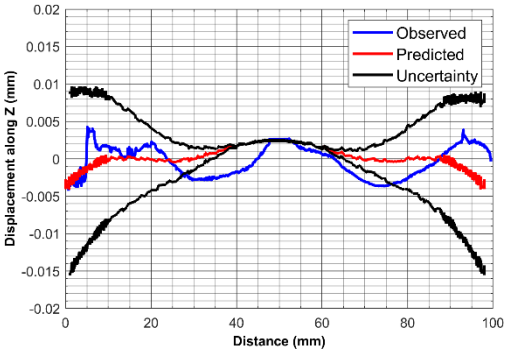

(g) Positive diagonal

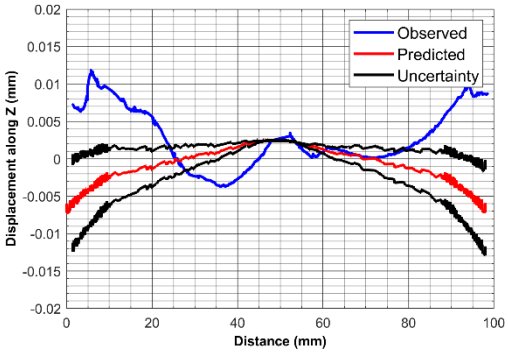

(h) Negative diagonal

Figure 34 – LBS, 7 mm, spiral path milling: line plots of bottom surface form along various paths

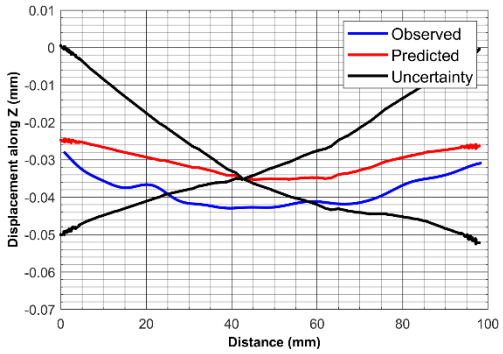

(a) x = 25 mm

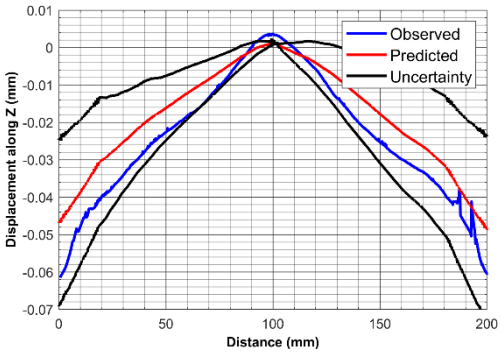

(b) y = 15 mm

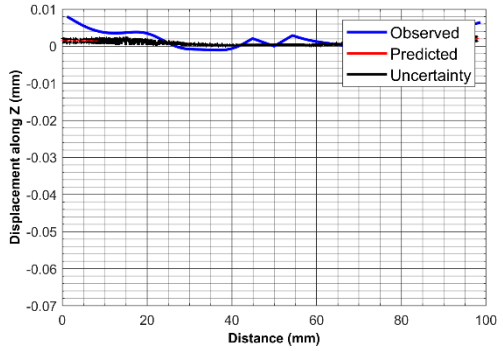

(c) x = 100 mm

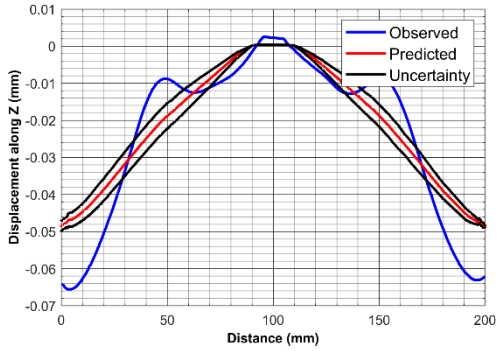

(d) y = 50 mm

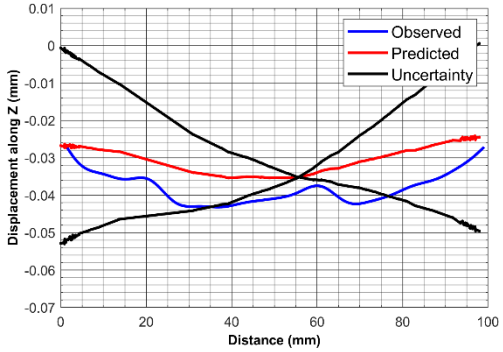

(e) x = 175 mm

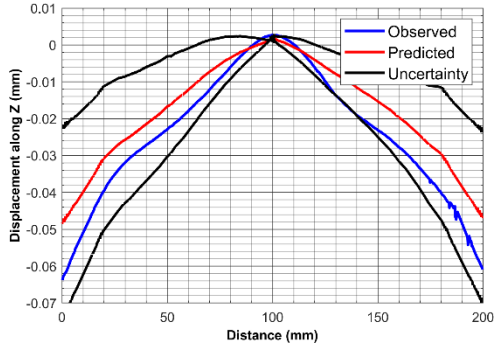

(f) y = 85 mm

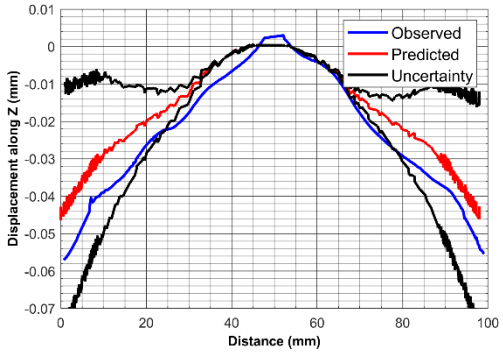

(g) Positive diagonal

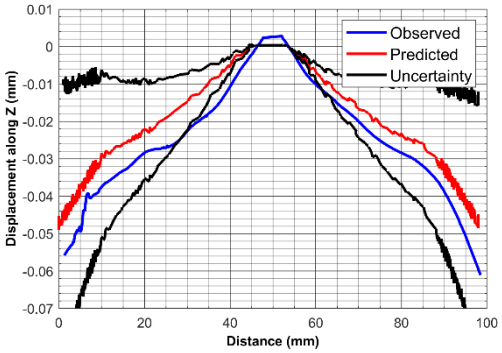

(h) Negative diagonal

Figure 35 – LBS, 3 mm, spiral path milling: line plots of bottom surface form along various paths

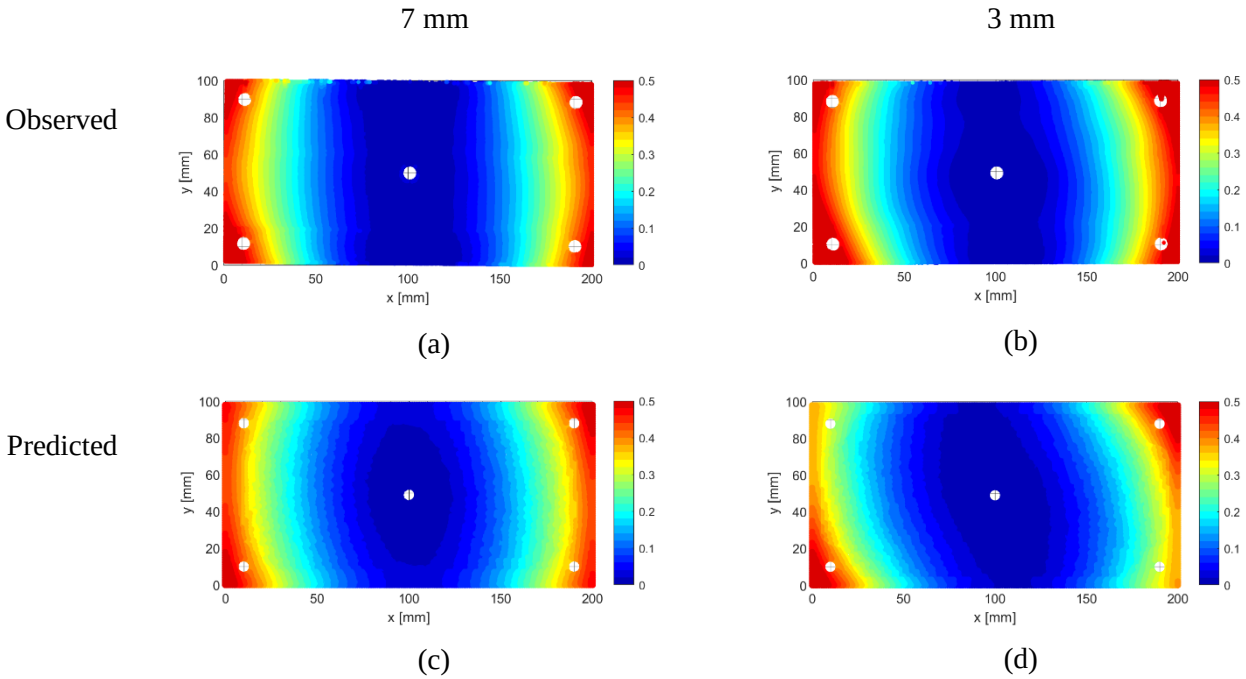

Figure 36 – Observed (upper) and predicted (lower) form of the bottom face of the 7 mm (left) and 3 mm (right) feature samples with high bulk residual stress and line path milling

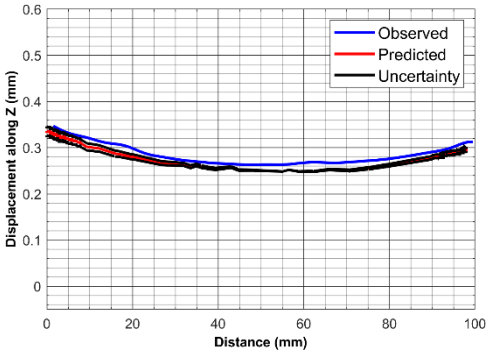

(a) x = 25 mm

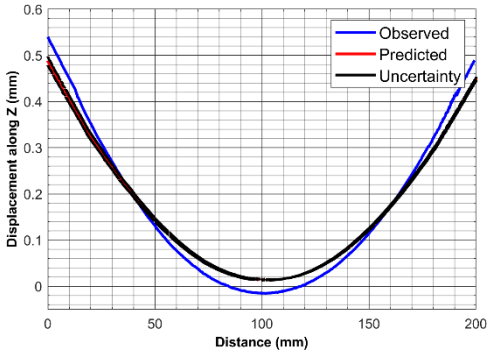

(b) y = 15 mm

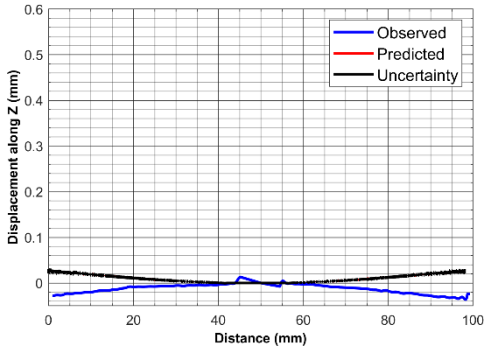

(c) x = 100 mm

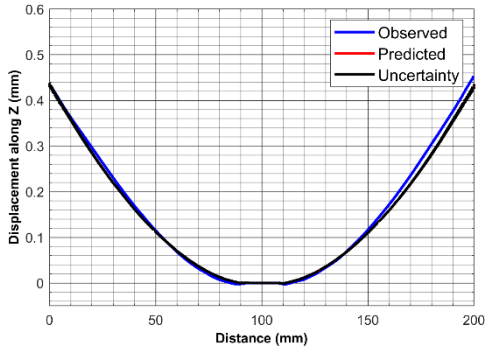

(d) y = 50 mm

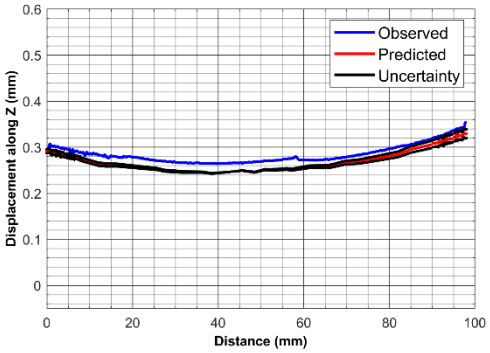

(e) x = 175 mm

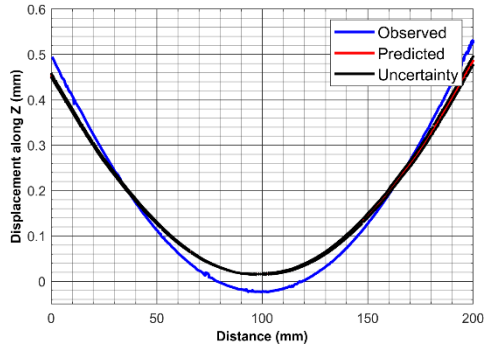

(f) y = 85 mm

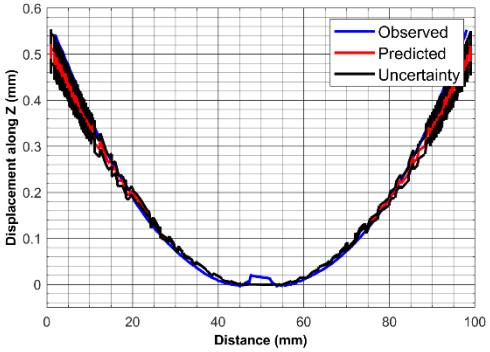

(g) Positive diagonal

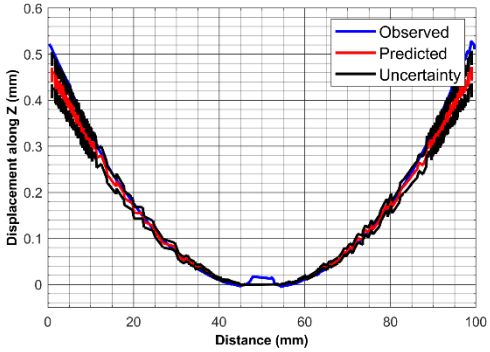

(h) Negative diagonal

Figure 37 – HBS, 7 mm, line path milling: line plots of bottom surface form along various paths

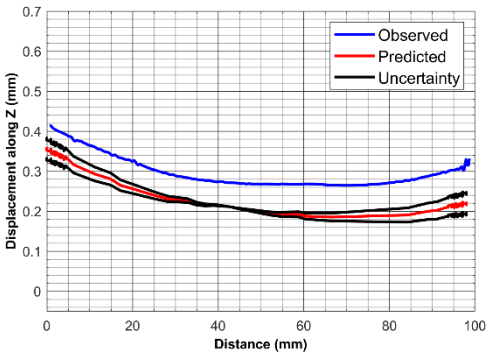

(a) x = 25 mm

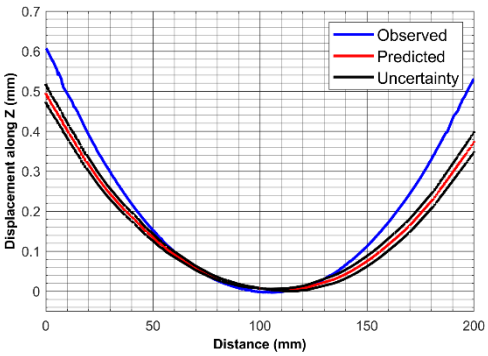

(b) y = 15 mm

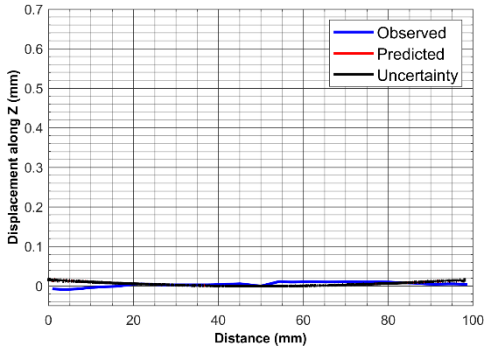

(c) x = 100 mm

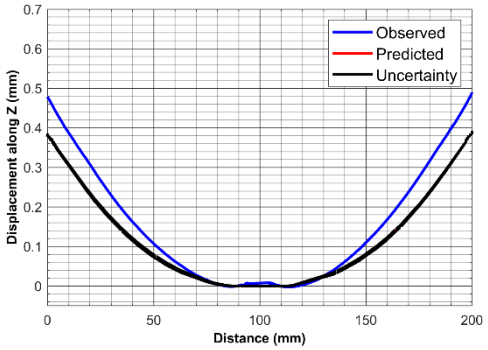

(d) y = 50 mm

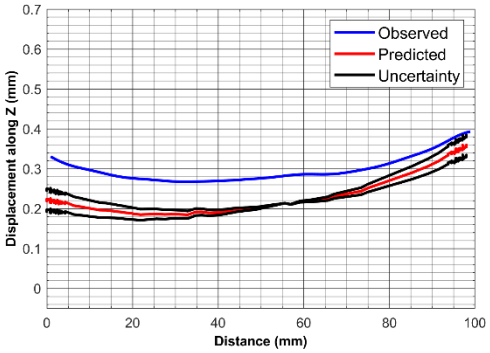

(e) x = 175 mm

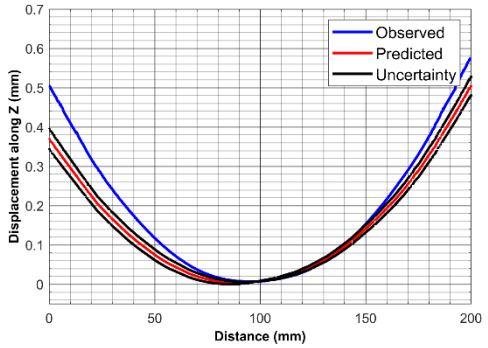

(f) y = 85 mm

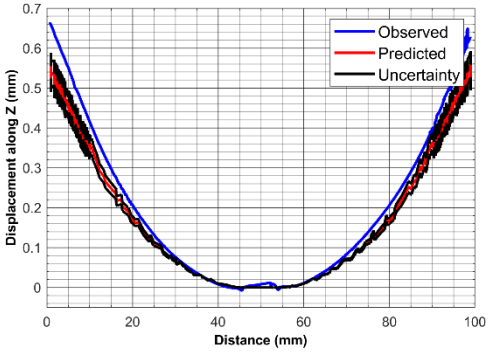

(g) Positive diagonal

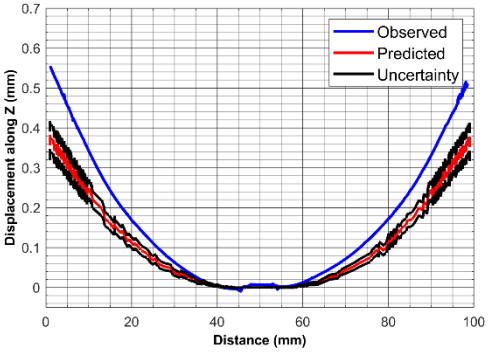

(h) Negative diagonal

Figure 38 – HBS, 3 mm, line path milling: line plots of bottom surface form along various paths

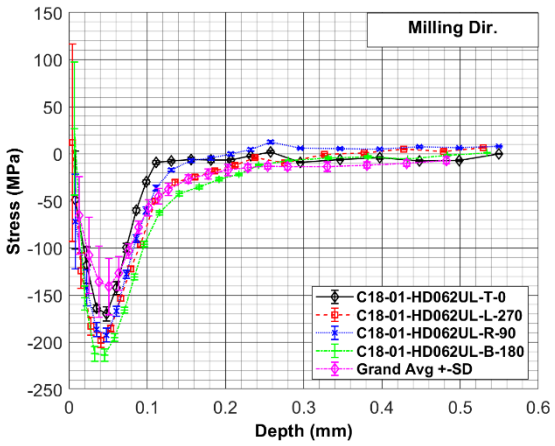

(a)

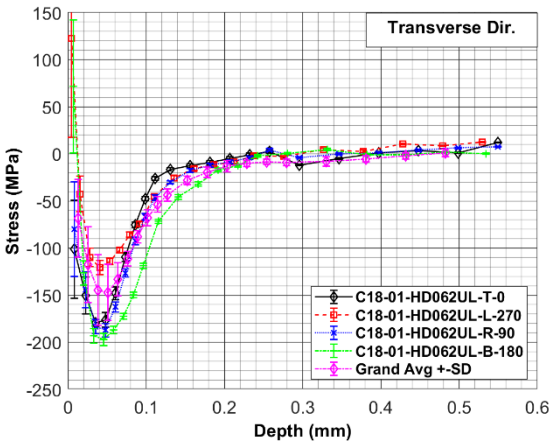

(b)

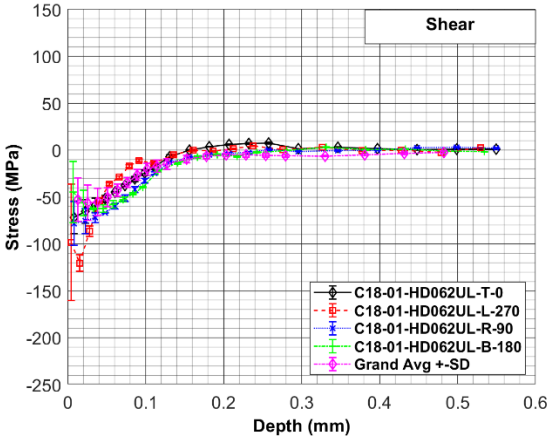

(c)

Figure 39 - Residual stress profile results from the pocket of the spiral path feature sample (C18) compared to the grand average mode 3 stress profile: a) milling direction b) transverse direction c) shear stress

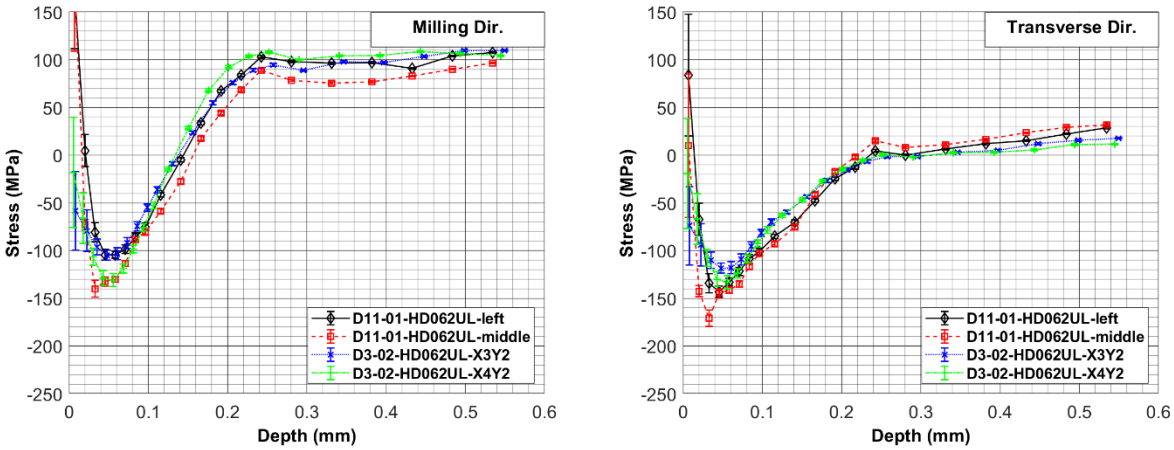

(a)

(b)

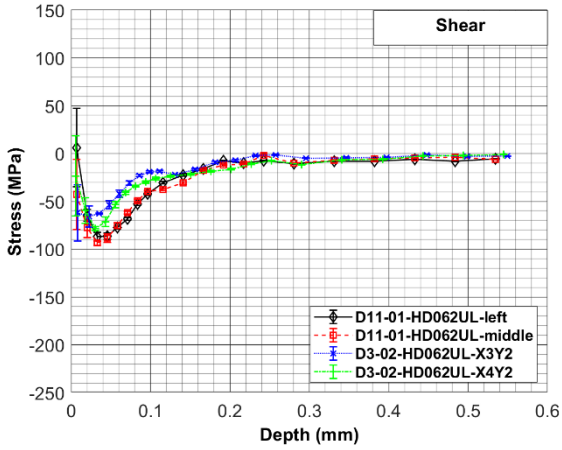

(c)

Figure 40 - Residual stress profile results from the pocket of the high bulk stress 7 mm feature sample (D11) in an area of tensile bulk residual stress compared to residual stress profile results from a plate sample (D3) in an area of tensile bulk residual stress: a) milling direction b) transverse direction c) shear stress

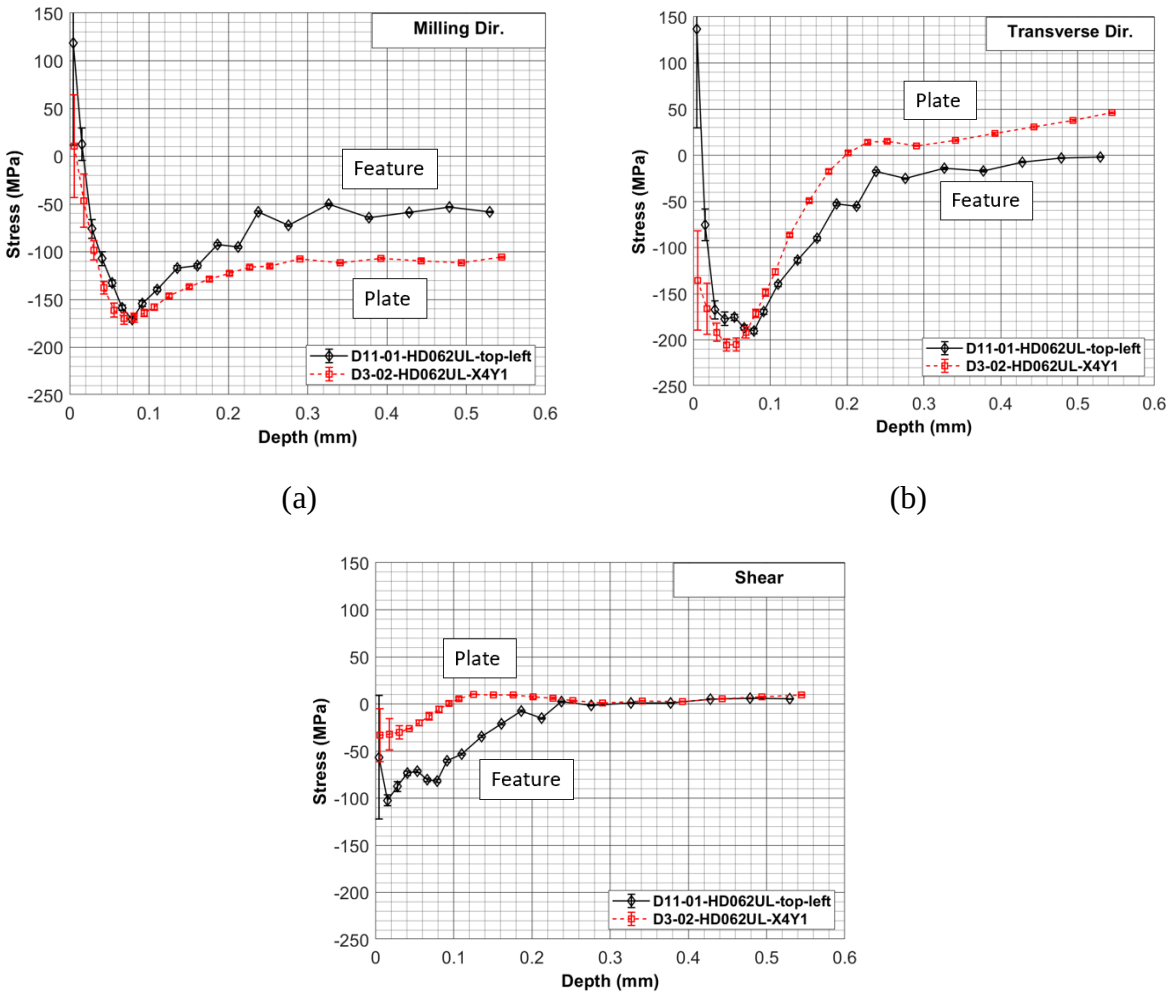

Figure 41 - Residual stress profile results from the pocket of the high bulk stress 7 mm feature sample (D11) in an area of compressive bulk residual stress compared to residual stress profile results from a plate sample (D3) in an area of compressive bulk residual stress: a) milling direction b) transverse direction c) shear stress

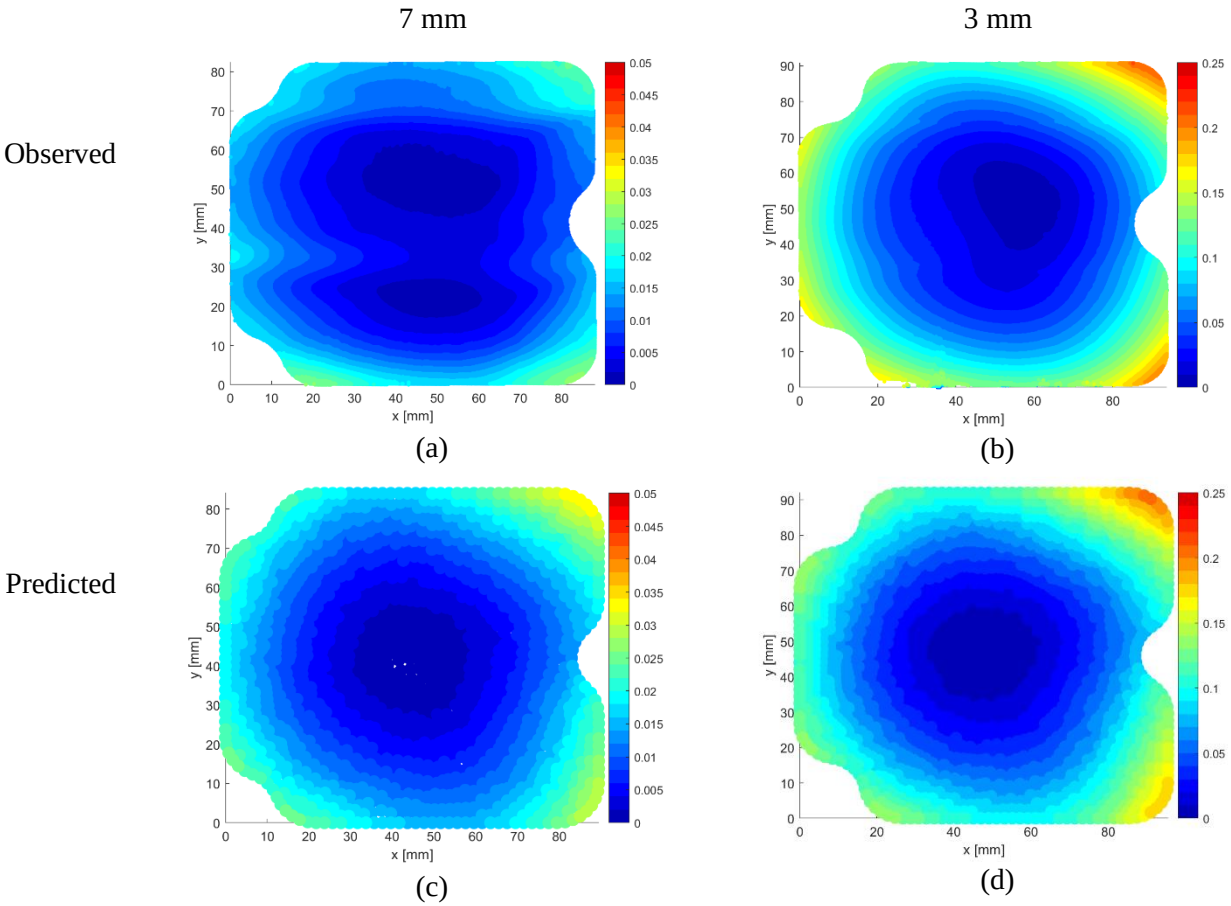

Figure 42 – LBS spiral milled form of the bottom face of the isolated pocket floor from the 7 mm (left) and 3 mm (right) spiral milled feature sample. Observed results (top) and predicted model results (bottom)

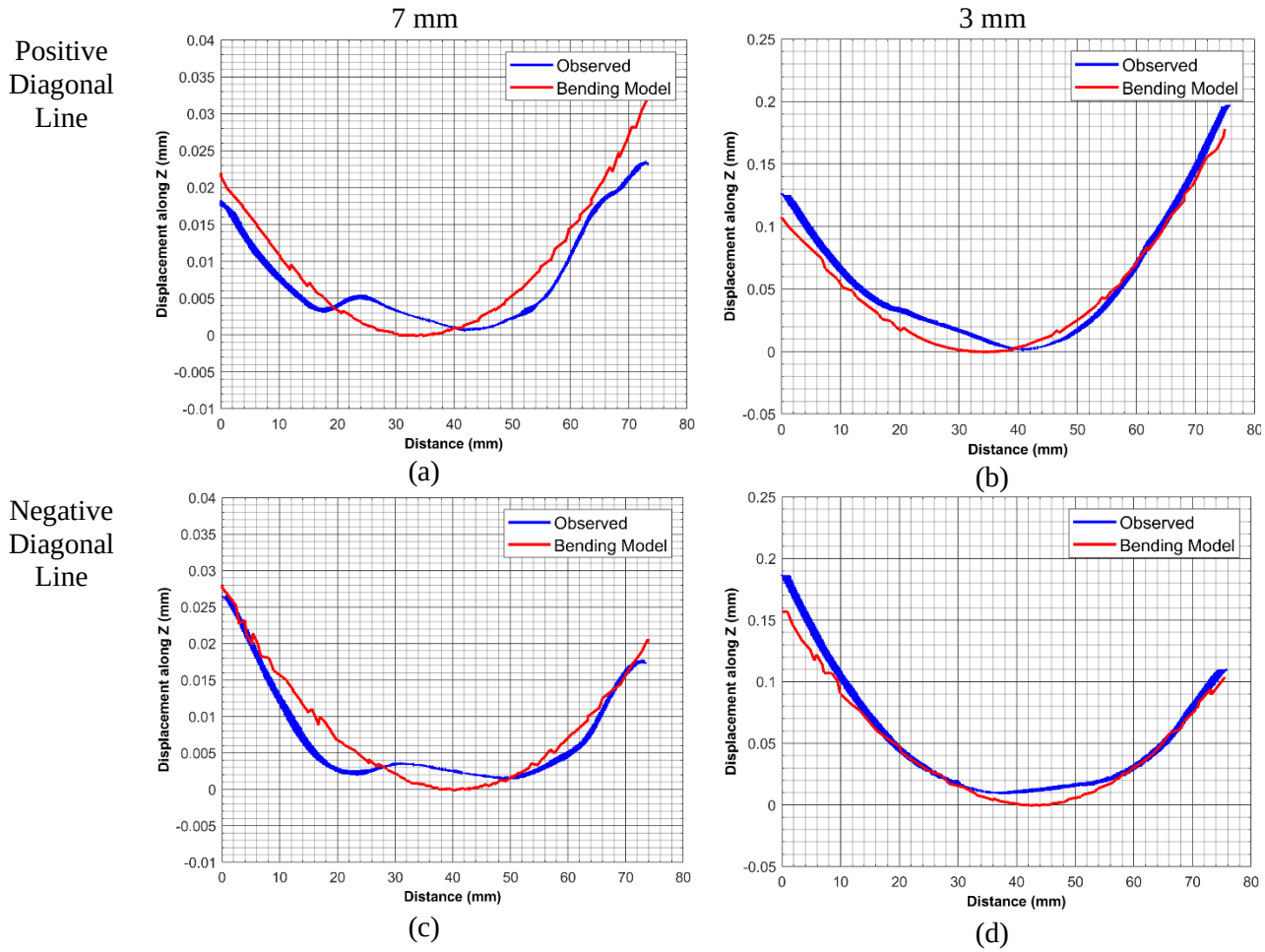

Figure 43 – Diagonal line plots of observed and predicted bottom surface form after the pocket floor removal for the spiral path milled 3 mm and 7 mm samples

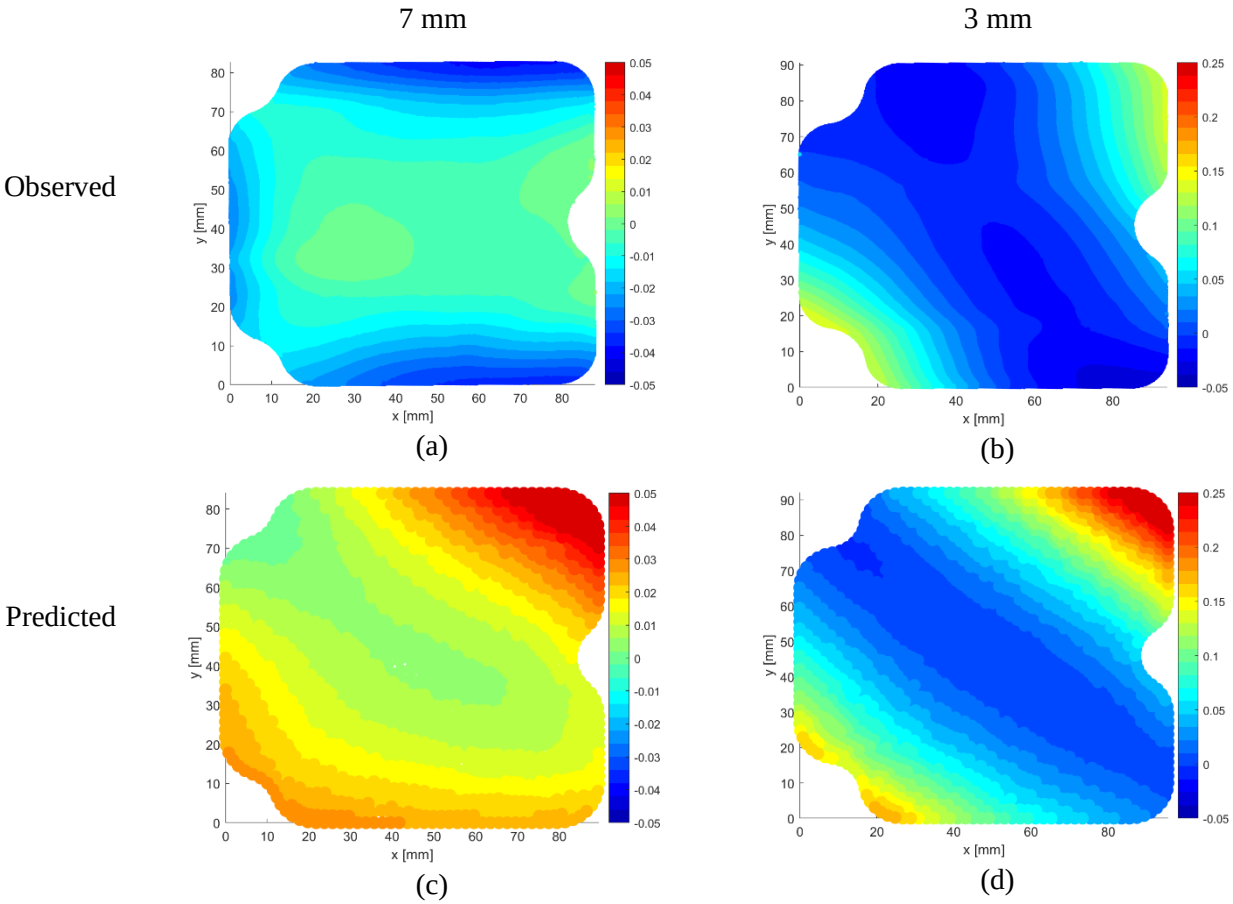

Figure 44 – HBS line milled form of the bottom face of the isolated pocket floor from the 7 mm (left) and 3 mm (right) high stress feature sample. Observed results (top) and predicted model results (bottom)

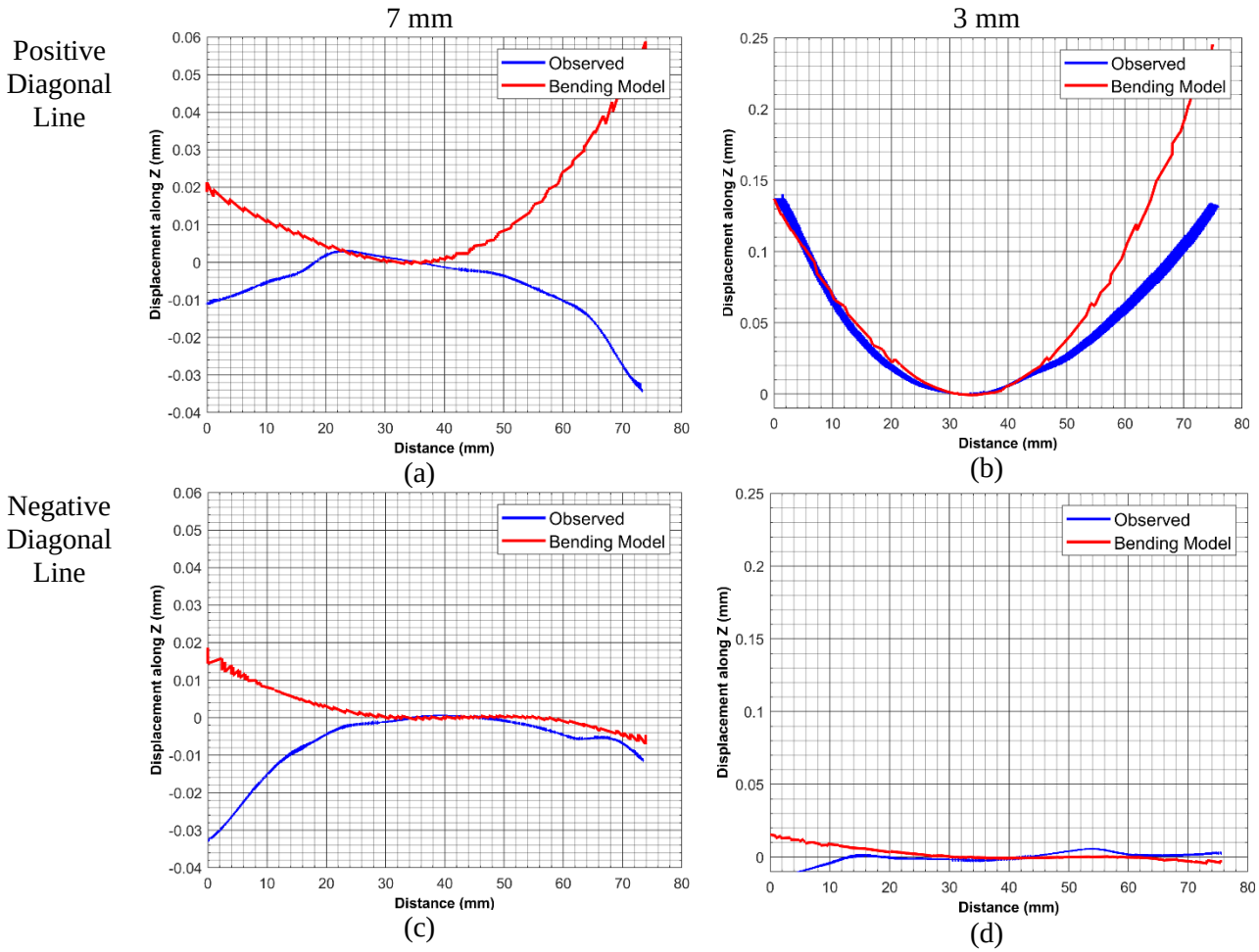

Figure 45 – Diagonal line plots of observed and predicted bottom surface form after the pocket floor removal for the 3 mm and 7 mm high stress samples

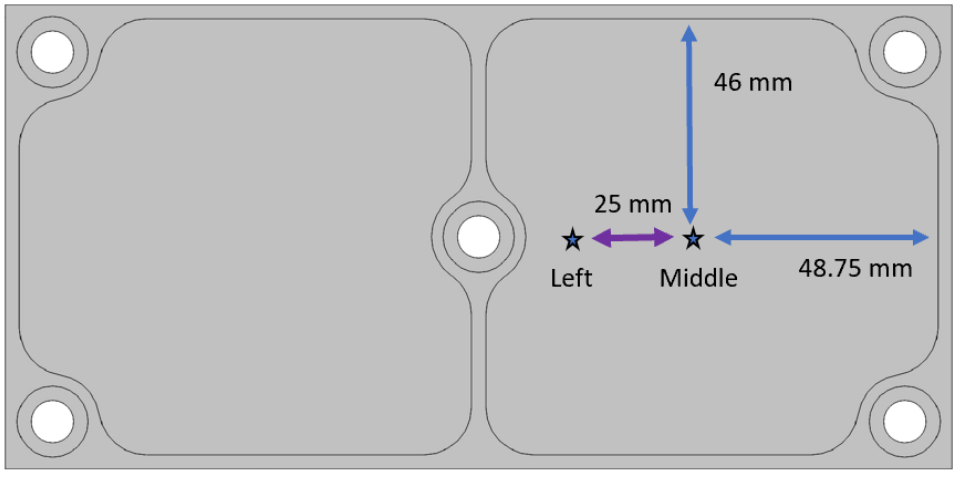

Figure 46 - Location of the hole drilling measurement on the pocket of the 3 mm high stress feature sample

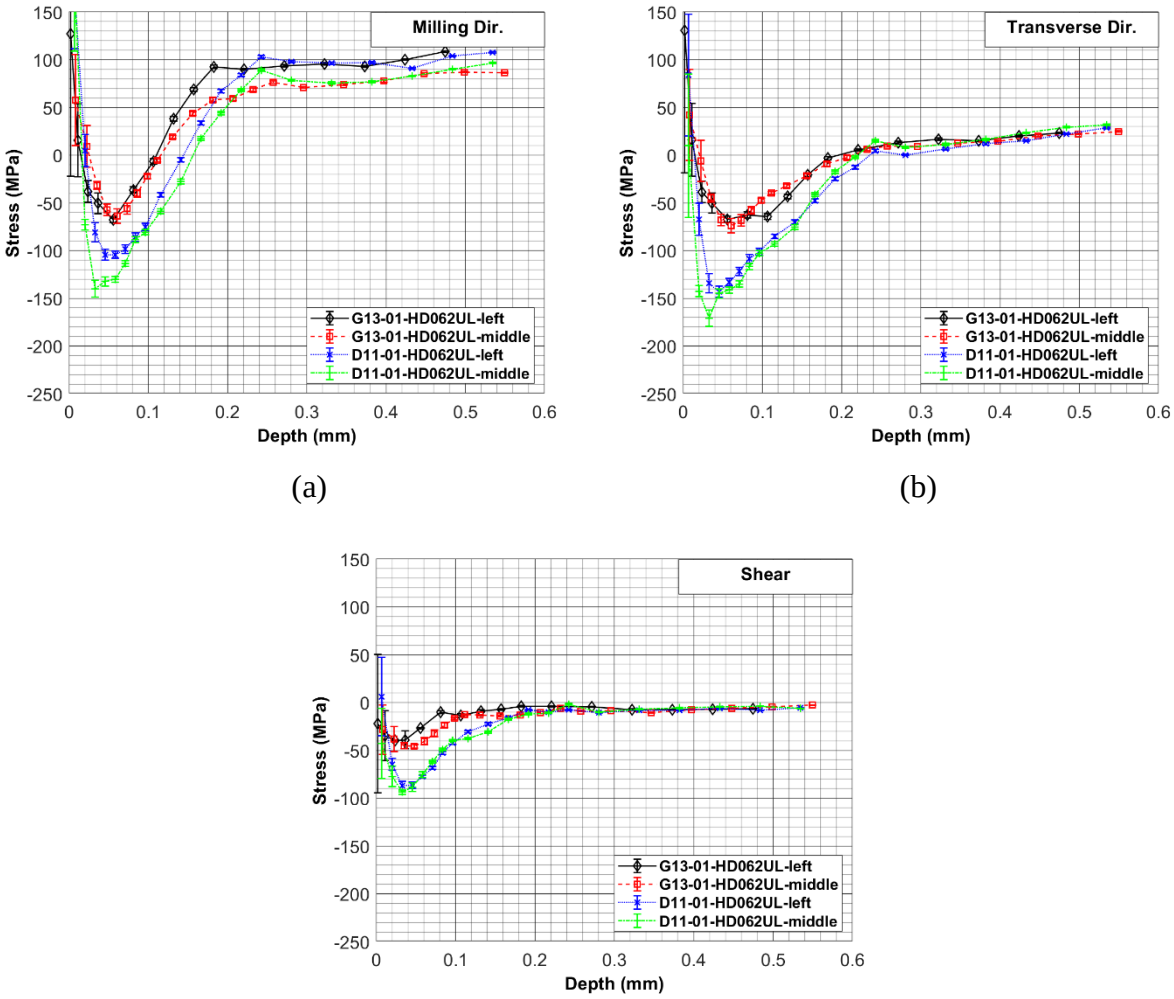

Figure 47 - Residual stress profile results from the pocket of the high bulk stress 7 mm feature sample (D11) in an area of tensile bulk residual stress compared to residual stress profile results from the high bulk stress 3 mm feature sample (G13) in an area of tensile bulk residual stress: a) milling direction b) transverse direction c) shear stress

Chapter 4 – Conclusions and Future Work

Chapter 1 introduces the purpose of this research and the implications to the manufacturing industry. Chapters 2 and 3 analyze the distortion prediction method for workpieces with complex geometries and verify the method using validation experiments. The development and implementation of the model is introduced for a thin-walled lightweight aerospace component. A finite element model is developed based off the geometry and material properties of the component. Residual stress measurements are then completed on representative material with simple geometries and used as input to the finite element model. Near surface residual stress measurements were completed using the hole-drilling technique and bulk residual stress measurements were completed using the slitting technique.

Chapter 2 introduces the validation experiments that were used to analyze the distortion prediction. Evaluating both the surface form of the sample and the residual stresses gives a comprehensive understanding of the influence that residual stress has on the overall distortion of the workpiece. Additional research could analyze the surface forms on the other sides of the feature sample, and work towards a 3-dimensional mapping of distortion, which was out of scope for this work. Chapter 2 also focuses on the aggressive milling which is the main cause of near surface residual stress in the samples. Future work could also analyze other types of machining and their influence on distortion. In general, the distortion prediction method introduced in Chapter 2 is a useful method.

Chapter 3 explores the method introduced in the previous chapter with the added complexity of spiral path machining and high bulk residual stress in the samples. The validation experiments demonstrate that the method gives a consistent prediction of distortion for the spiral path samples. The isolated pocket floors show improved agreement between observed and

predicted results, suggesting that the modeling method may be affected by other influences, and further research is needed to determine the cause of these discrepancies. The validation experiments also demonstrate there is a general agreement for the bottom face surface forms for the prediction of distortion for the high bulk stress samples. The residual stress measurements competed on the samples with 7 mm wall thickness show agreement with the residual stress measurements completed on the representative plate samples. The residual stress measurements in the 3 mm wall thickness show less agreement. The interaction of bulk residual stress and milling induced residual stress could contribute to the difference in the residual stress profiles in samples with very thin walls, which can be explored in future work. Additional research is needed to refine the method in the high bulk stress material.

In general, the distortion prediction model presents a useful method for prediction and control and can help minimize part rejection and rework in the aerospace industry. There is good shape agreement between the predicted models and the observed results, which supports the method in this thesis. Additional work may be needed for more complex cases and future research and refinement can help improve the method.

References

[1] Sim, W. (2010) Challenges of residual stress and part distortion in the civil airframe industry. International Journal of Microstructure and Materials Properties. 5(4-5):446-455. https://doi.org/10.1504/IJMMP.2010.037621

[2] Li, J., Shu-qi, W. (2016) Distortion caused by residual stresses in machining aeronautical aluminum alloy parts: recent advances. Int J Adv Manuf Tech. 89:997-1012. https://doi.org/10.1007/s00170-016-9066-6

[3] Masoudi, S., Saeid A., Ehsan S., Hamdollah E. (2015) Effect of machining-induced residual stress on the distortion of thin-walled parts. Int J Adv Manuf Tech. 76(1):597-608. https://doi.org/10.1007/s00170-014-6281-x

[4] Prime, Michael B. (2001) Cross-sectional mapping of residual stresses by measuring the surface contour after cut. Journal of Engineering Materials and Technology 123(2): 162-168. https://doi.org/10.1115/1.1345526

[5] Madariaga, A., Perez, I., Arrazola, P.J., Sanchez, R., Ruiz, J.J., Rubio, F.J. (2018) Reduction of Distortions in Large Aluminum Parts by Controlling Machining-Induced Residual Stresses. Int J Adv Manuf Tech. 97:967-978. https://doi.org/10.1007/s00170-018-1965-2

[6] Schindler, S., Zimmermann, M., Aurich, J.C., Steinmann, P. (2013) Modeling deformations of the workpiece and removal of material when turning. CIRP Conference on Modeling of Machining Operations. 8:39-44. https://doi.org/10.1016/j.procir.2013.06.062

[7] Ma, Y., Zhang, Z., Yu, D., Feng, P., Xu, C. (2019) Modeling of machining distortion for thin-walled components based on the internal stress field evolution. The International Journal of Advanced Manufacturing Technology. 103:3597–3612. https://doi.org/10.1007/s00170-019-03736-9

[8] Maria, A., Iñigo, L., Oier, Z., Luis, N. (2021) Improving accuracy of bulk residual stress characterization in ribbed geometries through equivalent bending stiffness. 18th CIRP Conference on Modeling of Machining Operations. 102:325-330. https://doi.org/10.1016/j.procir.2021.09.056

[9] Huang, X., Sun, J., Jianfeng, L. (2015) Finite element simulation and experimental investigation on the residual stress-related monolithic component deformation. Int J Adv Manuf Technol. 77(5-8):1035-1041. https://doi.org/10.1007/s00170-014-6533-9

[10] Zhang, Z., Li, L., Yang, Y., He, N., Zhao, W. (2014) Machining distortion minimization for the manufacturing of aeronautical structure. Int J Adv Manu Technol. 73:1765-1773. https://doi.org/10.1007/s00170-014-5994-1

[11] Su, J.C., Young, K.A., Ma, K., Srivatsa, S., Morehouse, J.B., Liang, S.Y. (2013) Modeling of residual stresses in milling. Int J Adv Manuf Technol. 65:717–733. https://doi.org/10.1007/s00170-012-4211-3

[12] Chighizola, C.R., D'Elia, C.R., Jonsson, J.E., Weber, D., Kirsch, B., Aurich, J.C., Linke, B.S., Hill, M.R. (2021) On the Effect of Bulk Residual Stress on Milling-Induced

Residual Stress and Distortion. Prepped for submission for a special edition of Experimental Mechanics.

[13] Denkena, B., Boehnke, D., de Leo´n, L. (2008) Machining induced residual stress in structural aluminum parts. Institute of Production Engineering and Machine Tools. 2:247–253. https://doi.org/10.1007/s11740-008-0097-1

[14] Weber, D., Kirsch, B., Chighizola, C.R., Jonsson, J.E., D'Elia, C.R., Linke, B.S., Hill, M.R., Aurch, J.C. (2021) Investigation on the scale effects of initial bulk and machining induced residual stresses of thin walled milled monolithic aluminum workpieces on part distortions: experiments and finite element prediction model. 18th CIRP Conference on Modeling of Machining Operations. 102:337-342. https://doi.org/10.1016/j.procir.2021.09.058

[15] Chighizola, C.R., D'Elia, C.R., Weber, D., Kirsch, B., Linke, B., Hill, M.R. (2020) Intermethod comparison and evaluation of near surface residual stress in aluminum parts subject to various milling parameters. Experimental Mechanics. 6:67-74. https://doi.org/ 0.1007/978-3-030-30098-2_10

[16] Weber, D., Kirsch, B., Chighizola, C.R., D'Elia, C.R., Linke, B.S., Hill, M.R., and Aurich, J.C. (2020) Analysis of machining induced residual stresses of milled aluminum workpieces, their repeatability and their resulting distortion. Internation Journal of Advanced Manuafacturing Technology. 115:1089-1110. https://doi.org/10.1007/s00170-021-07171-7

[17] ASTM International. (2013) E837-13a Standard Test Method for Determining Residual Stresses by the Hole-Drilling Strain-Gage Method. West Conshohocken, PA: ASTM International. https://doi.org/10.1520/E0837-13A

[18] Grant, P., Lord, J., Whitehead, P., Fry, A.T. (2006) The Application of Fine Increment Hole Drilling for Measuring Machining-Induced Residual Stresses. Applied Mechanics and Materials. 3-4:105-110. https://doi.org/10.4028/www.scientific.net/AMM.3-4.105

[19] Garcia, D.R., Hill M.R., Aurich, J.C., Linke, B.S. (2017). Characterization of Machining Distortion due to Residual Stresses in Quenched Aluminum. Manufacturing Science and Engineering Conference. V001T02A031. https://doi.org/10.1115/MSEC2017-2878

[20] Li, R., Wang, G., Zhao, X., Dai, F., Huang, C., Zhang, M., Chen, X., Song, H., Zhang, H. (2021). Effect of path strategy on residual stress and distortion in laser and cold metal transfer hybrid additive manufacturing. Additive Manufacturing. 46:2214-8604. https://doi.org/10.1016/j.addma.2021.102203

[21] Tang Z.T., Liu Z.Q., Wan Y., Ai X. (2008) Study on Residual Stresses in Milling Aluminium Alloy 7050-T7451. In: Yan XT., Jiang C., Eynard B. (eds) Advanced Design and Manufacture to Gain a Competitive Edge. Springer, London. https://doi.org/10.1007/978-1-84800-241-8_18

[22] Bilkhu, R., Ayvar-Soberanis, S. (2020). Simulation of the coupling effect of bulk and induced residual stresses on machining distortion. Conference on High Performance Cutting. 101:5-8. https://doi.org/10.1016/j.procir.2021.05.150.

[23] ASM Handbook. (1991) Heat Treating of Aluminum Alloys. ASM Handbook. 4:841-879. https://doi.org/10.1361/asmhba0001205

[24] Chighizola, C.R., Hill, M.R. (2021) Two-dimensional Mapping of Bulk Residual Stress Using Cut Mouth Opening Displacement. Experimental Mechanics. https://doi.org/10.1007/s11340-021-00745-2